

See discussions, stats, and author profiles for this publication at: <https://www.researchgate.net/publication/27411762>

A 2D variable reluctance planar motor

Article

Source: OAI

CITATIONS

4

READS

1,256

1 author:



J.F. Pan

Shenzhen University

140 PUBLICATIONS 1,780 CITATIONS

[SEE PROFILE](#)



THE HONG KONG
POLYTECHNIC UNIVERSITY

香港理工大學

Pao Yue-kong Library
包玉剛圖書館

Copyright Undertaking

This thesis is protected by copyright, with all rights reserved.

By reading and using the thesis, the reader understands and agrees to the following terms:

1. The reader will abide by the rules and legal ordinances governing copyright regarding the use of the thesis.
2. The reader will use the thesis for the purpose of research or private study only and not for distribution or further reproduction or any other purpose.
3. The reader agrees to indemnify and hold the University harmless from and against any loss, damage, cost, liability or expenses arising from copyright infringement or unauthorized usage.

If you have reasons to believe that any materials in this thesis are deemed not suitable to be distributed in this form, or a copyright owner having difficulty with the material being included in our database, please contact lbsys@polyu.edu.hk providing details. The Library will look into your claim and consider taking remedial action upon receipt of the written requests.

**The Hong Kong Polytechnic University
Department of Electrical Engineering**

A 2D Variable Reluctance Planar Motor

Pan Jianfei

**A thesis submitted
in partial fulfillment of the requirements
for the Degree of Doctor of Philosophy**

August, 2006

CERTIFICATION OF ORIGINALITY

I hereby declare that this thesis is my own work and that, to the best of my knowledge and belief, it reproduces no material previously published or written, nor material that has been accepted for the award of any other degree or diploma except where due acknowledgment has been made in the next.

(Signed)

Pan Jianfei _____ (Name of student)

Abstract

High-precision, two dimensional planar motion is often required in the manufacturing industry. An ideal planar motor should have a simple and low-cost structure with fast response. Various types of planar motors have been designed, but none of them can fulfill the requirements such as low cost, stiff structure and working under a variety of environments. Switched Reluctance (SR) motor has a simple and robust structure, therefore it has been widely applied in many industrial applications. However, due to its highly nonlinear characteristics, it has not been used in direct-drive, planar motion applications.

The aim of this project is to investigate the feasibility of employing SR technology in two dimensional, high-precision, position control applications. Under this goal, a prototype of SR planar motor has been built. Although some motor parameters are still required to be optimized, the initial machine is capable of achieving high-precision position and trajectory control under selected control algorithms.

For the initial research stage, a thorough performance prediction and analysis have been made with finite element analysis. Simulation results show that the motor has good magnetic characteristics and there is zero mutual coupling between any of the adjacent phase windings, therefore each winding can be controlled independently.

In order to fully understand the behavior of the planar motor prototype, detailed

characterization experiments have been carried out. Flux-linkage measurement based on the Step Voltage method and the Alternate Current (AC) excitation method are both performed and their results are compared. Force profiles are measured by direct measurement with a load cell and its result is compared with the results from finite element method. Other magnetic characteristics including hysteresis, leakage flux-linkage and mutual coupling are also measured and verified.

After reviewing various modeling techniques commonly used for SR motors, the nonlinear characteristics of the planar motor, flux-linkage vs. different current levels and positions are modeled with an exponential description function. The modeling precision is verified with its absolute error profile.

Two different control algorithms have been applied to tackle the nonlinearity of the SR planar motor. The first position control algorithm is composed of a reduced size nonlinear force-current-position look-up table compensator with PID control strategy. The main benefit of this method is simple and straightforward implementation, and it is more suitable for industrial applications. The second control scheme is aimed at velocity regulation based on Auto-Disturbance Rejection Control (ADRC). Experiment results show that the proposed position controller is capable of achieving good precision, and the velocity controller is highly robust, and it offers better performance than a traditional PID speed regulator.

Acknowledgments

First of all, I would like to express my sincere gratitude and appreciation to my project advisor, Dr. Norbert Cheung for his support, guidance and patience. His kindhearted assistance and encouragement have been the prime power in the completion of this research project.

Secondly, I would like to thank Associate Professor Yang Jinming, a visiting scholar from South China University of Technology, Guangzhou, PRC. He has kindly helped me with the nonlinear control of this motion system and taught me some fundamental control theories.

I would also like to give my special thanks to the University Grants Council for support of this project under the CERG Project Account Code: B-Q473.

Lastly, I would like to thank all my friends and colleagues who have offered help in time of need. I would like to give my special thanks to my parents and my girlfriend, Shumin, for their constant encouragement and support throughout my Ph.D study.

Table of Contents

1.	Introduction	1
1.1	Background	1
1.2	Motivation of the research project	3
1.3	Organization of the thesis	4
1.4	Summary of contributions	5
1.5	Publications from the research project	6
2.	Review of planar motors	8
2.1	Sawyer motor	8
2.2	Planar induction motor	11
2.3	Permanent magnet planar motor.	12
2.4	Summary	17
3.	The planar switched reluctance motor (PSRM)—design and construction. .	18
3.1	Brief review of switched reluctance motors	18
3.1.1	A rotary switched reluctance motor (RSRM)	18
3.1.2	Derivation of linear switched reluctance motor (LSRM).	19
3.2	Principles of operation	20
3.3	Design of the planar switched reluctance motor	22
3.4	Construction of the planar switched reluctance motor.	25
3.4.1.	The stator	27
3.4.2	Stator building element and matrix	28

3.4.3 The linear guides	29
3.4.4 The mover and the moving platform	30
3.4.5 Construction of the planar motor.	32
3.5 Summary of motor characteristics	33
4. Performance analysis of the planar switched reluctance motor.	35
4.1 Review of analytical methods.	35
4.1.1 Energy conversion analysis	35
4.1.2 Equivalent magnetic circuit approach	37
4.1.3 The finite element method.	40
4.2 Meshing of the planar switched reluctance motor	41
4.3 Test of zero mutual inductance.	45
4.3.1 The equivalent magnetic circuit (EQMC) approach.	45
4.3.2 The finite element method..	47
4.3.3 Experiment verification.	50
4.4 Force disparities along Z-axis	50
4.4.1 The finite element method	52
4.4.2 Experiment verification	53
4.5 Calculation of normal forces (Y-force)	54
4.5.1 Determination of air gap lengths.	55
4.5.2 Finite element analysis of normal forces	55
4.6 Analysis and measurement of propulsion force (X-force)	56
4.6.1 Calculation from FEM.	57

4.6.2 Measurement from experiment.	58
4.7 Summary	61
5. Characterization and modeling of the planar switched reluctance motor	62
5.1 Motor Characterization	62
5.2 Review of obtaining magnetic characteristics for switched reluctance motors.	63
5.2.1 Mathematical model of the planar switched reluctance motor.	64
5.2.2 Step Voltage measurement.	65
5.2.3 The AC excitation method	66
5.2.4 Comparisons of DC and AC methods of flux-linkage measurement	68
5.3 Experiment results	68
5.3.1 The Step Voltage method	69
5.3.2 The AC excitation method	71
5.4 Leakage flux-linkage.	75
5.5 Modeling of the planar switched reluctance motor.	76
5.6 Review of flux-linkage modeling methods.	77
5.6.1 The look-up table method.	78
5.6.2. Piecewise linear approximation.	78
5.6.3 Parabolic approximation.	78
5.6.4 Arc-tangent representation	80
5.6.5 Cubic-spline.	81
5.6.6 Exponential description.	82

5.7 Modeling of the planar switched reluctance motor	83
5.8 Dynamic model of the planar switched reluctance motor	84
5.9 Summary	85
6. Trajectory control of the planar switched reluctance motor.	86
6.1 The current controller.	86
6.1.1 Introduction	86
6.1.2 Current controller for the planar switched reluctance motor.	88
6.1.3 Test verification.	91
6.2 Phase excitation schemes.	93
6.2.1 Single phase excitation.	93
6.2.2 Multi-phase excitation	96
6.2.3 The excitation scheme for the planar switched reluctance motor.	97
6.3 Linearization of the planar switched reluctance motor.	99
6.3.1 Introduction.	99
6.3.2 Linearization scheme for the planar switched reluctance motor	100
6.3.3 Experiment verification	103
6.4 The position controller.	105
6.4.1 The Proportional Derivative (PD) controller	105
6.4.2 Experiment results	107
6.5 The dual-loop position controller.	112
6.5.1 Introduction	112
6.5.2 Controller derivation	115

6.5.3 Experiment verifications.	116
6.6 Summary.	118
7. Speed Regulation with auto-disturbance rejection control (ADRC)	119
7.1 Introduction.	119
7.2 The auto-disturbance rejection controller (ADRC)	121
7.2.1. Whole structure..	122
7.2.2 Tracking differentiator (TD)	122
7.2.3 Nonlinear state error feedback (NLSEF)	123
7.2.4 Extended state observer (ESO)	125
7.3 Construction of the velocity controller..	128
7.4 Simulation results	132
7.5 Experiment results	134
7.6 The three-loop controller.	142
7.7 Summary	144
8. Conclusions and future work	145
8.1 Conclusions on the planar motor.	145
8.2 Conclusions on the characterization and modeling of the PSRM.	146
8.3 Conclusions on the control of the PSRM.	147
8.3.1 Nonlinear compensation.	147
8.3.2 Position control.	147
8.3.3 Speed regulation.	148
8.4 Achievements of this research work.	148

8.4.1 Motor design and construction.	149
8.4.2 Performance analysis of the PSRM.	149
8.4.3 Characterization and modeling of the PSRM.	150
8.4.4 Control strategies.	150
8.5 Suggestions for further research.	151
Appendix A.	153
Appendix B.	157
References.	159

List of Figures

Fig.2.1 Overall structure of a Sawyer motor

Fig.2.2 The perspective view and side view of a planar induction motor

Fig. 2.3 Energize for rotary motion and linear motion in a planar induction motor

Fig.2.4 Structure of the PM planar motor

Fig.2.5 Four arrangements of stator for PM planar motors

Fig.2.6 Structure of the planar motor

Fig.3.1 A series-wound 6/4 rotary SR motor with its topology and typical flux path

Fig.3.2 Formation of a LSRM from a RSRM

Fig.3.3 The LSRM

Fig.3.4 Basic structure of one axis for the LSRM at Aligned and un-aligned position

Fig.3.5 Photo of the PSRM

Fig.3.6 Motor construction

Fig.3.7 The stator base (part view)

Fig.3.8 Stator lamination, one block, block formation and block combination (bricks) with
flux path

Fig.3.9 Top view of the PSRM

Fig.3.10 Equivalent overlapping air gap area

Fig.4.1 Magnetization curve for aligned and un-aligned positions

Fig.4.2 Reluctance definition and equivalent magnetic circuit

Fig.4.3 3D finite element models of one mover and stator

Fig.4.4 2D meshes of the mover, the stator and the air gap

Fig.4.5 The race track

Fig.4.6 The complete 3D finite element model

Fig.4.7 Equivalent magnetic circuit of the movers and reluctance of the mover

Fig.4.8 3D FEM model for mutual inductance test

Fig.4.9 2D flux distribution from one activated mover at 8A

Fig.4.10 Flux distribution when one mover is activated at 8A for one mover and its adjacent neighbor

Fig.4.11 Coupling effect between the closest windings

Fig.4.12 Longitudinal end effects and transverse edge effects

Fig.4.13 Side view of the PSRM with a six-step sequence

Fig.4.14 Force disparities along Z-axis at fixed X position (X=3mm)

Fig.4.15 Force variations of Z-axis

Fig.4.16 Normal force at different air gap lengths

Fig.4.17 Propulsion force at different positions with respect to current

Fig.4.18 Saturation effect with higher current excitation

Fig.4.19 Load cell and the test-rig

Fig.4.20 Experiment setup of force measurement

Fig.4.21 Force output from experiment measurement of Y-axis

Fig.4.22 Force comparisons at 5A and 8A from FEM and experiment

Fig.5.1 Equivalent electrical circuit

Fig.5.2 Experiment setup for Step Voltage measurement

Fig.5.3 Current and voltage waveform from the Step Voltage method

Fig.5.4 Flux-linkage waveform

Fig.5.5 Search coil locations

Fig.5.6 Experiment setup for AC excitation flux-linkage method

Fig.5.7 Hysteresis loops of the PSRM for one phase

Fig.5.8 Flux-linkage at different current levels

Fig.5.9 Possible flux paths

Fig.5.10 Leakage flux-linkage for the un-aligned position

Fig.5.11 Approximation of flux-linkage vs. current curves

Fig.5.12 Flux-linkage modeling

Fig.5.13 Error from exponential curve-fitting

Fig.6.1 A typical hysteresis current regulator and a PWM current regulator

Fig.6.2 Current waveform in a typical hysteresis controller

Fig.6.3 An asymmetric bridge PWM inverter

Fig.6.4 Block diagram for current control loop

Fig.6.5 Current response of the motor's coil at fully aligned position and fully un-aligned position

Fig.6.6 Ideal inductance profile

Fig.6.7 Waveform of three phases and total force output at a certain speed from single phase excitation

Fig.6.8 Reference position

Fig.6.9 Position control block with multi-phase excitation for one axis

Fig.6.10 Flow chart for obtaining i^*

Fig.6.11 Bi-linear interpolation from the look-up table

Fig.6.12 3D relationship between force output with respect to position and force command

and 2D relationship between force output and force command at certain positions

Fig.6.13 Simplified position control block

Fig.6.14 Control block of the PSRM and experiment setup

Fig.6.15 Trajectory response of the PSRM for circular motion

Fig.6.16 Overall performance

Fig.6.17 Error response from simulation

Fig.6.18 Error response from experiment for X-axis at 0.5 Hz and 1 Hz

Fig.6.19 The construction of the inner controller

Fig.6.20 Error response under dual-loop position controller for X-axis at 0.5 Hz and 1 Hz

Fig.7.1 The ADRC control block

Fig.7.2 Comparison of linear and nonlinear gains

Fig.7.3 ADRC scheme for velocity control

Fig.7.4 The whole control diagram of the controller

Fig.7.5 Response of mass change from PID and ADRC

Fig.7.6 Response of PID and ADRC for load change at 0.2 s

Fig.7.7 Response of PID and ADRC controller at friction variation at 0.2 s

Fig.7.8 Block diagram of the whole control scheme

Fig.7.9 Overall experiment setup

Fig.7.10 Response of PID controller under 0.5 Hz, 20 mm

Fig.7.11 Response of ADRC controller under 0.5 Hz, 20 mm

Fig.7.12 Response of PID controller under 1 Hz, 20 mm

Fig.7.13 Response of ADRC controller under 1 Hz, 20 mm

Fig.7.14 Response of PID and ADRC controller under mass change at 0.5Hz, 20 mm

Fig.7.15 Response of PID and ADRC controller under force variation at time=1.8 s at
0.5Hz, 20 mm

Fig.7.16 Response of PID and ADRC controller under force variation at time=1.8 s at
0.5Hz, 20 mm

Fig.7.17 The three-loop control scheme

Fig.7.18 Simulation result under two-loop control

Fig.7.19 Simulation result under three-loop control

List of Tables

Table 3.1 Design specifications of the PSRM

Table 5.1 Modeling parameters of the PSRM

Table 6.1 The multi-phase excitation scheme

Table 7.1 Parameter regulation

List of Acronyms

AC	Alternate Current
ADC	Analog-to-Digital Converter
ADRC	Auto-Disturbance Rejection Control
DAC	Digital-to-Analog Converter
DC	Direct Current
DSP	Digital Signal Processor
EMF	Electromagnetic Force
EMI	Electromagnetic Interference
EQMC	Equivalent Magnetic Circuit
ESO	Extended State Observer
FEM	Finite Element Method
LSRM	Linear Switched Reluctance Motor
MMF	Magnetomotive Force
NLSEF	Nonlinear State Error Feedback
PC	Personal Computer
PCI	Peripheral Component Interconnect
PD	Proportional and Differential
PI	Proportional and Integral
PID	Proportional, Integral and Differential
PM	Permanent Magnet
PSRM	Planar Switched Reluctance Motor
PWM	Pulse Width Modulation
RSRM	Rotary Switched Reluctance Motor
RTI	Real-Time Interface
SR	Switched Reluctance
TD	Tracking Differentiator

List of Symbols

B	flux density, T
B_v	friction coefficient, N/m
d	pole width, mm
e_{bemf}	back EMF, V
f	force component for X, Y or Z direction, N
f_l	load force, N
$f_{x(y)}$	propulsion force of X- or Y-axis, N
g_{kj}	coefficient matrix
H	magnetic field intensity, A/m
i	current, A
J_s	source current density, A/S^2
K_c	converter gain
K_p	proportional gain
K_i	integral gain
K_d	derivative gain
l	stack length, mm
L	winding inductance, H
L_Δ	change of inductance, H
M	mass, Kg
N	number of turns

p	pole-pitch, mm
q	slot width, mm
$R_{x(y)}$	winding resistance, Ω
R	reluctance, AWb^{-1}
s	displacement, m
v	volume, mm^3
V	winding voltage, V
W_c	co-energy, J
W_e	total electrical energy, J
W_f	stored energy, J
W_m	mechanical energy, J
x	position of X mover, m
z	air gap length, mm
λ	flux-linkage, Vs
φ	flux density, Wb
Γ	magnetomotive force, A
ς	damping factor
ω_n	natural frequency, $rads^{-1}$
θ	angle, rad
μ_0	vacuum permeability, H/m
μ_r	relative permeability

Chapter 1

Introduction

1.1 Background

Precise two dimensional, high-precision motion control system is in high demand in industry. For many applications, such as electronic component insertion, integrated circuit packaging, and precision watch assembly, all require high-precision planar motion. At present, the X-Y table still plays a key role in these applications. The X-Y table achieves planar motion by stacking two linear slides with rotary motors on top of each other. Linear motion is achieved by the coupling of a rotary motor to a rotary to linear mechanical translator such as gears or shafts. Though this is the commonly used method, it has the following disadvantages of i) reduced accuracy, ii) complex mechanical structure, iii) high production cost and iv) frequent adjustments and alignments.

Since the X-Y table has the above problems, direct-drive motion system is a better option to achieve linear and planar movements. In a direct-drive system, the mechanical output of the machine is directly coupled to the machine load, thus eliminating any mechanical translator, such as pulley, belt or gear. With the direct coupling method, the mechanical structure is greatly simplified and the whole system is easier to assemble, reduced in cost, and increased in performance. The linear motor is one example of this type of machine. Linear motion is generated directly by the moving platform without the help of any mechanical translators.

Instead of the combination of two or more actuators stacked on top of each other, a direct-drive planar motor is a machine which contains a moving platform that can directly provide two dimensional movements. Presently, the following types of planar motors have been reported,

- i) The Sawyer motor
- ii) The planar induction motor
- iii) The permanent magnetic (PM) planar motor

The Sawyer motor [1, 2] is the first type of machine providing two-axis of movement and it is the only type of planar motor readily available to industry. Though it can provide uniform performance over the entire workspace and offer high speeds, its open-loop control structure often leads to the loss of steps and deterioration in performance when subjected to external disturbances. The other two types of planar motors operating under closed loop mode are the planar induction motor and permanent magnet planar motor [3-5]. Like rotary induction motors, the planar induction motor has a simple and robust structure with low production cost, but two dimensional motion is difficult to achieve due to the motor's complicated core structure configuration [3]. The permanent magnetic planar motor is configured to different structures according to the location of permanent magnets. However, no matter where the permanent magnets are located, the designers will always encounter the problems of either complex stator coil structure [4] or massive expenses spent on large number of N- and S-pole permanent magnetic blocks [5].

1.2 Motivation of the research project

With the exception of the Sawyer motor, planar motor structure either involves complicated coil windings or expensive magnetic materials to realize two-axis of movement. Therefore these prototypes only remain in the research stage and the disadvantages hinder them from practical industrial use.

After surveying the typical applications of actuators for two dimensional movements [6, 7], the essential requirements for a good planar motor should be i) low cost, ii) fast response, iii) able to operate in wide temperature range, iv) high efficient, v) robust, vi) accurate, and vii) maintenance free.

Based on all these requirements, the investigation of a planar motion system based on variable reluctance, also termed as switched reluctance (SR) principle has been explored. Motivated by the attractive features and recent advancement of SR machines, this project mainly focuses on the creation and development of a low-cost, novel planar motor with a simple structure as an ultimate solution to 2D direct-drive motion systems. Coinciding with the requirements for a good planar motor, the SR machine has many outstanding features, such as simple structure, high robustness, low cost and capability of operation in extreme temperatures. However, due to the highly nonlinear characteristics inherent in the magnetic path, its control is complex and the output has large torque or force ripples. Therefore it has never been a popular choice for high-precision and high-speed motion applications until the recent resurge of interest in SR motors [8-10]. This resurge of interest mainly owes to the advancement of power electronics and digital signal processing, and the continuous trend of “simplifying the mechanics through improved control strategy”. However, most of these

developments are directed towards general speed/torque operation and the linear motor applications remain in transportation. This project is the first attempt to develop a SR motor for two dimensional direct-drive motion systems for high-precision applications.

1.3 Organization of the thesis

The initial stage of the research (Chapter 1) surveys on the current direct-drive 2D motion systems and compares different types of planar motors available today. Detailed characteristic analysis on the advantages and disadvantages of each motion system is thoroughly examined in Chapter 2. Then a motion system based on SR principle is proposed in Chapter 3. This chapter introduces the design and construction of the entire motion system with SR principle.

Chapter 4 focuses on the performance analysis of the motor magnetic parameters. The finite element analysis and the experiment results of the SR motor are obtained.

Chapter 5 discusses the characterization of the planar motor. Experiment for flux-linkage measurement is conducted to explore the motor's characteristics. Magnetic parameters such as hysteresis and leakage flux-linkage are also obtained. Then, different modeling techniques for the motor measurement are compared and a simple yet precise modeling method is proposed. Compared with the experiment results, the model is confirmed to be accurate.

Chapter 6 proposes a simple and effective position controller for the planar motor which is expected for future practical implementation in industry. An improved dual-loop PID controller is proposed. This controller aims at dynamic error reduction as the frequency

increases. Detailed experiment results are recorded and investigated.

Chapter 7 focuses on investigation of a robust velocity controller based on the auto-disturbance rejection control (ADRC) concept. Both simulation and experiment results show that the controller is effective and robust to disturbances.

1.4 Summary of contributions

After the analysis and comparison of different forms of existing two dimensional motion systems, a unique prototype of planar motor based on SR principle is constructed.

Design details are provided in this thesis. The finite element method (FEM) is introduced for performance prediction and analysis investigation of the PSRM. Many magnetic parameters are anticipated or calculated.

Various flux-linkage measurement techniques for the PSRM are investigated and advantages and disadvantages are compared. Flux-linkage of the PSRM is measured with the Step Voltage method and AC excitation method respectively. Other magnetic properties such as leakage flux-linkage are also explored.

Investigation of various kinds of flux-linkage modeling methods for the planar switched reluctance motor (PSRM) has been carried out, and the effective exponential modeling method is selected. Thereafter, the construction of a concise dynamic model of the PSRM is obtained.

At the first stage of controller design, a simple PD controller suitable for industrial applications is tried out. Then an improved dual-loop PID controller, especially for error reduction with increased operating frequency is proposed and implemented.

Nonlinear robust velocity controller design for the PSRM is investigated with the implementation of the ADRC concept. Both the simulation and experiment results show that the PSRM is resistant to disturbances under ADRC control.

1.5 Publications from the research project

1.5.1 Patent

N. C. Cheung, J. F. Pan, and J. M. Yang; “Two Dimensional Variable Reluctance Planar Motor,” Ref: IP-135A, file no: I040420E, filed date: July 2004

1.5.2 Conference paper

- 1) Norbert C. Cheung, Jianfei Pan and Jinming Yang, “A Novel 2D Variable Reluctance Planar Actuator for Industrial Automation”, *European Power Electronics and Drives Association*, 2003
- 2) Jianfei Pan, Norbert C. Cheung and Jinming Yang, “Structure and Characteristics of Closed-loop Two-dimensional Surface Motors”, *Fifth International Conference on Power Electronics and Drive Systems*, 2003, pt. 1, p 236-41 Vol.1
- 3) J.F. Pan, Norbert C. Cheung and Jinming Yang, “Position Control of a Novel Planar Switched Reluctance Motor”, *Thirtieth Annual Conference of IEEE Industrial Electronics Society*, 2004 , Volume 3, 2-6 Nov. 2004 Page(s):2400 - 2405 Vol. 3
- 4) J.F. Pan, San Chin Kwok, Norbert C. Cheung and J.M. Yang, “Auto-Disturbance Rejection Speed Control of a Linear Switched Reluctance Motor”, *Fortieth International IAS Annual Meeting, Industry Applications Conference*, 2005, Volume 4, 2-6 Oct. 2005, Page(s):2491 - 2497
- 5) J.F. Pan, N. C. Cheung, and Gan Wai-Chuen, “A Novel Switched Reluctance Motor for Industrial Applications”, *IEEE International Magnetics Conference*, 2006

1.5.3 Journal paper

- 1) N.C. Cheung and Jianfei Pan, “Using VR Actuators in Automated Manufacturing Machines”, *Industrial Robot*, Vol. 30, Nov 4, 2003, Page(s):355-362
- 2) J.F. Pan, N.C. Cheung, and J.M. Yang, “High-precision Position Control of a Novel Planar Switched Reluctance Motor”, *IEEE Transactions on Industrial*

Electronics, Volume 52, Issue 6, Dec. 2005 Page(s):1644 - 1652

- 3) J.F. Pan, N.C. Cheung and J.M. Yang, "An Auto-Disturbance Rejection Controller for the Novel Planar Switched Reluctance Motor", *IEE Proceedings on Electric Power Applications*, March 2006, Page(s):307- 316
- 4) J.F. Pan, N.C. Cheung, Gan Wai-Chuen and Shiwei Zhao, "A Novel Switched Reluctance Motor for Industrial Applications", *IEEE Transactions on Magnetics*, Vol. 42, No. 10, Oct, 2006

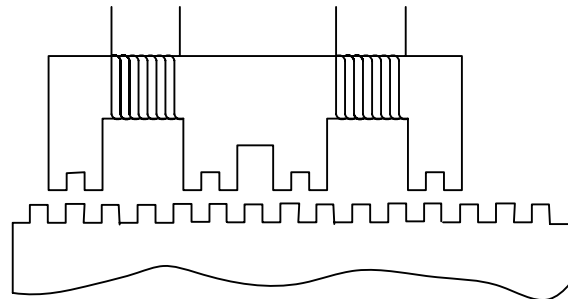
Chapter 2

Review of planar motors

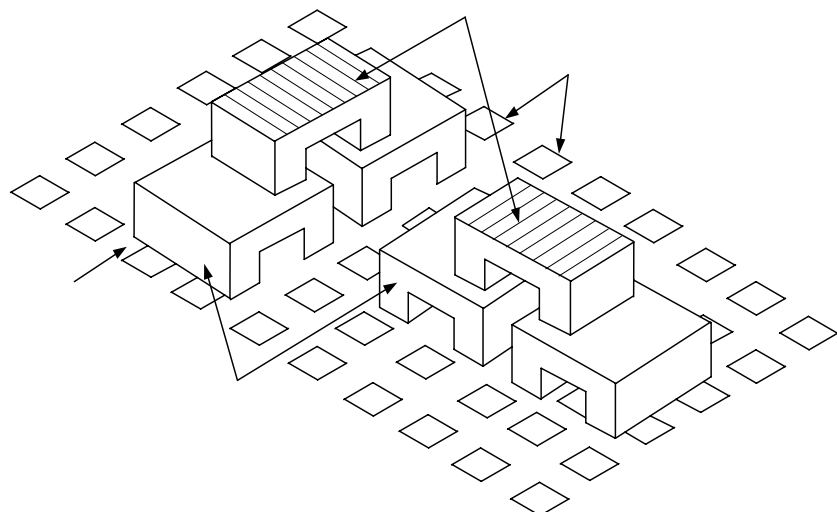
Planar motors, also named as surface or X-Y motors, are essentially different from traditional X-Y tables. Instead of stacking two linear slides on top of each other, the planar motor has a moving platform which can be directly driven and controlled in both X and Y directions. This chapter reviews several types of planar motors with different propulsion mechanism and their motor characteristics are also investigated.

2.1 Sawyer motor

Presently, the Sawyer motor is the only type of planar motor that is readily available to industry. To achieve two dimensional motion, the motor consists of two sets of single axis driving coils, arranged perpendicular with each other. The motor often operates in an open-loop stepping manner; it has the characteristics of providing uniform performance over the entire workspace. The moving platform can operate at fairly high speed, acceleration and precision [1, 2, 11]. Sawyer motors have been successfully employed in two dimensional flatbed plotters and wafer probers. However the motor has the drawbacks of i) susceptible to loss of steps, ii) unable to accomodate external disturbances, iii) unable to provide high stiffness.



(a)



(b)

Fig.2.1 Overall structure of a Sawyer motor in (a) two dimensional view (b) three dimensional view

Fig.2.1 (a) shows the simplified structure for a single axis of the Sawyer motor. The mover contains two sets of driving coils, arranged in a perpendicular fashion. Each set of coil contains a permanent magnet attached to two U-shaped coils at both ends of its poles. The stator platform is made of ferromagnetic material to provide the return path for the magnetic field of the mover as shown in Fig.2.1 (b). By exciting the driving coils, flux is built up along the permanent magnet, the mover poles and stator teeth. In this way, one-axis motion can be achieved. Two-axis motion can be obtained by assembling two identical movers on a single motor frame with their axes perpendicular to each other.

The control strategy for Sawyer motors often applies a “digital open-loop control system” structure with a typical precision of 0.2 mm [12]. Operating in an open-loop manner, it is subject to loss of steps and performance deterioration at high speed.

Since there is no guiding mechanism on the moving platform, the mover is subjected to rotation under unbalanced electromagnetic forces. The rotary torque is caused by resultant force that does not pass through the center of mover mass. Two effective solutions have been proposed to avoid such negative effect—i) to arrange mover coils in a proper manner to balance rotary effect, or ii) to reduce the length ratio of slot width to the pole-pitch [13].

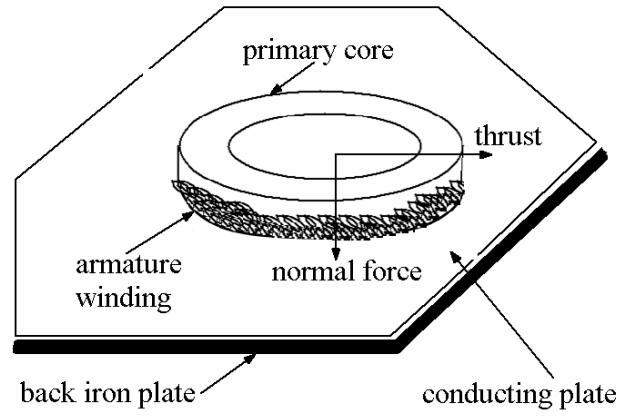
As far as the material for the magnetic flux path of Sawyer motor is concerned, a single material cannot meet the demand for both high motor speed and force output. No currently known material has both low eddy current losses and high saturation flux density property. Therefore composite magnetic structure of several different materials is often used. The motor is made up of Vanadium Permendur as stator teeth, and ferrite material as supporting substrate [12]. It has the advantages of providing higher motor force, higher speed, and low manufacturing cost.

Sawyer motors were initially designed as open-loop for stepping operations. However, in recent years, there have been many investigations which operate Sawyer motors in closed loop mode with the implementation of proper sensors. The system with accelerometer was first proposed [14] to provide velocity or tachometer feedback. Using the stator plane as a reference, several other means to sense position are also available, which are—(i) magnetic (ii) capacitive and (iii) optical [13, 15].

2.2 Planar induction motor

The first attempt toward making a planar induction machine is to use two linear induction motors arranged perpendicularly. This arrangement does not have multiple and complicated armature windings or magnetic poles compared with the structure of permanent magnet planar motors. It has the same composition as a single-sided linear induction motor. However the two windings for X and Y direction have to perpendicularly intersect to each other under magnetic interactions. Due to the complicated configuration of the core, it is difficult to form a good magnetic circuit.

An induction type of circular shaped planar motor is proposed in [16], whose moving platform has a toroidal structure as the primary core as shown in Fig.2.2. The secondary surface is composed of a flat conducting plate and a back iron plate. The mover can perform rotation in addition to linear motion on the surface and it can obtain thrust for any direction.



(a)

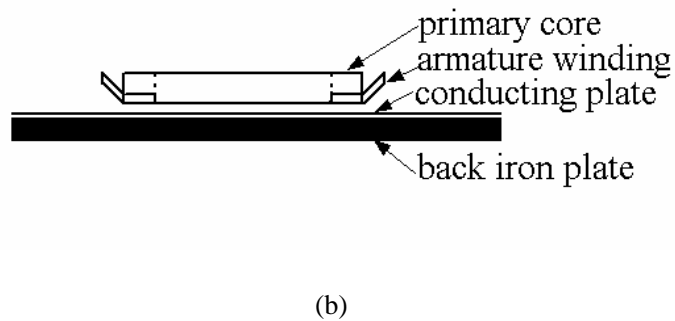


Fig.2.2 The (a) perspective view and (b) side view of a planar induction motor

For rotating motions, the two halves of the coil are energized to generate the rotating turning torque as an axial gap type of rotating motor, as shown in Fig.2.3 (a). For linear motions, the two halves of the windings are energized differently as shown in Fig.2.3 (b). The resulting force is a linear forward force accordingly [17, 18].

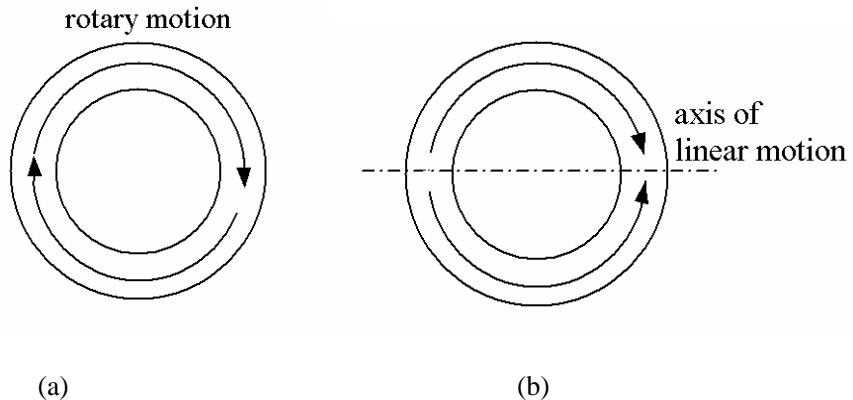


Fig. 2.3 Energize for (a) rotary motion and (b) linear motion in a planar induction motor

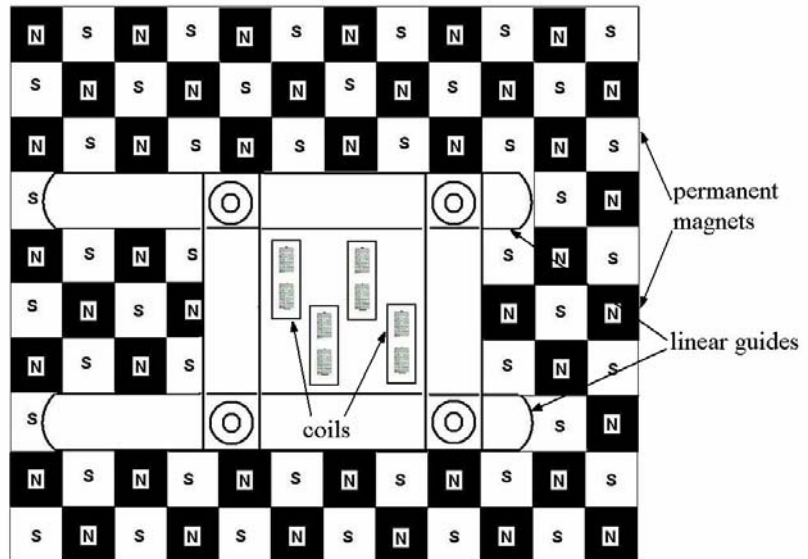
Planar induction motors have a smooth force output but they have difficulty in developing high air gap flux density. Therefore the output force is small. However the simple conducting plate ensures large traveling area.

2.3 Permanent magnet planar motor

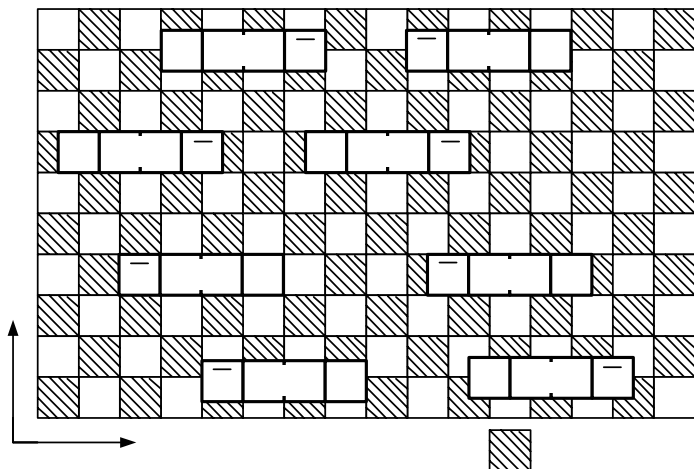
Presently, there are two types of planar motors based on permanent magnet motor

principle and they are classified according to the position of the permanent magnets. The first type applies the “magnet matrix with active coil” structure. The motor employs a number of permanent magnets to form the stator matrix. By a suitable arrangement of magnets, the stator shape and traveling length are adjustable. The second type has the “moving magnets with coil matrix” structure. The stator matrix is composed of a number of orthogonal coil windings. When the coils are excited, with the interaction with the permanent magnets from the moving platform, the motor can move in two dimensions.

The overall structure of the first type of PM planar motor [5] is shown in Fig.2.4 (a). It is composed of stator, mover, supporting mechanism and coils. The stator is a checkerboard arrangement of N- and S-pole magnets, which is laid atop a back iron plate. The mover is a bakelite truck platform and it has eight core coils, each magnetically independent. As shown in Fig.2.4 (b), these cores and coils are positioned in such a way that by selecting among different combinations of excitation phases, the mover can be moved in both X and Y directions. For example, if the phase excitation is changed from A to B, the motor generates the magnetic force so that the mover will move half of the magnetic width along the X-axis because phase B is positioned half of the magnetic width along X direction.



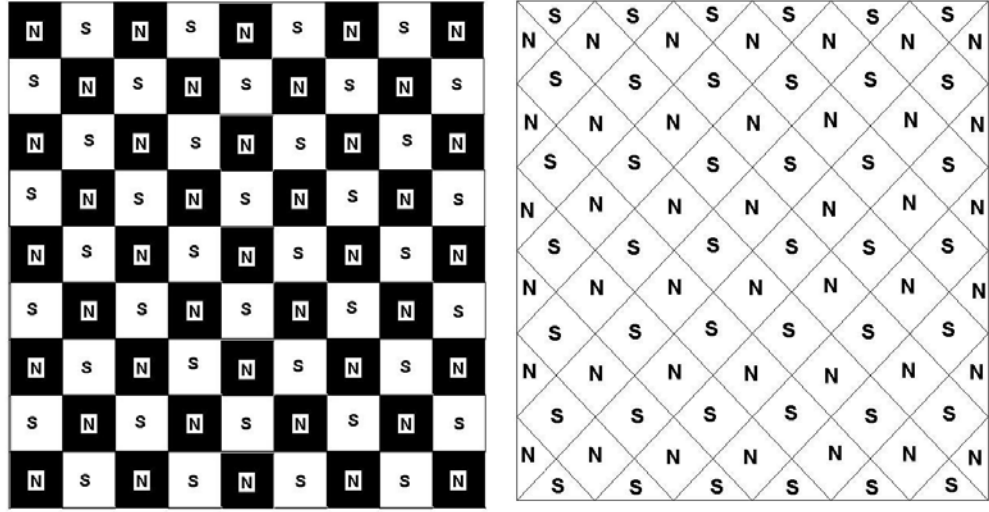
(a) Overall structure



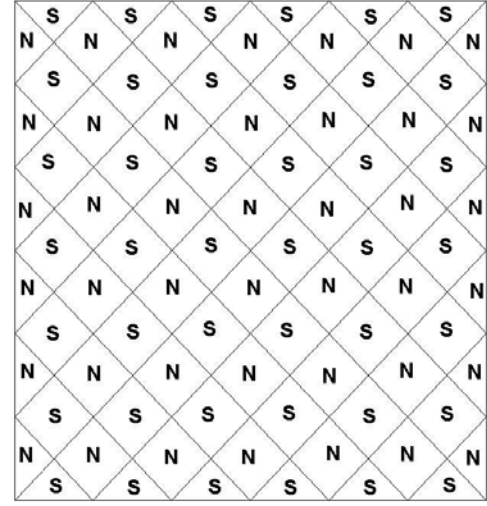
(b) Stator perspective view

Fig.2.4 Structure of the PM planar motor

At present the magnet arrangement of the stator poles consists of four major forms, as shown in Fig.2.5 (a)—(d) [19-22],



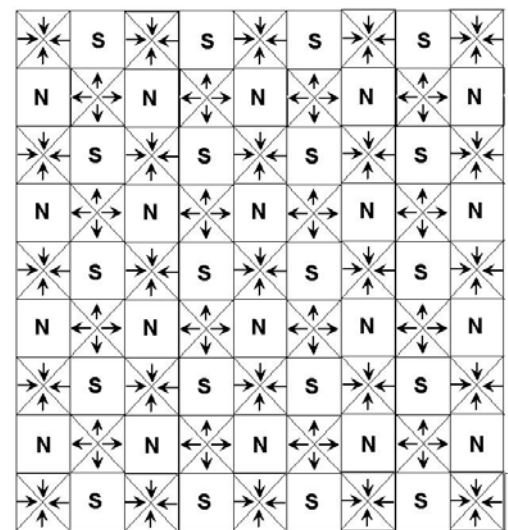
(a)



(b)



(c)



(d)

Fig.2.5 Four arrangements of stator for PM planar motors

The second type of PM planar motor has an inverse arrangement of mover and stator coils and it is proposed in [4]. The structure of the stator is a stationary slotless armature with orthogonal windings. The mover is composed of two high-efficient permanent magnets. The orthogonal windings have no electric connections and they are produced in such a way that over one layer of the X coil there will be a layer of the Y coil. Each winding is divided into twelve independent phases and the winding has the same width as the permanent magnets.

Only the necessary coil sections responsible to produce the motion force will be excited. The disadvantages of this structure are the presence of significant end effects and the normal force that reduces the actuator performance.

Another PM planar motor belonging to the second type with a different stator coil matrix [23] is shown in Fig.2.6. The mover is free from wire connections. By means of appropriate excitations of stator coils, the mover can rotate itself in addition to performing coordinate motion in two directions of the X-Y plane. The mover and the stator are completely separated and the motor is expected to be used for sealed space applications.

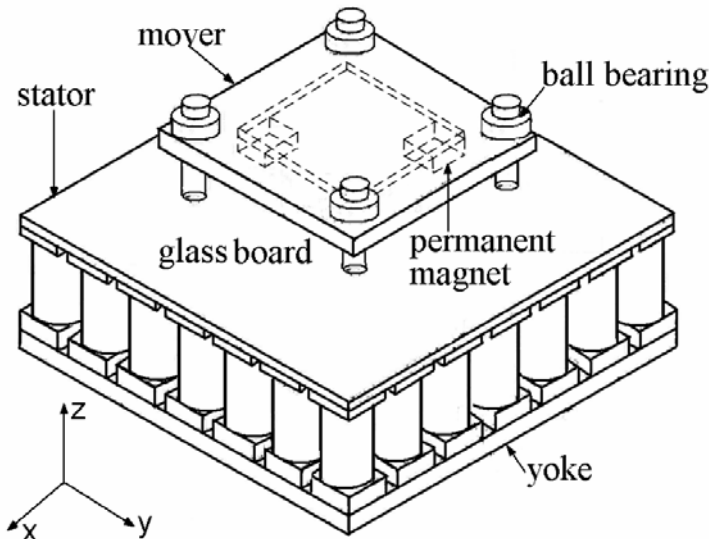


Fig.2.6 Structure of the planar motor

The PM planar motors rely on permanent magnets to produce the magnetic force, thus requiring multiple armature windings or big magnet poles to be installed. Since the working area of the secondary surface should be much larger than the primary moving one, therefore, the utilization rate of the permanent magnets is quite low. From the introduction of planar motors discussed above, the designers always encounter the problems of either complex stator coil structure or massive expenses spent on large number of N- and S-pole permanent

magnet blocks.

2.4 Summary

From the investigation of 2D direct-drive motors mentioned in this chapter, none can meet all the requirements stated before. The Sawyer motor is lack of robustness and accuracy since its open-loop control structure often leads to loss of steps and reduced precision. Although the motor can operate under closed loop, the whole motion system is complex and the implementation cost is high. The planar induction motor has the disadvantage of a complicated winding structure, therefore the motor has high increasing manufacturing cost and requires constant maintenance. Although it has a robust motor structure, the low output efficiency prevents its use for industrial applications. As for the PM planar motor, the introduction of permanent magnets will inevitably raise manufacturing cost and prevent the machines from operation in wide temperature ranges. Furthermore, the involvement of permanent magnets also limits the magnitude of input signal and complicates the control strategy. Considering the construction of the overall motor construction, the PM planar motor either involves a complex coil structure or complicated magnet arrangement.

To overcome some of the problems mentioned from the above planar motors, this project proposes a new type of planar motor based on SR principle.

Chapter 3

The planar switched reluctance motor—design and construction

3.1 Brief review of switched reluctance motors

In this chapter, first, the rotary and linear switched reluctance motors are briefly reviewed. Then design and construction of the planar switched reluctance motor (PSRM) is discussed in detail. Last the summary of motor characteristics is given at the end of this chapter.

3.1.1 A rotary switched reluctance motor (RSRM)

The concept of SR is an old idea which can trace back to the 17th century [24]. However, it was not until recently, with the fast development of modern power electronics, that have SR motors regained research and industrial interest.

The operation of SR motors is based on the “minimum reluctance” principle of a magnetic circuit. The moving parts have a tendency to minimize the reluctance of the magnetic path at the instance of current excitation. The position where the reluctance reaches minimum is referred to as the “full alignment” position and the generated torque/force at these positions is minimal. Any positions except these are referred to as “out of alignment”. As shown in the RSRM of Fig.3.1 (a), when the rotor poles are in alignment with the two stator poles AA’, another set of rotor poles is out of alignment with

respect to a different set of winding stator poles BB'. Thus this set of rotors can be brought to alignment by energizing the phase winding coil BB'. Under this circumstance, a flux path is set up through the rotor, air gap, stator and stator yoke as shown in Fig.3.1 (b). In order to reduce eddy current effect, the stator and rotor are made of laminated silicon-steel sheets. SR motors are mechanically and thermally robust, because they consist of simple stator windings and straight forward silicon-steel sheet laminations. Unlike other type of machines, they do not involve commutators, rotor windings or permanent magnets. Therefore SRMs are suitable for easy manufacture and mass production.

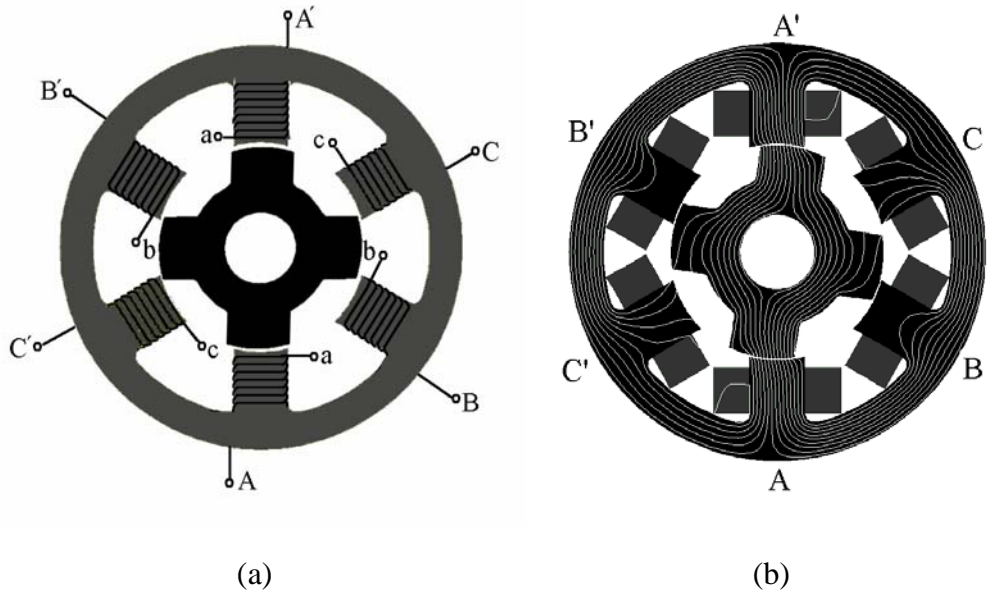


Fig.3.1 A series-wound 6/4 rotary SR motor (a) topology (b) a typical flux path

3.1.2 Derivation of a linear switched reluctance motor (LSRM)

The formation of a LSRM can be explained by the illustration of Fig.3.2. The stator of a RSRM is cut and flattened, and a LSRM is formed.

A LSRM may have windings either on the stator or on the translator. With respect to

the location of the phase windings, the LSRM can be classified as “passive-translator-active-stator” or “passive-stator-active-translator” structure. The latter type has the following advantages [25],

- i) Simple manufacture of the stator base without complicated coil arrays
- ii) Flexible traveling range and stator dimensions
- iii) Easy manufacture of mover slots with mounted coil windings

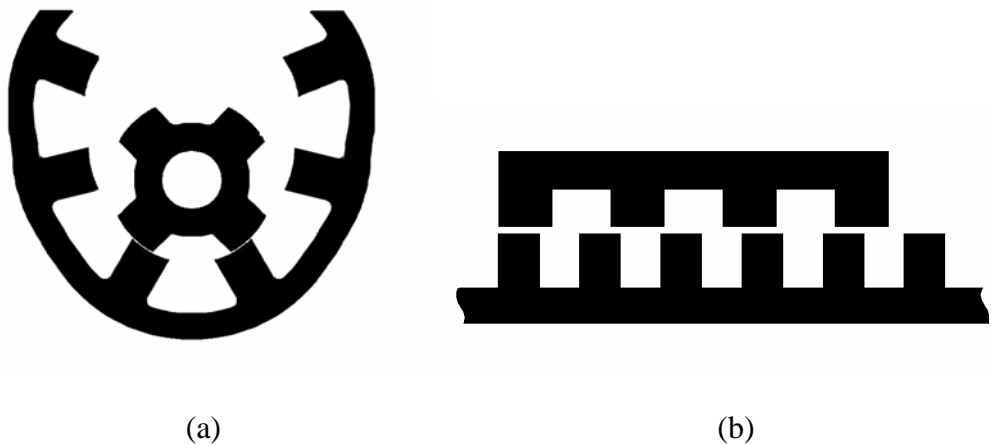


Fig.3.2 Formation of a LSRM (b) from a RSRM (a)

3.2 Principles of operation

Fig.3.3 shows a typical LSRM [27]. The stator base and the movers are manufactured with aluminum. The silicon-steel laminations are stacked between the stator and mover slots. A pair of linear motion guide ensures smooth sliding motion and supports the moving platform. A linear optical encoder is mounted on the motion actuator to observe the motion profile and provides position feedback.

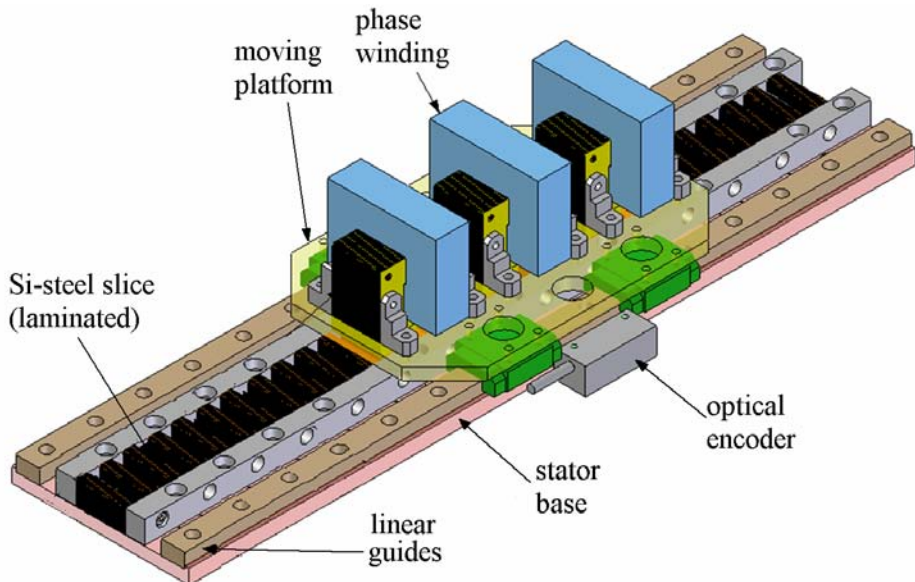


Fig.3.3 The LSRM

Fig.3.4 (a) shows the cross section of this three-phase LSRM. Any one of the three mover bodies A, B or C is termed as “aligned” whenever its teeth correspond to any set of stator teeth (Fig.3.4 (b)). In the aligned positions, the reluctance of the magnetic circuit reaches minimum with zero propulsion force. The mover body will remain at these stable points when its coil is excited. As one phase is aligned, the other two are out of alignment with respect to a different set of stator poles. When the mover body moves to the positions where it totally agrees to stator pole slots (Fig.3.4 (c)), such positions are termed as “un-aligned” with maximum reluctance of the magnetic circuit. Therefore, by switching the currents between the three phase windings in a proper manner, the mover bodies will become aligned and un-aligned sequentially, and the moving platform can move left or right.

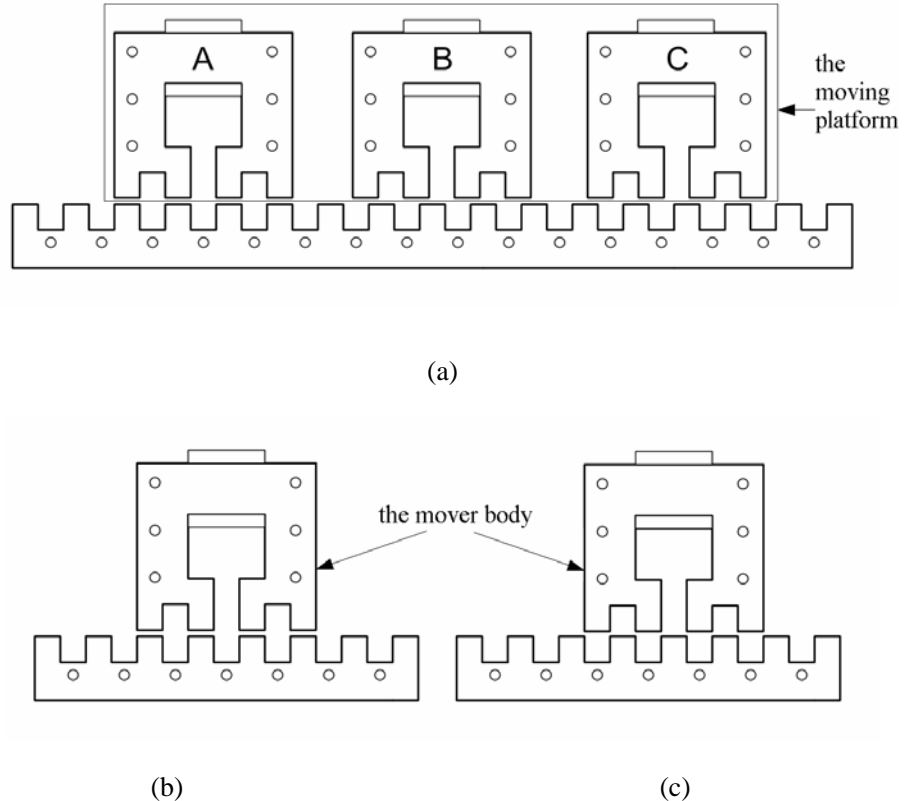


Fig.3.4 (a) Basic structure of one axis (b) Aligned and (c) un-aligned position

Compared with its rotary counterpart, this type of LSRM has the characteristics of a larger air gap. The attraction force is totally directed downwards on the moving platform for the LSRM, while in the case of RSRM, the attraction force can be balanced by the stator pole and its diametrically opposite pole when excited. Therefore a pair of rigid linear guides is one of the important factors for the design of this LSRM. This arrangement not only facilitates linear motion with low friction, but also endures all the normal pressure and tries to maintain a uniform air gap.

3. 3 Design of the planar switched reluctance motor

Up till now, there has been no article that describes a detailed design procedure of planar SR motors for position control applications; recent research topics mainly focus on

the speed regulation and applications for transportsations of linear SR motors [26]. The fabrication of the prototype PSRM for this research project is based on the knowledge of the previously built LSRM [27] with the extension of an extra perpendicular axis of motion. It is primary intended for high-precision positioning of electronic components. The pole-width and pole-pitch of the two motors are identical as 6mm and 12 mm respectively and also the PSRM can make use of the same magnetic material applied in the LSRM. The proposed specifications of the PSRM prototype are shown in Table 3.1.

Maximum loading (X)	10 Kg
Maximum loading (Y)	20 Kg
Max velocity (X & Y)	0.1 m/s
Max acceleration (X & Y)	2.5 m/s ²
Max travel range	450×450 mm
Static position precision	10 μm

Table 3.1 Design specifications of the PSRM

The 2D SR motor is based on the “straightened-out” version of two 6/4 pole rotary SR motors along both X and Y directions. Due to the reasons stated in Section 3.1.2, the “passive-stator-active-translator” scheme is employed for both axes of motion.

Appendix A defines the parameters and symbols necessary for calculation. To meet with the specifications of maximum force output, from the requirement of maximum loading and acceleration, maximum propulsion force can be developed in each phase according to Newton’s Law as,

$$F_{x(y)} = M_{x(y)} \cdot a = 50 N \quad (3.1)$$

The magnetic parameters can be estimated from the requirement force. At the analytical stage, regardless of saturation effect, propulsion force in linear region can be derived from the following equations [28],

$$f_x(x, i) = \frac{\pi \cdot i^2 \cdot L_\Delta}{p} \cdot \sin\left(\frac{2\pi x}{p}\right) \quad (3.2)$$

$$f_z(x, i) = -\frac{\mu_0 I N^2 i^2 (d - x)^3}{2 z^2} \quad (3.3)$$

where x is the travel distance in X-axis, i is the phase current and $2L_\Delta$ is change of phase inductance from aligned to un-aligned position. The maximum phase current from the motor driver is limited to 10 A; therefore in order to obtain a maximum force of 50 N from the above equations, the maximum change of inductance is 1.5 mH.

In general, L_Δ is a function of motor geometry (d, q, p, l, z). The phase inductance can be represented by the Fourier series. If the first order approximation is considered, the self-inductance is equal to [29],

$$\begin{aligned} L(x) &= L_{ls} + L_0 + L_\Delta \cos\left(\frac{2\pi x}{p}\right) \\ L_0 &= N^2 \mu_0 I N_s C_0 \\ L_\Delta &= N^2 \mu_0 I N_s C_1 \end{aligned} \quad (3.4)$$

where L_{ls} is the phase leakage inductance and N_s is the number of teeth on a primary side pole. The Fourier coefficients C_0 and C_1 for the normalized permeance of one teeth can be found in a standard table [30] of pole-pitch versus air gap length.

The main difference between the PSRM and the LSRM, as far as one axis of motion is concerned, is the stack length l of the silicon-steel plates. Considering the fact that the pole teeth and slots should appear alternatively for the PSRM along two axes while only one axis for a LSRM, for larger force output of the PSRM, the stack length of the mover is chosen to be 48mm. For the PSRM, N_s is equal to 2 and air gap length z is chosen to be 0.5 mm for practical and accurate mechanical alignment.

If $L_{\Delta} = 2 \text{ mH}$ is set to satisfy the maximum force requirement and guarantee a 10% safety margin, then by using $L_0 = 10 \text{ mH}$, the maximum propulsion force of 52.34 N can be evaluated from Equ.3.2. The mechanical dimensions of the proposed PSRM are summarized in Table A.1 in Appendix A. The proposed PSRM has been manufactured according to the calculated dimensions. The photo of the prototype is shown in Fig.3.5.

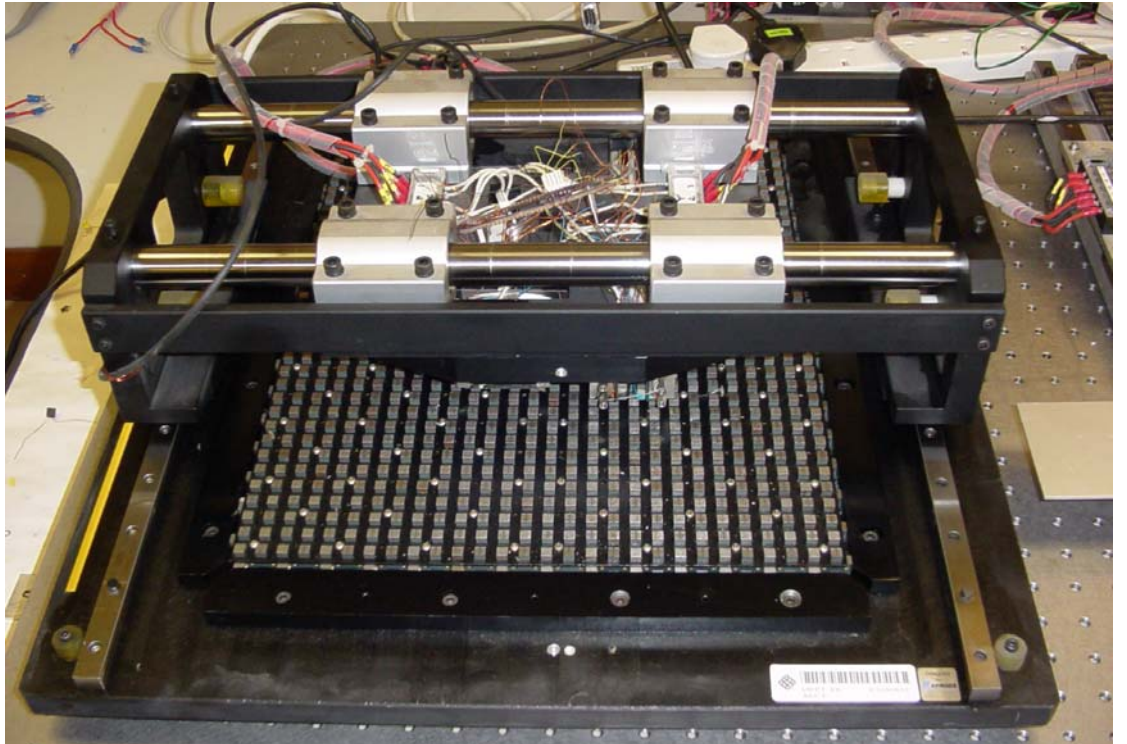


Fig.3.5 Photo of the PSRM

3.4 Construction of the planar switched reluctance motor

Section 2.4 of Chapter 2 describes that existing planar motors are either complicated or expensive. Also, due to the limitations of the base plate, present 2D planar motors cannot be too large.

In an effort to solve one of the problems of planar motors, and to promote the wide spread use of planar motors, a high performance, two dimensional direct-drive planar motor based on SR principle is invented [32]. This motor integrates all the good features of

a SR motor, including a simple and robust structure. The motor construction is shown in Fig.3.6.

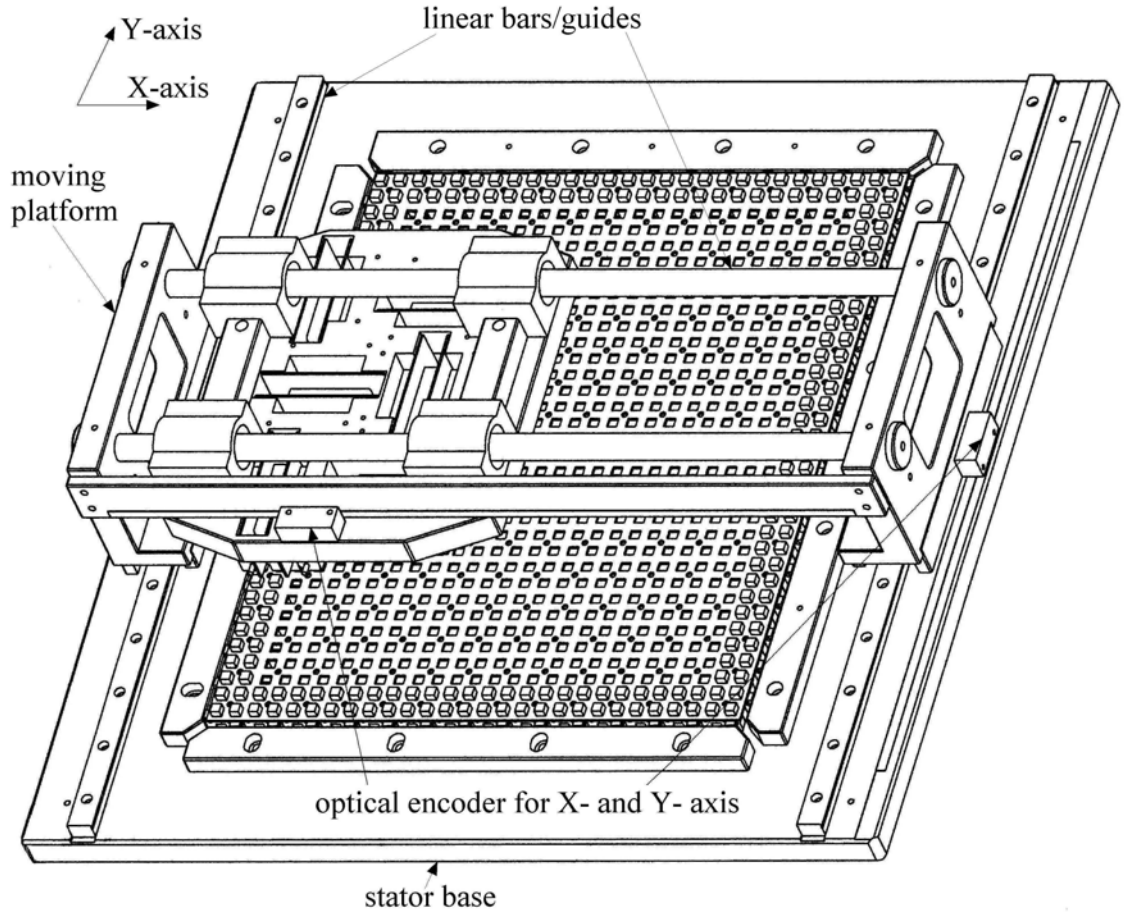


Fig.3.6 Motor construction

The planar motor consists of the following main parts,

- i) The stator consists of an aluminum base with multiple, laminated silicon-steel blocks as described in Section 3.4.1 and 3.4.2.
- ii) Six laminated silicon-steel slots wound with coils with an arrangement that any one slot and its adjacent neighbor are responsible for perpendicular axis of motion as described in Section 3.4.4.
- iii) Two pairs of supporting mechanical sliding bars holding the moving platform and maintaining the air gap and optical encoders mounted on each moving

platform to detect and feedback its real-time position information as described in Section 3.4.3.

3.4.1. The stator

As shown in Fig.3.7, the stator consists of i) an aluminum square base, ii) a pair of sliding guides for Y-axis of motion, iii) stator element matrix, and iv)mechanical holding components.

The stator contains multiple laminated silicon-steel blocks held together by epoxy glue. A rigid aluminum base plate with the dimension of 560 mm×560 mm is made to support the blocks and ensure enough travel range for the moving platform. The aluminum base plate can reduce the weight compared with other types of material substitutes and does not affect the magnetic path at the same time. The holding bars tightly fix the stator matrix in the base slot and they are fastened by lead screws. The function of the aluminum holding plate is to hold all the stator elements together and ensure that all the stator pole extrusions are at the same height.

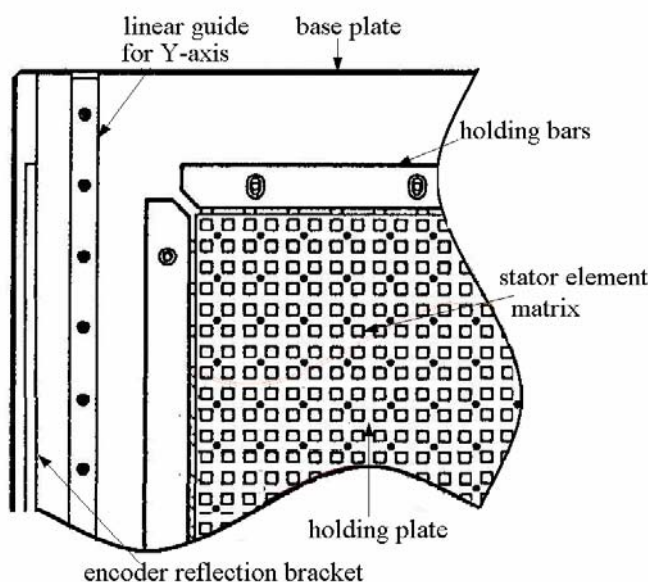


Fig.3.7 The stator base (part view)

3.4.2 Stator building element and matrix

SR machines often use lamination structure to reduce eddy current effect and the phase winding is arranged in such a manner that when excited, flux flows along each lamination and the direction of flux is perpendicular to the direction of the laminations as shown in Fig.3.8 (d). In case of the planar motor, to ensure flux paths for two vertical axes, stacked laminations should be arranged in two perpendicular directions. Therefore, fabrication the whole stator plates from one single slab of sheet would be impossible. An alternative, innovative idea has been proposed, which applies the “*LEGO* block” idea method [32]. The stator is constructed from a combination of magnetic bricks. The basic element is one piece of silicon-steel plate manufactured from a stamping tool.

Starting from one piece of plate (0.5 mm thick), twelve such stacked laminations are pressed together by a standard press tool and fixed with two rivets as one stator block as shown in Fig.3.8 (a), (b). Then the leg extrusion of one block inserts to the leg hole of another block perpendicularly, as shown in Fig.3.8 (c). The other pair can be connected in the same manner as the previous ones. All the four blocks are attached by epoxy glue to form one magnetic brick with a “phalanx” structure as shown in Fig.3.8 (d).

The stator structure uses a “building blocks” approach. With four block elements stacked up as one unit, any number of such units can be generated and combined together to form a whole base of any size and dimension. When the winding for a certain direction is excited, the stator blocks with laminations along that axis are responsible for the establishment of a flux path. As shown in Fig.3.8 (d), flux flows from one block through its leg extrusion to another one at the same position from the “phalanx” structure.

This unique stator structure not only reduces eddy currents, but also makes mass production and flexible customization go well hand in hand. The overall construction complexity and manufacturing cost can be reduced drastically.

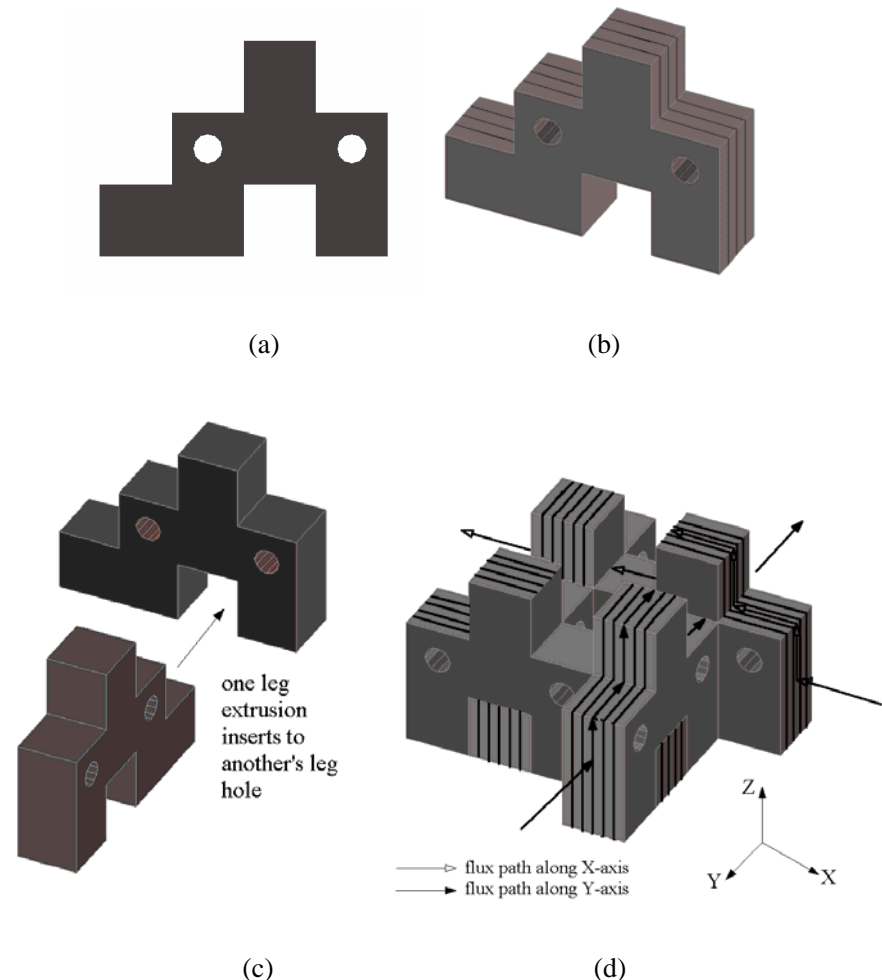


Fig.3.8 Stator (a) lamination, (b) one block, (c) block formation and (d) block combination (bricks) with flux path

3.4.3 The linear guides

Two roller slides are employed to support movement in X-axis, and a pair of high-precision guides is employed for the movement in Y-axis to ensure a smooth sliding motion, and support the massive weight of the moving platform as well. Two linear optical

encoders with $0.5 \mu\text{m}$ are mounted on each moving platform with one piece of encoder reflection bracket that facilitates the optical information.

3.4.4. The mover and the moving platform

A mover body consists of a set of mover plates laminated together with one excitation coil. Like the stator, the mover body for the PSRM is also fabricated from one mould with a pile of 0.5 mm-thick , silicon-steel plates as shown in Fig.A.5 in Appendix 1. Ninety six such plates with 48 mm of thickness are pressed and riveted together to form one mover body after the coil shoe and coil windings are wound on it.

For the PSRM, six mover bodies with two sets of three-phase windings comprise of the moving platform. Altogether there are six coils, with three coils responsible for each direction. Coils for perpendicular force generations are arranged in alternation and mounted on the mover slots with wide magnetic teeth as shown in Fig.A.4 and Fig.A.7 in Appendix 1.

Each mover body along with its corresponding stator blocks below forms the main magnetic path when its coil is excited. All six movers together with windings have the same dimensions and ratings. The six movers are arranged together in the moving platform alternatively to provide each axis of motion as a qualified 2D direct-drive SR machine as shown in Fig.3.9. This arrangement facilitates output forces more evenly along the entire moving platform compared with the “two-linear-motor-combination” structure. For any one axis of movement, the movers conform to the SR principle such that when one is fully aligned with corresponding stator blocks of the stator base, the other two are out of

alignment so that one will move left and the other will move right when activated.

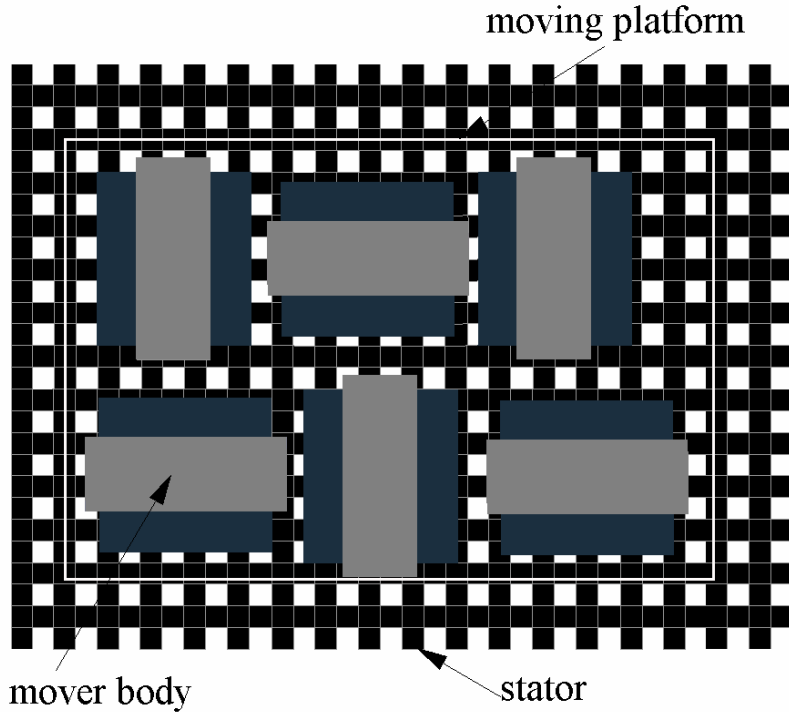


Fig.3.9 Top view of the PSRM

This mover arrangement has many features and advantages. Firstly, the motor winding scheme is simple and straightforward with the structure of individual mover plus winding coil. Compared with the “passive-translator-active-stator” structure, windings on the mover bodies are more applicable to a 2D machine. Therefore the overall manufacture cost and complexity are greatly reduced.

Secondly, zero mutual inductance can be achieved between each adjacent mover with flux-decoupled windings [29]. Each set of three-phase coil generates force in one direction only and two sets of coils are required for the planar motor. The two axes are force-decoupled from each other. The flux-decoupled characteristic between any phase of the mover ensures that any of the six mover coils can be independently activated.

Thirdly, if the moving platform is required to travel a different range, there is no need

to reconfigure the overall motor structure. As long as the former linear bars and guides are replaced with new ones, the motor can be readily adapted to a new traveling distance.

Fig.A.6 shows the construction of the moving platform. For direct-drive of two axes of motion, the moving platform is integrated with one pair of sliding supports. For the convenience of fixture, two high-grade linear sliding rods are applied. Four ball bearings are installed above the moving platform to overcome large normal attraction force between the moving platform and the stator base from current excitations and such an arrangement can also balance the attraction force impressed on the moving platform.

The moving platform is “carved out” with six slots to fit the mover bodies and the coil windings. The back view as shown in Fig.A.7 of the moving platform shows how the six movers are installed in the slots.

3.4.5 Construction of the planar motor

Fig.A.8 shows the assembly of the stator base as shown in Fig.A.2 and the moving platform, as shown in Fig.A.6. From Equ.3.3, in order to produce a force of 50 N, an air gap of 0.5 mm should be used as the optimum air gap length. Smaller air gap can produce higher propulsion force, but it requires higher mechanical rigidity and precision on the linear guides. A finite element method is carried out to analyze the optimal vertical air gap length for the PSRM afterwards in Chapter 4.

From the perspective view of decoupled movements, the thickness of each mover is chosen to be a multiple of the stator pole-pitch to ensure unchanged overlap air gap area and effective magnetic circuit wherever the moving platform resides according to current

excited coil(s) as shown in Fig.3.10. The supporting guides are responsible to overcome the attraction force and remain a uniform air gap space.

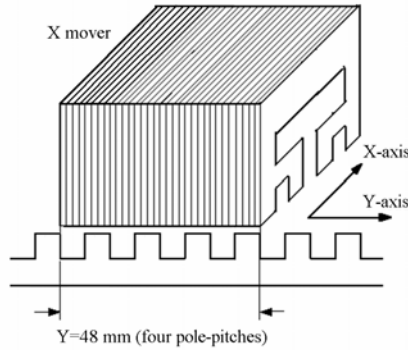


Fig.3.10 Equivalent overlapping air gap area

3.5 Summary of motor characteristics

A novel planar motor based on SR principle is designed and constructed. The motor has a simple and robust structure. The stator base is made from a single piece of ferrite metal, and the laminations of the plural pieces form the stator blocks. Therefore the size and shape of the stator base can be regulated as required. The moving platform is made from simple coil windings and ferrite metal pieces.

Unlike DC brushless drive, no expensive and hard-to-handle magnets are required. The PSRM is a direct-drive actuator, thus mechanical couplings such as lead screws and gears are not required. Compared with traditional X-Y tables driven by DC motors, it is much simpler and less expensive. It is more robust and fault tolerant, and has less overheating problems. The PSRM has a very low maintenance cost.

The PSRM is designed for a 2D motion system that is operated under closed loop control. With the sensors' detection and feedback of real-time information, the degree of

precision is inherent in the motion sensors instead of the mechanical precision of the motor.

Therefore high-precision manufacture routine is not required and special mechanical adjustments are not necessary.

Chapter 4

Performance analysis of the planar switched reluctance motor

This chapter describes performance analysis and prediction of the PSRM. First different analysis techniques are reviewed. Then motor characteristics of zero mutual inductance and force disparities along Z-axis are analyzed with finite element method (FEM). Finally, the experiments corresponding with FEM analysis are carried out to verify the motor performance.

4.1 Review of analytical methods

4.1.1 Energy conversion analysis

Like all electric motors, SR motors are devices that convert electrical energy into kinetic one. However, most standard analytical approaches for AC or DC machines do not apply in SRMs, because the magnetic field inherent in a SR machine is complicated and the coil currents are excited in a pulsed manner. The energy conversion approach starts from the magnetization curve that describes the relationship between flux-linkage and current at different positions. As shown in Fig.4.1, the flux-linkage versus current is usually limited at two special cases—aligned and un-aligned positions. The characteristics for $x = x_i$ is linear because the reluctance of air is dominant for the un-aligned position. Under proper current excitation, the moving platform is magnetized and the propulsion force increases. It

disappears until the mover teeth of the excited phase fully overlap the stator ones underneath and reach position $x = x_2$, the fully aligned position.

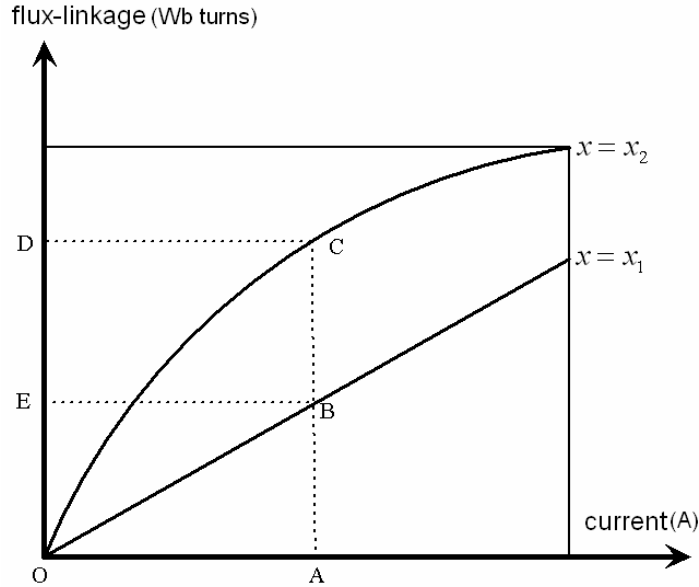


Fig.4.1 Magnetization curve for aligned and un-aligned positions

The electrical input energy is represented as [8],

$$W_e = \int e idt = \int idt \frac{dN\varphi}{dt} = \int Nid\varphi = \int \Gamma d\varphi \quad (4.1)$$

where e is the induced electromagnetic force (*emf*) and Γ is the *mmf*. The input electrical energy, W_e , is equal to the sum of energy stored in the coil, W_f and energy converted into mechanical work, W_m , which is,

$$W_e = W_f + W_m \quad (4.2)$$

where,

$$W_f = \int_0^\lambda i(\lambda, \theta) d\lambda \quad (4.3)$$

The complement of field energy, termed as co-energy, is mathematically expressed as,

$$W_c = \int_0^i \lambda(i, \theta) di \quad (4.4)$$

As shown in Fig.4.1, for motor operation from $x = x_1$ to $x = x_2$, co-energy corresponds to

area OBAO and area OCAO respectively.

For linear machines, the incremental mechanical energy in terms of electromagnetic force and change in position for X direction is described as,

$$\Delta W_m = F_x \cdot \Delta x \quad (4.5)$$

where F_x is the electromagnetic force and Δx is the incremental position in X direction.

Hence the electromagnetic force production, f , of the PSRM for either axis, is given by [25],

$$f_{x(y)} = \left[\frac{\partial W_c}{\partial x(y)} \right]_{i=const} \quad (4.6)$$

The enclosed area OBCO represents the change of coenergy from x_1 to x_2 , which gives the maximum work done for one stroke of the motor. The electromagnetic force can be calculated from Equ.4.6 at a given position with respect to a constant current. Even though the computation of force and work done appears simple and the method is applicable to both linear and saturated situations, the data generation required for their calculation is a complex process, because the relationship of flux-linkage with respect to different positions and excitation currents is hard to predict point by point.

4.1.2 Equivalent magnetic circuit approach

The magnetic structure of the PSRM can be characterized by an equivalent magnetic circuit (EQMC) method [33]. By employing the same philosophy from electric circuitry to represent a magnetic system, analyzing a magnetic system becomes similar to analyzing an electric circuit. With such approach, the relationship between motor parameters such as flux-linkage and propulsion force can be subsequently obtained from calculations. Therefore

it is suitable for the early stage of motor design, because a change in one or some of motor specifications does not involve considerable amount of computation time [25]. Furthermore, in view of performance index, such as cost, efficiency, and weight, etc. can be optimized to meet with the budget requirements. However, this method can only be carried out under linear regions [25]. It also assumes that the approximated reluctance variation for force production is sinusoidal [34].

The equivalent magnetic circuit for one mover under a set of stator teeth at a certain position can be represented as shown in Fig.4.2 below,

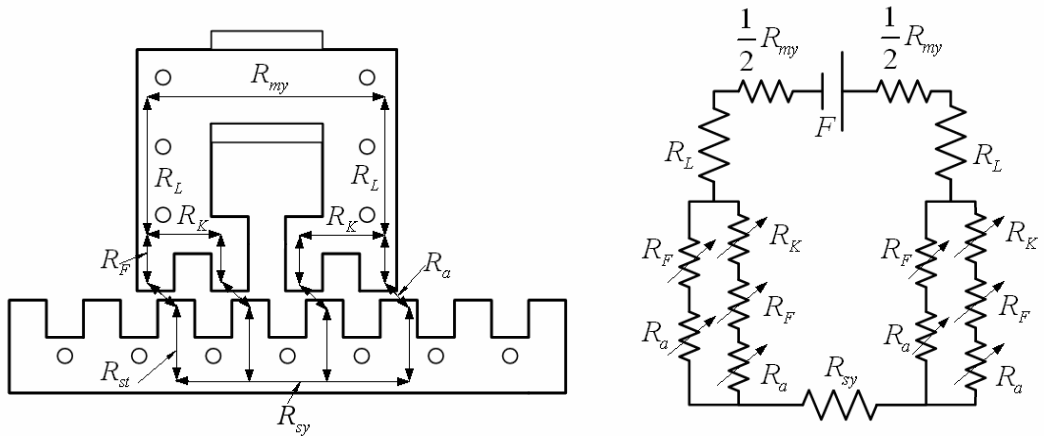


Fig.4.2 Reluctance definition and equivalent magnetic circuit

Accordingly, the above magnetic circuit can be formulated as,

$$\phi = \frac{F}{R_{my} + 2R_L + R_{sy} + 2R_v} \quad (4.7)$$

where $R_v = (R_f + R_a) \square (R_K + R_f + R_a)$.

The reluctance from the above equation of each part of the magnetic circuit depends on flux path, position and material permeability. A precise mathematical calculation of reluctance is practically impossible with uncertain flux paths under different positions. Therefore the above calculation is a rough estimation and it only applies to estimation of the

magnitude range of flux. It is worthwhile to mention that the calculation is more accurate for aligned positions due to the fact that leakage is negligible [25].

One fact has been discovered that flux paths in air between any two surfaces always arrange themselves in such a manner that the maximum possible flux will be produced for a given magnetomotive force, so that the reluctance of the air between the surfaces is minimal [33]. With these basic ideas the designer can sketch the flux distributions for some simple cases. Recently, interests are rising for the analytical prediction of magnetic parameters for some basic magnetic devices [35].

Article [25] has proposed a detailed calculation procedure of air gap flux paths for a LSRM with the “passive-translator-active-stator” structure. The distinct flux distributions add up to ten paths under the fully un-aligned condition. Since the mechanical structure of the PSRM is not uniform along Z-axis, the distribution of magnetic field is more complicated due to end and edge effects. The following assumptions must be met for EQMC method [25],

- i) Hysteresis effect is negligible.
- ii) Magnetization curve is approximately represented by a straight line where μ_r is a constant.
- iii) Flux distributions are uniform over the cross sections of the cores and flux lines enter and leave the iron surface normally.
- iv) The flux lines in the stator and translator poles or yokes run parallel to the longitudinal axis.

For complex situations of magnetic estimation, the magnetic paths are also dependent

on physical parameters of the magnetic circuit such as shape, distance and air gap distribution, etc. Therefore, it can be concluded that the estimation of flux paths for a magnetic device is based on designers' experiences. One important fact is that this method cannot model magnetic machines that operate under saturated region, where it is often the case for SRMs.

Analytical means such as energy conversion and EQMC techniques are no longer capable of computation where there are complicated or irregular geometries, saturation and eddy current effects, especially end and edge effects from three dimensional models. To overcome the above problems and provide a more reasonable analytical solution for the PSRM, a numerical analysis method is applied. Considering both of the advantages and disadvantages of different numerical techniques, the finite element method is by far the most powerful tool for numerical computation of magnetic field, which excels not only in irregular shapes but also in nonlinear materials [36].

4.1.3 The finite element method (FEM)

A powerful FEM software package, *MEGA*, has been introduced for the performance prediction and analysis of the PSRM. This software can be used to model any device which can be described in terms of Maxwell's Equations.

The finite element analysis of the PSRM belongs to the problem of electrical machines. *MEGA* is capable of modeling finite elements in three dimensions [37]. In order to fully inspect fringing phenomena such as end and edge effects, 3D models of the mover and stator are built separately. According to the convention of the FEM tool, the coordinate system for

all finite element models is redefined. The X-axis is defined as horizontal; the Y-axis is defined as the vertical direction and Z-axis as the direction vertical to the X-Y plane. The whole motor model is combined with the mover and stator meshes by Lagarange multiplier [38]. The mover is also defined as the moving 3D object relative to the stator with a number of movement steps.

Since the motor tends to enter saturation region with nonlinear permeability under real operation, “transient problem” is defined in the finite element models of the PSRM and each intermediate answer is solved by the time-stepping techniques [36]. A proper coil model in three dimensions with different current levels is selected from a standard coil library in the software package as the input excitation.

The chief objective of finite element analysis is to obtain the relationship of flux-linkage and inductance with respect to different currents and positions. Through this exercise, the motor performance can be fully determined. Then force profile can be derived from these solved magnetic variables.

4.2 Meshing of the planar switched reluctance motor

Before the finite element modeling of the motor, the physical parameters of the moving platform, stator and air gap are determined from the previous chapter. Fig.4.3 shows the 3D finite element models with mechanical specifications of each part.

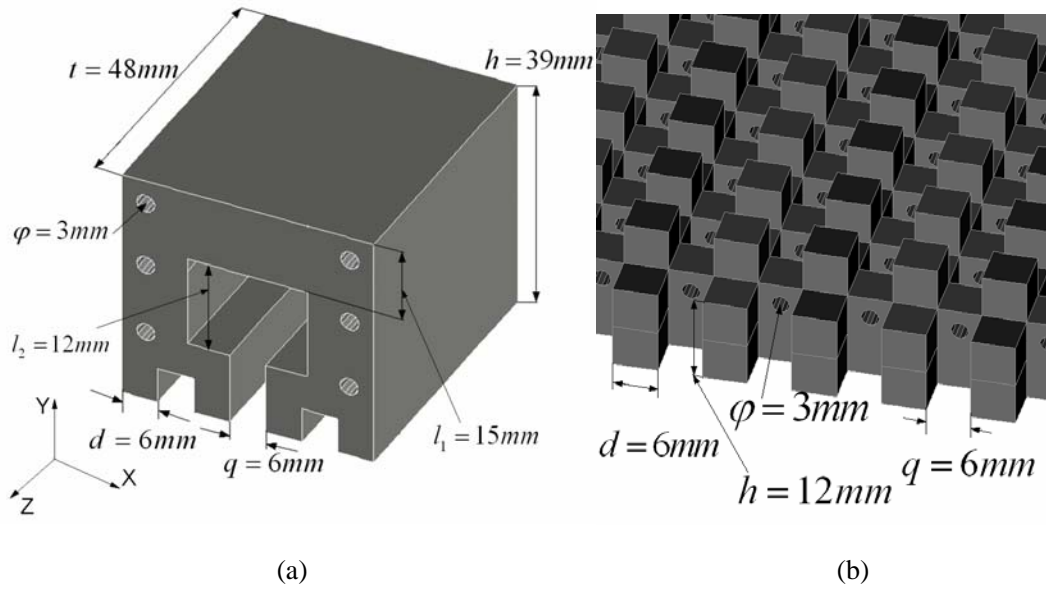
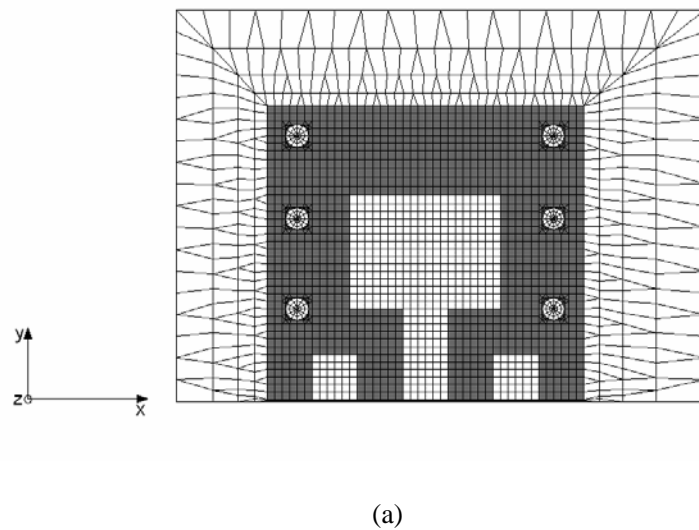


Fig.4.3 3D finite element models of (a) one mover and (b) stator

As shown in Fig.4.3, the 3D models are built by extruding a base plane along the Z-axis. A base is first constructed in the X-Y plane as a 2D framework of nodes and elements. This structure includes quadrilateral or triangles with each edge defined by two nodes. The field distribution is the key factor that affects the distribution of finite elements. Where the rate of change of field is greater, the elements should be fine enough otherwise the answers at these nodes will not be accurate.



(a)

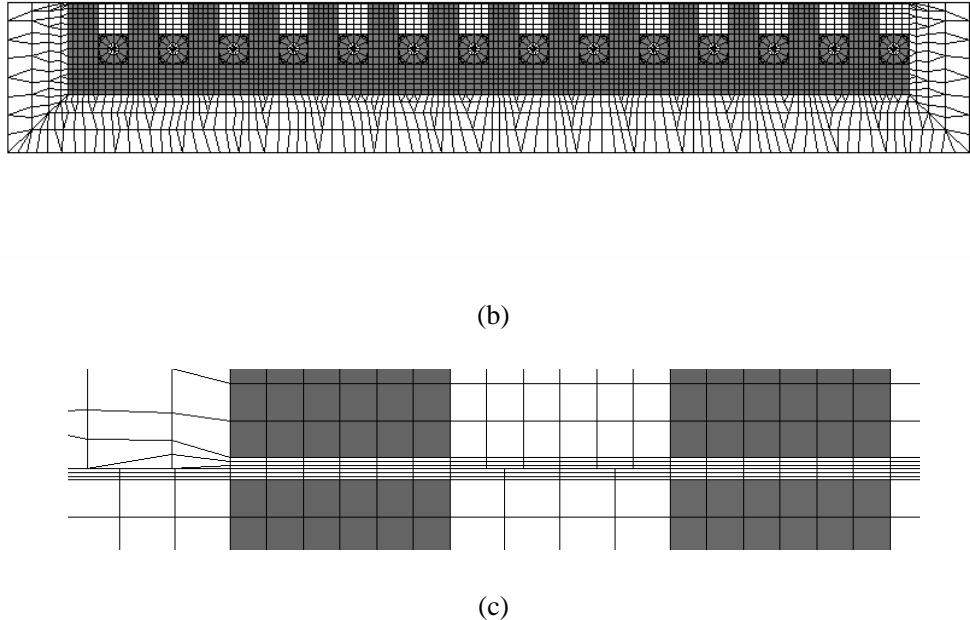


Fig.4.4 2D meshes of (a) the mover, (b) the stator and (c) the air gap

As shown in Fig.4.4 (a), the 2D meshes for one mover is represented with 2,474 nodes and 2,642 finite elements. The stator base plane is modeled in the same way with 3,739 nodes and 3,961 elements as shown in Fig.4.4 (b). Considering the software limitation and the fact that sharp change occurs around the regions with different relative permeabilities, discretisation should be reasonably fine for the meshing of air gap region since magnetic variables depend much on the flux densities around the corners of the mover and stator poles as shown in Fig.4.4 (c). After 2D model is set up, 3D mesh can be created level by level from the base plane. The model contains sufficient detail to define all the changes that occur along the Z direction to form a series of similar spaced planes having the similar discretisation. With reasonably fine discretisation resolution from the 2D model, the number of nodes and elements quickly becomes very large with the projection in the Z-axis. Altogether there are 17 levels with nodes and elements to 150,489 and 153,180 respectively. The coil elements

can be expressed in 3D from this software package. As shown in Fig.4.5, the type of “race track” coil is chosen to simulate the real winding from a variety of coils in the software library. The coil is “wound” on the mover yoke and current distribution is uniform over the entire coil cross sectional space. Though meshing is not needed for the coil, it should be embedded as reduced scalar elements and the region where the finite elements reside with this coil should be represented as reduced scalar potentials [38]. The magnetic field due to the source current is derived from Biot-Savart Law [37],

$$H_s = \frac{1}{4\pi} \int_v J_s \times \nabla \left(\frac{1}{r} \right) dv \quad (4.8)$$

where r is the distance between the current source point where the field is calculated, J_s is source current density and v is the current-carrying volume. The actual field is the sum of the source field and the gradient of a “reduced scalar potential” [36],

$$H = -\nabla \phi + H_s \quad (4.9)$$

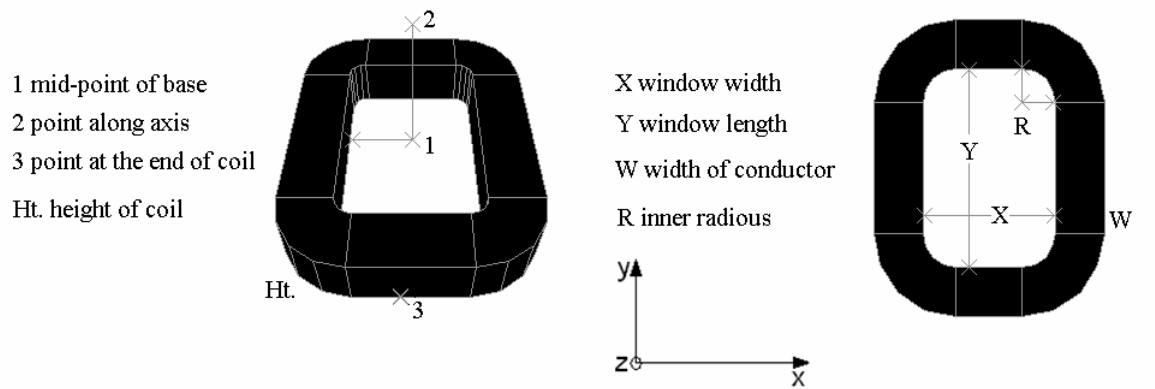


Fig.4.5 The race track

After the definition of the winding coil, the two models are joined together and displacement of one pole-pitch (12 mm) can be defined for the mover relative to the stator as shown in Fig.4.6.

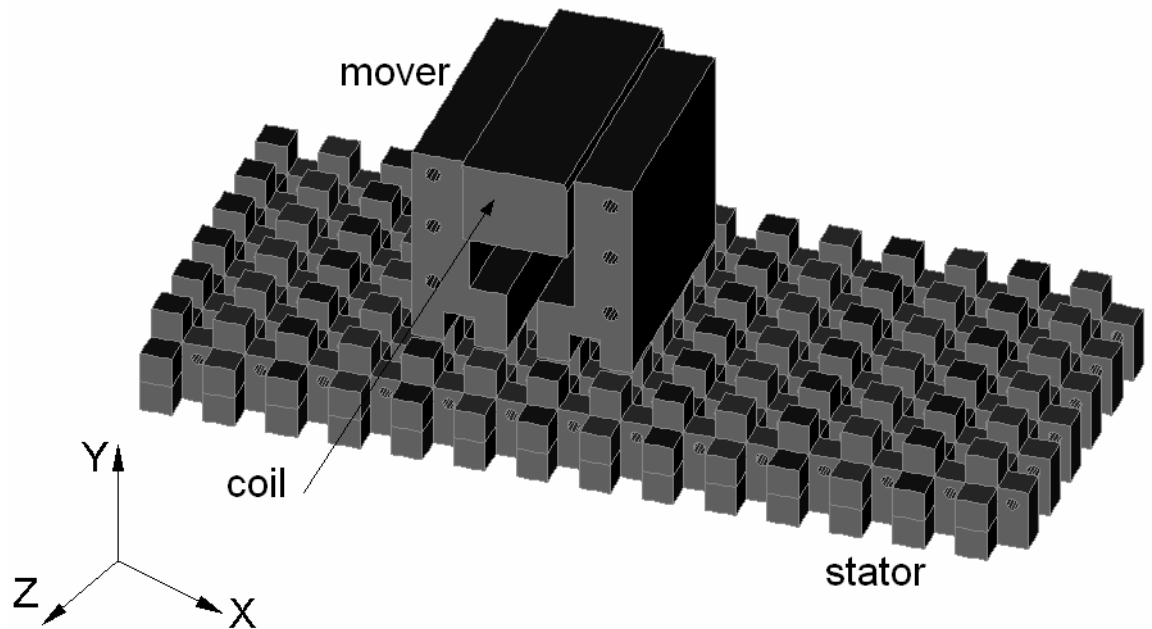


Fig.4.6 The complete 3D finite element model

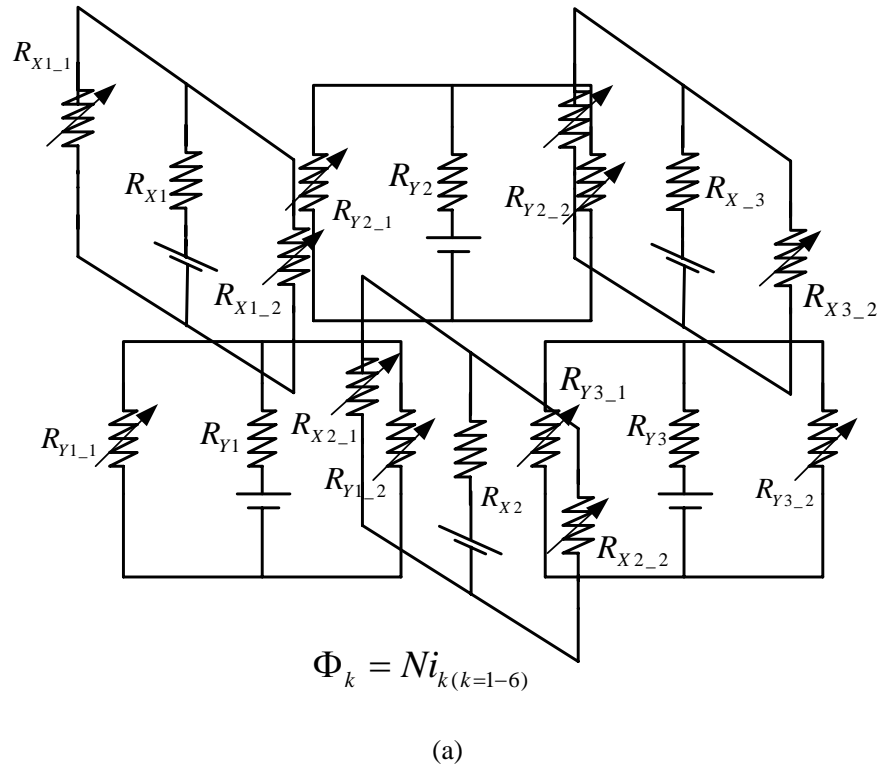
4.3 Test of zero mutual inductance

Mutual inductance between any two movers is first observed. If the coupling effect is negligible, the procedure of finite element modeling can be greatly simplified by building only one mover with a number of stator sets. Future control schemes can also be straightforward without any decoupling strategy involved. The test of zero mutual inductance is conducted by i) EQMC, ii) FEM and iii) experiment verification. They are described in Section 4.3.1, 4.3.2 and 4.3.3, respectively.

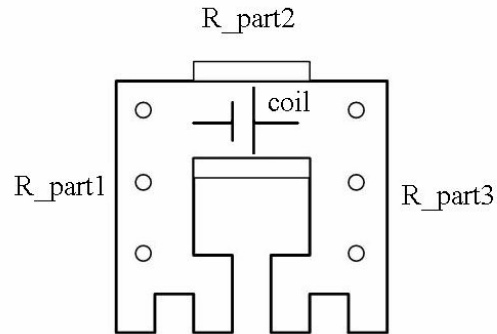
4.3.1 The equivalent magnetic circuit method (EQMC) approach

From motor specifications, all six movers are identical with the same reluctance for each part of the mover body and the equivalent magnetic circuit of the six movers is drawn

together as shown in Fig.4.7 (a) with the reluctance defined in Fig.4.7 (b). It can be seen that reluctance is a position function of the activated mover(s) [27, 29]. Since flux path distribution is determined by the value of relative permeability (μ_r), as one mover is excited, flux circulates the path along the mover body of its own with a higher μ_r , compared with the path across any adjacent mover bodies.



(a)



(b)

Fig.4.7 (a) Equivalent magnetic circuit of the movers (b) reluctance of the mover

4.3.2 The finite element method (FEM)

To further verify the fact that any of the two movers are flux-decoupled, a finite element method is performed. To precisely represent and solve the problem, the three dimensional model has been constructed with one mover and its closest neighbor. As shown in Fig.4.8, magnetic flux merely distributes within the short magnetic path among the mover with its excitation coil at 8A, the stator area and the air gap space between them. This is because the magnetic path between the two adjacent movers has as large reluctance as air.

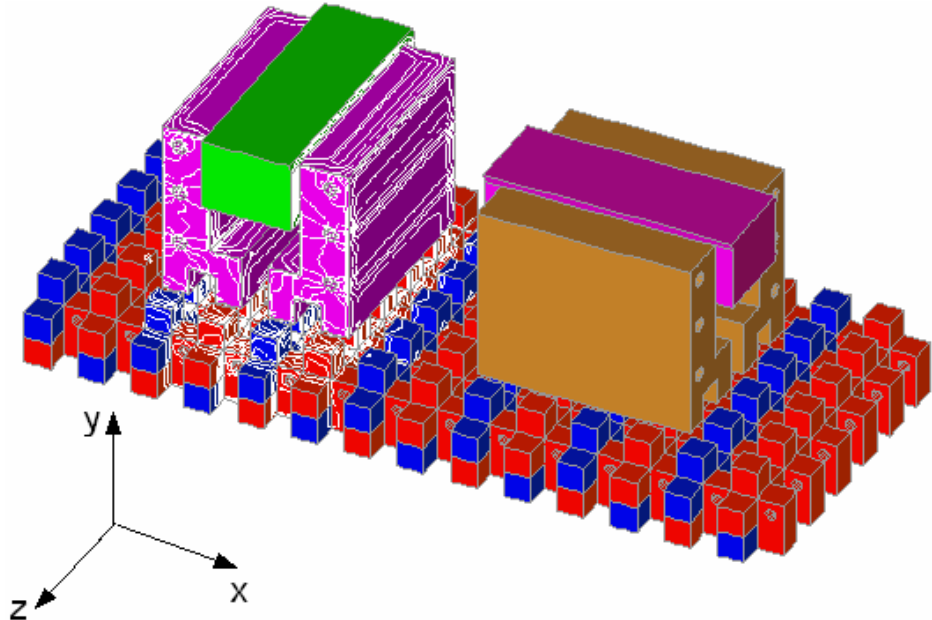


Fig.4.8 3D FEM model for mutual inductance test

For a precise numerical analysis, a 3D cut vertical to the Z-axis has been performed along the 3D finite element model. Then a 2D contour plot of flux distribution is derived as shown in Fig.4.9. After the finite elements of the air gap area between each mover and its corresponding stator are selected, the relationship of flux for each part according to its relative position can be obtained. From Fig.4.10, it can be concluded that the coupling effect between any two movers is negligible.

Although the above verification is performed at the aligned position for the mover relative to the stator, the relative distance between any of the two mover bodies are fixed regardless of mover positions. Even though flux distribution changes with different mover positions, however, from the FEM result the short magnetic path dominates among the mover with its excitation coil, the stator area and the air gap space between them with relative smaller reluctance. Therefore, the above analysis is also applicable for other positions.

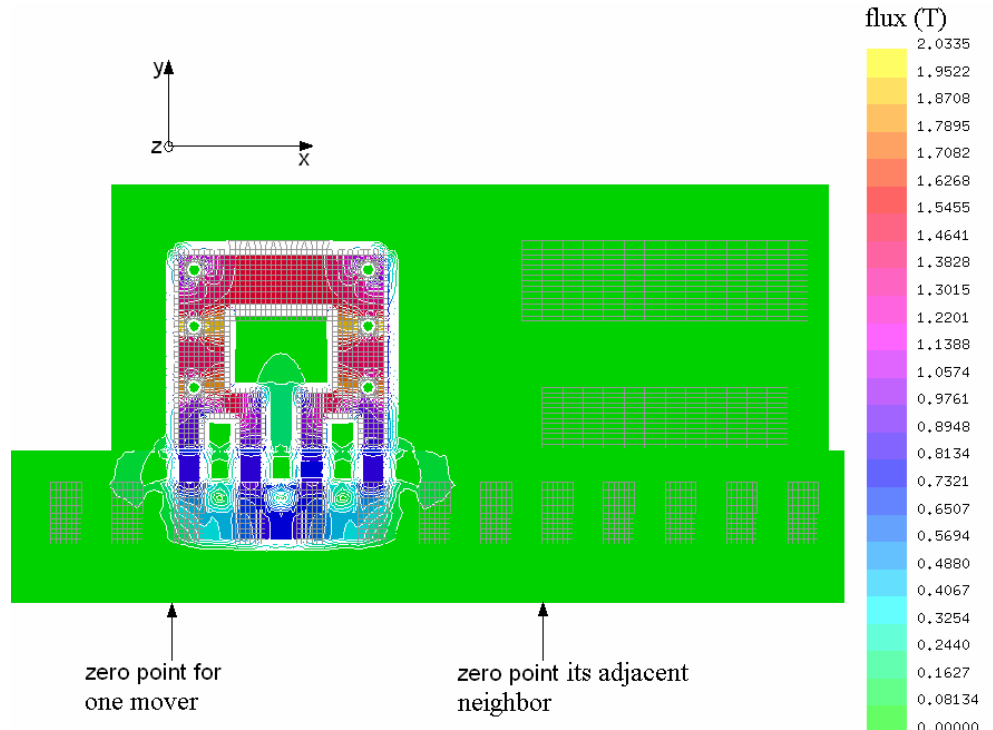
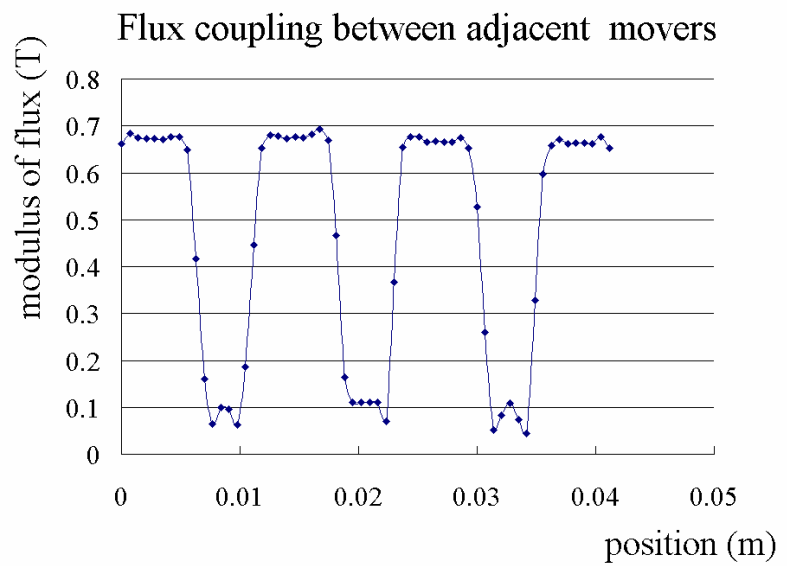
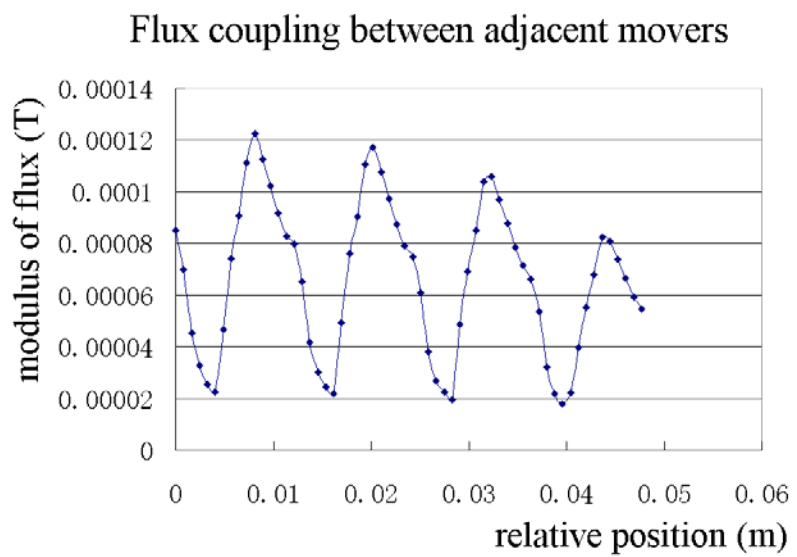


Fig.4.9 2D flux distribution from one activated mover at 8A



(a)



(b)

Fig.4.10 Flux distribution when one mover is activated at 8A for (a) one mover (b) its adjacent neighbor

4.3.3 Experiment verification

Together with FEM, an experiment that verifies the mutual coupling has also been conducted [31]. Fig.4.11 shows the input sinusoidal voltage to any one coil from the six mover coils and the induced output voltage from its closest neighbor coil. The output of the induced voltage is virtually zero.

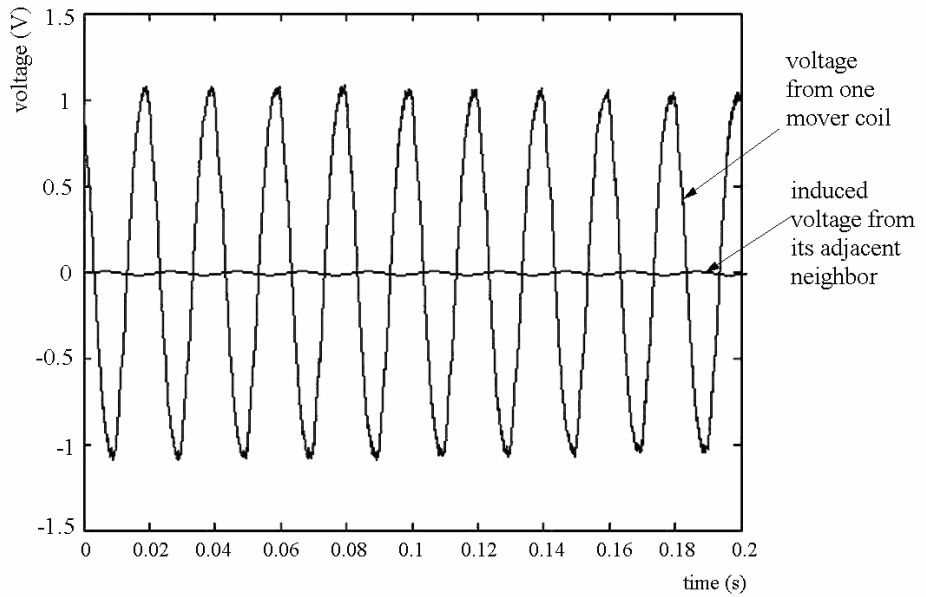


Fig.4.11 Coupling effect between the closest windings

4.4 Force disparities along Z-axis

The direction of movement for the X mover is defined as the X-axis. As long as one of the three movers for X direction is excited, the moving platform will encounter the force vertical to the moving direction. The vertical force along the moving platform is assigned as Z-force and the other, which is vertical to the moving plane, Y-force or normal force.

The end and edge effects play an important role in the SR motors. In normal motor operation, the moving platform will encounter a three dimensional force when current is

excited in X, Y and Z directions. The force generation that drives the motor moving in X direction is a collective contribution of electromagnetic force of X component together with longitudinal end effects. The values of end effects depend on different positions of the corresponding mover relative to the stator base and exciting current [39]. It causes a distortion of flux field distribution and directly affects force output performance. The worst case occurs in the extreme end of the mover. Fig.4.12 provides a schematic flux distribution of end and edge effects.

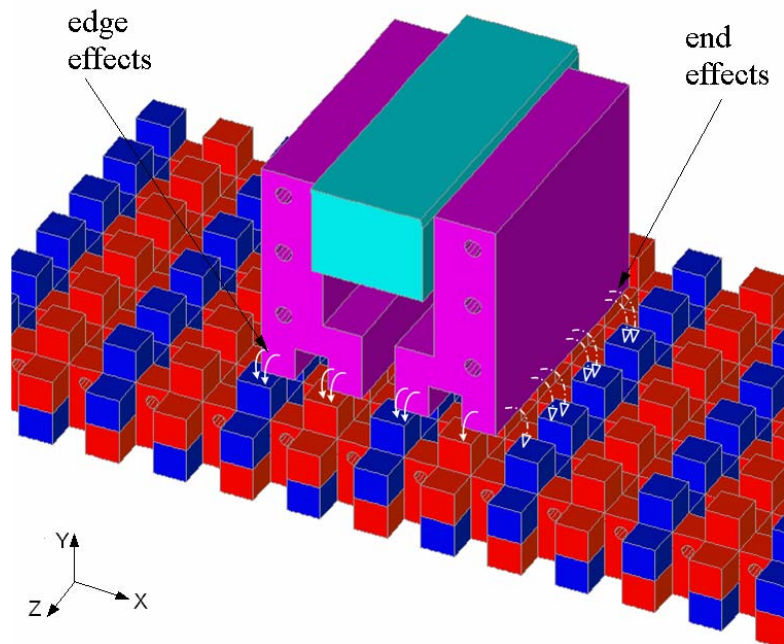


Fig.4.12 Longitudinal end effects and transverse edge effects

For RSRMs or LSRMs with one degree of freedom, transverse edge effect has no impact on the overall performance, since the rotor or the moving platform is locked along the axis perpendicular to the direction of movement. However, this is not the case for the PSRM. When the PSRM is activated, the resultant electromagnetic force of X and Z directions tends to skew the moving platform. It can be seen that the edge effects differ according to distinct relative positions from the moving platform to the stator along Z-axis. The Z-force

disparities are unique to the PSRM, and it mainly results from the transverse edge effects. For the PSRM, a thorough inspection should be carried out to verify the different values of edge and end effects and check whether they are large enough to take into account for control algorithms. This investigation is conducted by both FEM and experiment verification and each is described in Section 4.4.1 and Section 4.4.2, respectively.

4.4.1 The finite element method

To investigate the edge effects accurately, a 3D finite element model is built. A complete relationship between Z-force disparities respect to different X and Z positions are described in a 3D manner, and a position of $X=3$ mm from one mover according to the stator teeth is studied. By using a position increment of 1 mm, the analysis is performed with one mover at six discrete locations within half pole-pitch. Then the electromagnetic force at each location is calculated. Fig.4.13 shows the 2D side view of the finite element model at six positions.

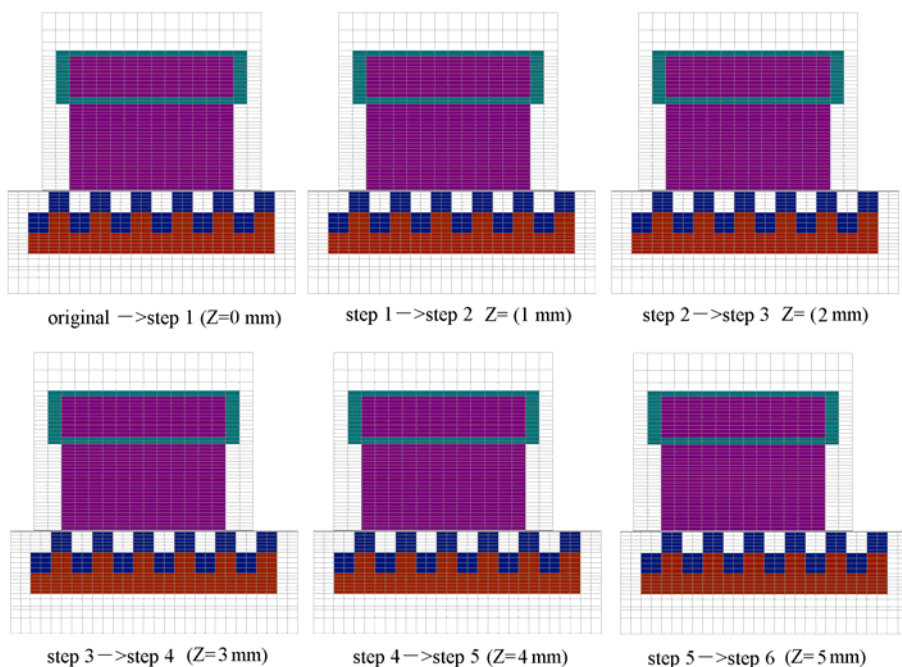


Fig.4.13 Side view of the PSRM with a six-step sequence

Fig.4.14 shows the FEM results. It is obvious that for a constant current level, Z-force disparities occur at two “extreme conditions” with the mover at $Z=0$ mm and $Z=5$ mm. Except for these two positions, edge effects are dominant on both the front and back side of the mover and they counteract with each other. It can also be seen that Z-force values distribute symmetrically at position of $Z=3$ mm. This is because the edge effects from both sides of the mover are identical with opposite force values and they can cancel each other.

Although maximum Z-force disparity is about 2.5 N at 10A excitation, from the finite element analysis of propulsion force in the following chapter, it is only 7.5% of the maximum propulsion force at 10 A. Therefore no extra decoupling mechanism is required to compensate Z-force disparities.

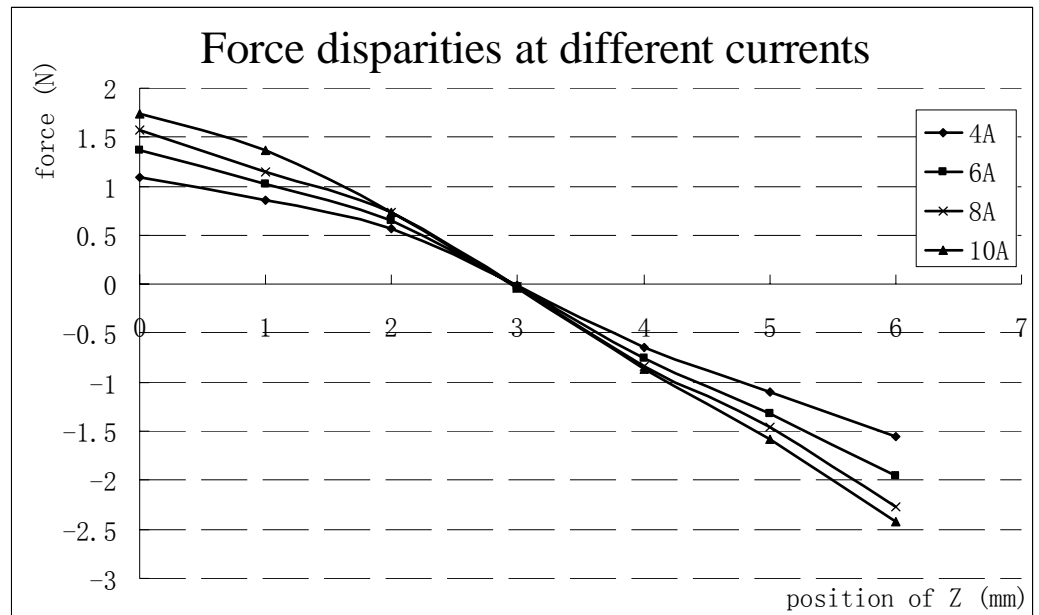


Fig.4.14 Force disparities along Z-axis at fixed X position ($X=3\text{mm}$)

4.4.2 Experiment verification

To further test whether force disparities place a burden on control algorithms,

experiment for Z-force measurement is carried out. As shown in Fig.4.15, with the mover of Y-axis at position of X=3 mm, there is certain amount of force shifts for different Z positions. However, these minor force offsets will not influence the performance of the motor along X-axis. The main reason is because the electromagnetic force generated along Z-axis from edge effects is not strong enough to overcome static frictions. Therefore the mover is considered to be decoupled in both X and Z directions.

Under the overall test, the sensor output from another axis remains unchanged and this ensures the motor to remain stationary along X directions at all times.

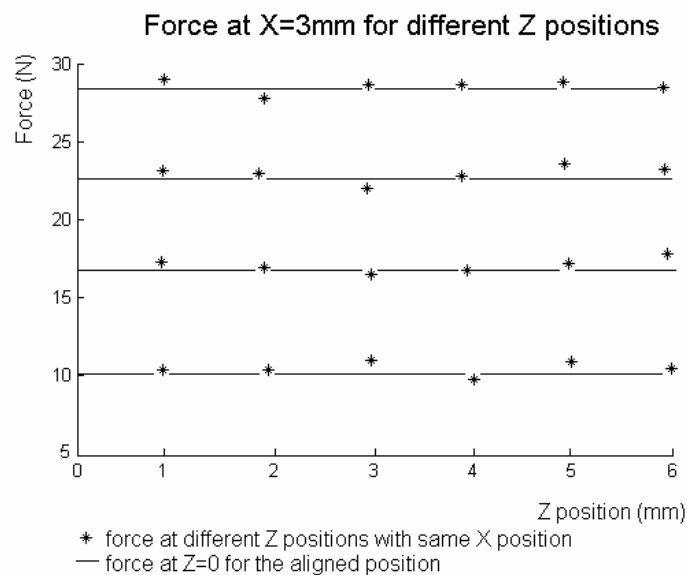


Fig.4.15 Force variations of Z-axis

4.5 Calculation of normal force (Y-force)

Section 4.5.1 discusses the determination of air gap lengths between the moving platform and the stator base. The calculation of normal force at different air gap lengths are estimated with FEM, as described in Section 4.5.2.

4.5.1 Determination of air gap lengths

The air gap length directly determines the values of normal force and it is a very important factor for motor design aspect. Determination for a proper length relies on many motor parameters, operating conditions and design requirements. The effect of air gap length on the electromagnetic force of each phase for the linear region is derived from Equ.3.3 in Chapter 3. It can be seen that propulsion force is inversely proportional to the square of air gap length with other variables unchanged. However, merely decreasing air gap length will lead to square growth of normal force. This lays a heavy burden on the supporting guides and causes mechanical distortion. This will further lead to the decrease of air gap lengths and worsen the attraction between the moving platform and stator base. This must be avoided for a proper machine design. The manufacturing tolerance for the minimum air gap support is another important factor to be considered. It determines the magnitude of uneven pull on the mover and hence the wear, tear and longevity. During motor operation, any one or several coils may be excited simultaneously from the requirement of control algorithms, and the unevenly distributed attraction force impressed on the linear guides affects the air gap distributions, so it is very hard to maintain a uniform air gap for the entire air space between the moving platform and the stator base, especially under large current excitation circumstances.

4.5.2 Finite element analysis of normal force

Since it is difficult to mount any sensor among the air gaps for an accurate measurement of normal force, the analytical method is used to calculate the effect of different air gap

lengths on normal force outputs according to different positions.

The 3D finite element model is built and a group of air gap lengths from 0.4—0.7mm are taken into consideration. Normal force according to different air gap lengths is drawn in the same figure as shown in Fig.4.16. The maximum normal force always occur at fully aligned positions ($X=0$ mm) for each air gap length.

From the simulated results the appropriate supporting guides for the PSRM can be selected. The finite element method may give larger values compared with experiment measurement since the finite element model ignores some real-world parameters, however this is still a feasible reference for the provision of a certain margin for linear guide selections. Considering the maximum supporting capability from the specifications of the linear guides, current air gap is regulated as about 0.55—0.6 mm.

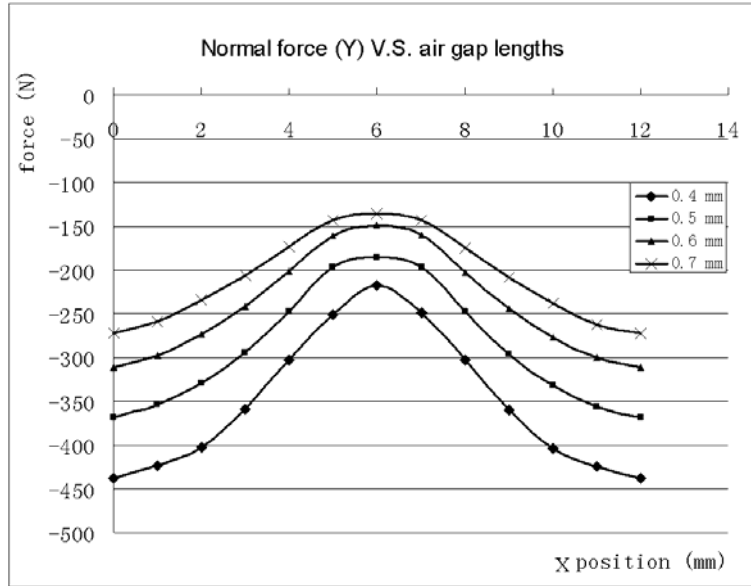


Fig.4.16 Normal force at different air gap lengths

4.6 Analysis and measurement of propulsion force (X-force)

Analysis of propulsion force is first conducted by FEM as described in Section 4.6.1.

Then measurement of the propulsion force is carried out with experiment as discussed in Section 4.6.2.

4.6.1. Calculation from FEM

Force at a given position is obtained by Maxwell Stress Method for a certain current. Among the three popular numerical methods of force calculations, the Ampere's Force Law though only deals with nonmagnetic conductors, can be used to find force distributions [40]. The Maxwell Stress Method and the Virtual Work Method are equivalent for a certain common cases [41].

The 3D finite element model is built as shown in Fig.4.6. The 2D propulsion force profile according to different positions within one pole-pitch with respect to different current levels is shown in Fig.4.17. From the diagram, it can be seen that at lower current excitations, maximum force occur at the position of half pole-teeth (3 mm or 9 mm, etc) and the waveforms are sinusoid-like curves. At higher current levels, such as 9A or above, the waveforms become distorted that force climbs to peak earlier and the maximum values appear before the mid pole-teeth within one pole-pitch from the fully un-aligned position to fully aligned position. This is because the magnetic materials have entered saturation region and the interaction becomes dominant accompanied by much more end effects. From the contour in Fig.4.18, the saturation effect becomes pronounced with a current excitation of 15A.

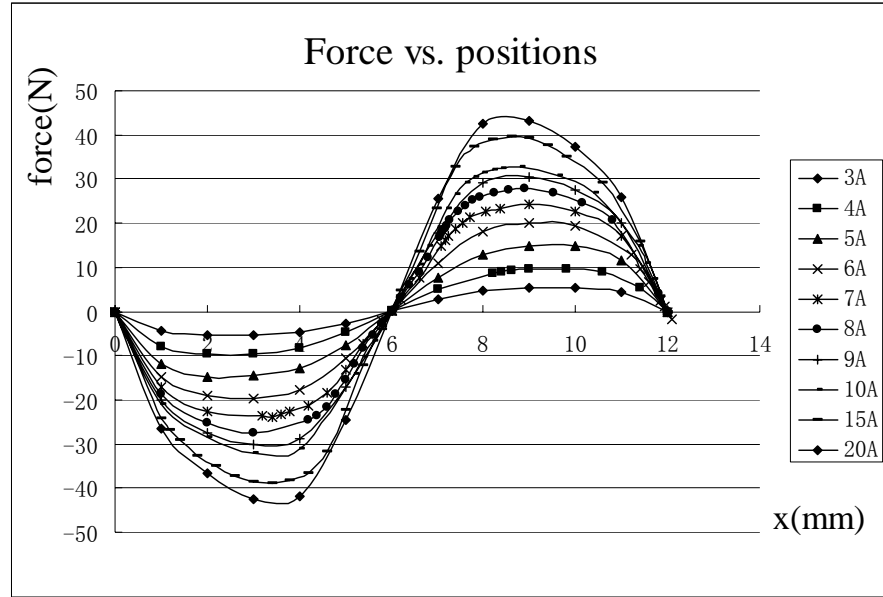


Fig.4.17 Propulsion force at different positions with respect to current

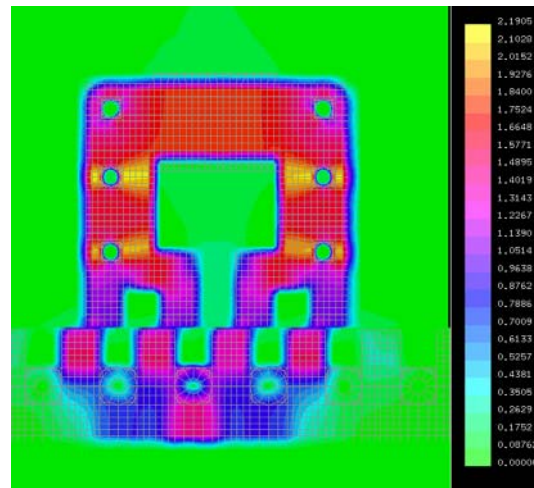


Fig.4.18 Saturation effect with higher current excitation

4.6.2. Measurement from experiment

Force experiment is conducted by a sensitive load cell. The load cell has a resolution of 274.65mv/50N. As shown in Fig.4.19, a test-rig fixture is installed to divide accurately one pole-pitch into a number of divisions finely enough [42]. An interface circuit has also been built for signal amplification and transfer of delicate sensored voltage output to the A/D channel of the DSP. Position information is fed back to the PC from the optical encoder. The

various input current excitations are provided with a generalized current driver [43]. Since a certain length of time should be taken for the load cell to settle, to prevent overheating of the coil and damaging the load cell, a current range of 1—10A is selected. When all the signals are ready, they are sampled consequently into the PC for further data processing. Fig.4.20 shows the whole experiment setup.

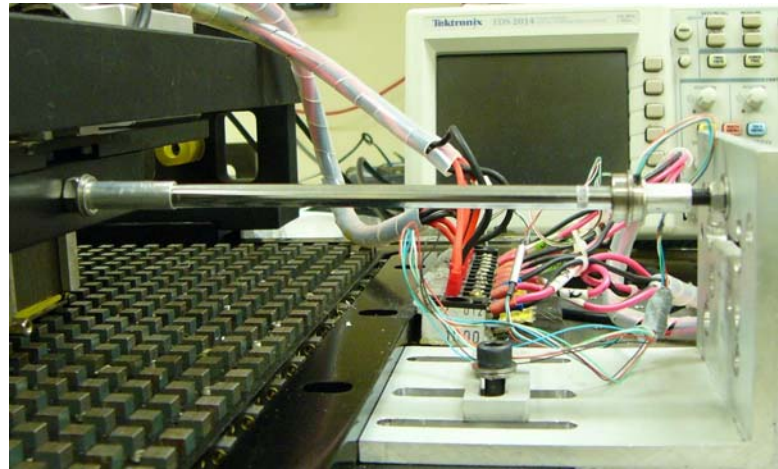


Fig.4.19 Load cell and the test-rig

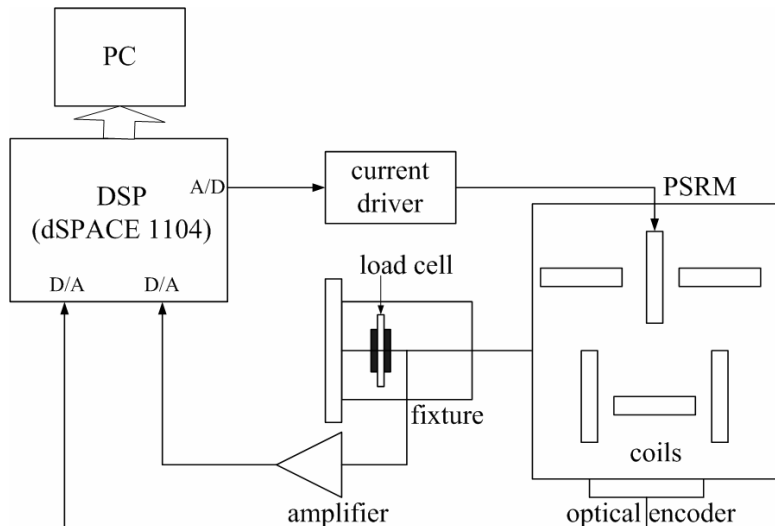


Fig.4.20 Experiment setup of force measurement

Force from one of the movers in Y-axis of movement is recorded and the result is shown in Fig.4.21. It can be seen that measurement results of propulsion force correspond with the FEM result. The waveform distortion from saturation effect is also apparent. The propulsion

force from FEM and experiment is drawn together in the same figure to show the difference between the FEM and measurement results. The main difference shows that under the same current excitation, force output is comparatively smaller than that of FEM. This is mainly due to the static frictions from the sliding support.

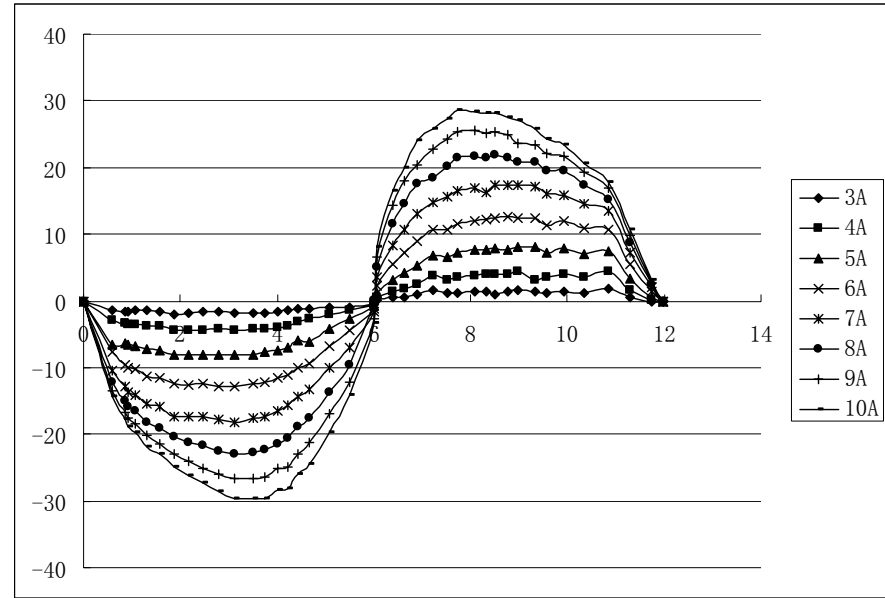


Fig.4.21 Force output from experiment measurement of Y-axis

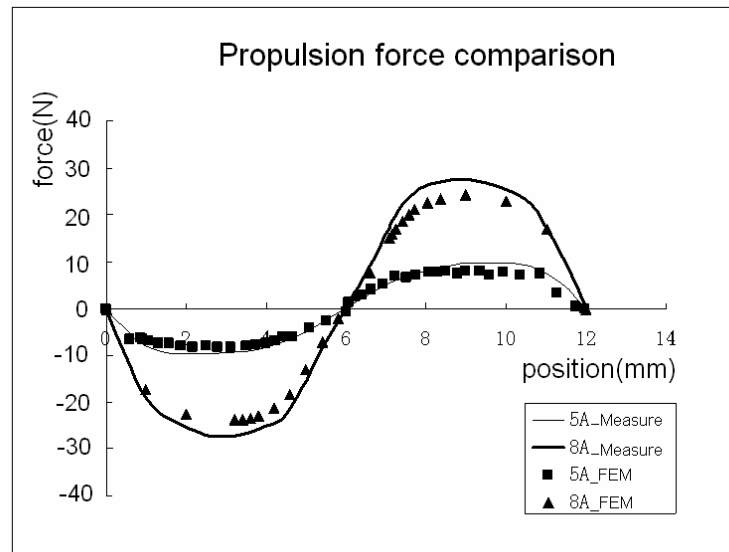


Fig.4.22 Force comparisons at 5A and 8A from FEM and experiment

4.7 Summary

In this chapter, parameters regarding to motor characteristics have been carefully examined. Compared with different analysis techniques, the finite element method is selected as an appropriate tool. Throughout the analysis, 3D model is used for an accurate simulation result. First, test of mutual inductance has been carried out and the simulation result is verified with experiment measurement. Then the effect of Z-force disparity unique to the 2D motor is studied and corresponding experiment is also performed. Both FEM and experiment results show that the effect of Z-force is negligible and there is no need for the introduction of any decoupling control mechanisms in Z-axis. Next the analysis toward air gap length selection is performed with FEM and normal force according to different air gap lengths is simulated. Lastly, the propulsion force for one axis is simulated with FEM and experiment results are provided for Y-axis due to less friction. Both the data from simulation and the experiment results correspond with each other well. From these detailed characteristic information, a model of the PSRM can be constructed for the controller design and simulation purposes. This will be described in the next chapter.

Chapter 5

Characterization and modeling of the switched reluctance motor

The performance characteristics of a SRM are determined by the relationship of flux-linkage vs. its positions and phase currents [8]. In order to evaluate the flux-linkage and obtain the characteristics of the PSRM, various flux-linkage measurement methods are reviewed and characterization experiments are conducted. In addition to the flux-linkage measurement, other characterization measurements such as hysteresis and leakage flux-linkage are also conducted.

The objective of modeling the PSRM aims at the construction of a mathematical model for the controller design and simulation purposes. The model of the PSRM is based on the nonlinear flux-linkage characteristics and a set of state-space equations. The model is compared with the results from measurement, and it is confirmed to be accurate.

5.1 Motor Characterization

Flux-linkage characteristics of a SR motor is related both to the change of relative positions and to the change in current levels. Therefore it is a three dimensional function with respect to both current and position [8]. When the mover teeth are aligned with the stator poles, the reluctance of the flux path is at minimum. When the move teeth begin to move away from the stator poles, the reluctance is getting higher and the flux-linkage value

is reduced. The measurement of flux-linkage vs. different positions with current as a parameter is of great importance since it reflects the performance of the machine.

5.2 Review of methods in obtaining the magnetic characteristics for switched reluctance motors

In general, the study of magnetic characteristic determination does not begin from the inductance measurement, since previous method [44] is limited to low-power rated machines and requires additional equipment to superimpose an AC signal on a large DC current that is injected into the motor phase. Furthermore, this method is not applicable for all operation conditions.

Another method of determining magnetic flux is to employ flux sensors and measure the flux inside the motor directly [45]. This method is seldom used due to the following reasons [46],

- i) It requires sensors to be installed at the stage of motor assembly.
- ii) The flux sensors are very expensive.
- iii) The flux sensor is not capable of measurement for a wide range of flux variations.

Therefore, the most preferred method is to measure flux indirectly by voltage and current data from the phase winding(s). Various approaches of measurements have been attempted and proposed [8, 46, 47]. Two methods are commonly in use and they are reviewed in Sections 5.2.2 and 5.2.3, respectively.

5.2.1 Mathematical model of the planar switched reluctance motor

The electrical characteristics of the PSRM for any one mover of either axis can be described as the combination of a resistive and an inductive structure as shown in Fig.5.1.

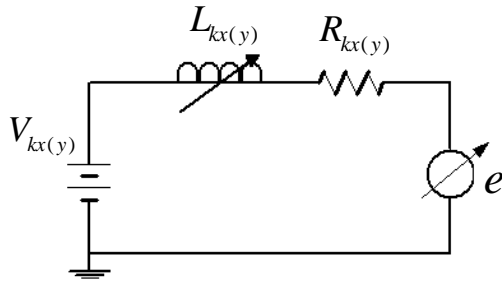


Fig.5.1 Equivalent electrical circuit

The voltage equation can be expressed as,

$$V_{kx(y)} = R_{kx(y)} \cdot i_{kx(y)} + \frac{d\lambda_{kx(y)}(s_{x(y)}, i_{kx(y)})}{dt} \quad (5.1)$$

where $V_{kx(y)}$, $R_{kx(y)}$, $i_{kx(y)}$ and $s_{kx(y)}$ is terminal voltage, coil resistance, current and position.

Symbol $x(y)$ stands for X-axis or Y-axis. Generally $\lambda_{kx(y)}$ is the total flux-linkage and can be regarded as the sum of self $\lambda s_{kx(y)}$, mutual $\lambda m_{kx(y)}$ and leakage flux-linkage $\lambda l_{kx(y)}$. For the PSRM, as mentioned before, mutual flux-linkage can be regarded as negligible.

Equ.5.1 can be further expressed as,

$$V_{kx(y)} = R_{kx(y)} \cdot i_{kx(y)} + \frac{\partial \lambda_{kx(y)}}{\partial i_{kx(y)}} \cdot \frac{di_{kx(y)}}{dt} + \frac{\partial \lambda_{kx(y)}}{\partial s_{x(y)}} \cdot \frac{ds_{x(y)}}{dt} \quad (5.2)$$

where

$$e_{bemf}(i_{kx(y)}, s_{x(y)}, \dot{s}_{x(y)}) = \frac{\partial \lambda_{kx(y)}}{\partial s_{x(y)}} \cdot \frac{ds_{x(y)}}{dt} \quad (5.3)$$

For low speed operations where the back EMF e_{bemf} can be omitted, Equ.5.2 can be further simplified as,

$$V_{kx(y)} = R_{kx(y)} \cdot i_{kx(y)} + L_{kx(y)} \frac{di_{kx(y)}}{dt} \quad (5.4)$$

In the mechanical side, the equation that governs the dynamic behavior of the machine can be expressed as,

$$M_{x(y)} S''_{x(y)} + B_{vx(y)} S'_{x(y)} + f_l = F_{x(y)} \quad (5.5)$$

where $F_{x(y)}$ is the force of X- or Y-axis required, $B_{vx(y)}$ is the friction coefficient of X- or Y-axis, f_l is the total load force impressed on the moving platform.

5.2.2 The Step Voltage method

This is a simple and easy-to-achieve method to obtain the magnetic characteristics of a SRM. It is achieved by applying a step voltage across the mover winding and simultaneously recording the current and voltage transients. Flux-linkage at a certain position can be evaluated offline accordingly [48].

Rearranging Equ.5.4, the flux-linkage can be expressed as,

$$\lambda_{kx(y)} = \int_{t_0}^{t_1} (V_{kx(y)} - R_{kx(y)} \cdot i_{kx(y)}) \cdot dt \quad (5.6)$$

After the phase winding is impressed with a DC voltage, the current increases. By recording the transient waveforms of terminal voltage and winding current, the flux-linkage can be derived through offline integration by using Equ.5.6.

In this method, first a step voltage with certain amount of holding time is applied across the mover winding, with the moving platform locked into a fixed position. Then the entire experiment is repeated with the moving platform fixed to a set of spaced positions, ranging from fully aligned and un-aligned positions within one pole-pitch.

This method is one of the most favorable for SR motor researchers with the following

advantages [48],

- i) Simplified procedure with the use of less number of components, equipment and instruments
- ii) Cost effective excitation source without the requirement of large power rating equipment
- iii) Simplified data processing
- iv) Flux-linkage versus different current levels can be evaluated without repetitions and no extra coils for sensing are required.

However, the flux-linkage obtained from this method contains self, mutual and leakage flux-linkage together. As described in Chapter 4, mutual inductance between any two movers of the PSRM is very small. However, this method is still preferred if leakage flux is also small for the PSRM.

5.2.3 The AC excitation method

The AC excitation method is based on the digital integration of the electromotive force induced by flux variations through a search coil mounted on stator poles [49]. From the general governing equations of SR motors in Equ.5.1, the transient or steady-state behavior can be determined as long as the flux-linkage function and winding resistance are both known. When a changing flux passes a search coil with N turns, an EMF, $e_{sr}(t)$ will be induced and flux can be obtained from the Faraday's Law,

$$\varphi(t) = -\frac{1}{N} \int e_{sr}(t) dt \quad (5.7)$$

Since flux calculation is a digital integration process, a slight DC offset will produce a

significant shift in the integrated value of flux. To eliminate this error, a compensation value δ_{esr} is added to the integration process as,

$$\delta_{esr} = \frac{\int_0^T e_{sr}(t) - e_{sr}(0)}{N_{sa}} \quad (5.8)$$

where $e_{sr}(0)$ is the initial voltage across the search coil and N_{sa} is the number of samples during one period T of the input AC current. Since the input current and voltage are pure AC waveforms across the excitation coil, the flux output after integration is assumed to be symmetrical with zero mean values, i.e. the maximum and minimum values of flux signals should be the same. Thus the initial flux $\varphi(0)$ can be obtained as,

$$\varphi(0) = \frac{\varphi(2) - \varphi(1)}{2} \quad (5.9)$$

Combining Equ.5.8, flux can be rearranged as [50],

$$\varphi(t) = -\frac{1}{N_s} \int_0^T (e_{sr}(t) + \delta_{esr}) dt + \varphi(0) \quad (5.10)$$

By joining the vertices of the first quadrant produced by various current levels, the flux-linkage profile can be constructed [51]. Furthermore, it is verified that flux-linkage results do not change for a specified maximum value of the excitation current in a wide range of excitation frequency values [49]. It can be expected that as the operating frequency increases, there is a reduction in flux-linkage values. This is mainly due to the demagnetization effect from eddy currents. However, eddy currents are negligible for a laminated motor structure. As a result, the reduction in flux-linkage value in change of frequency can be neglected. Moreover, even though the winding excitation current is not purely sinusoidal, the measurement method can still be considered valid [52].

This arrangement can determine the leakage flux-linkage as well. Leakage flux-linkage

can be regarded as any flux-linkage which does not link through the entire magnetic circuit.

Such flux deteriorates the electrical performance and increases the EMI.

5.2.4 Comparisons of DC and AC methods of flux-linkage measurement

Both of the two methods mentioned above are applicable to the measurement of SR motors. The Step Voltage method is a straight-forward way for flux-linkage measurement while it requires proper choice of DC power supplies. Once the measurement is conducted, experiment of same repetitions for different positions is sufficient, since the voltage and current waveforms have transient states containing all necessary information at a specified position.

The AC excitation method is more suitable for characterizing the magnetic properties of the PSRM, because it has the advantages of separation of mutual and leakage flux-linkage characteristics. The major disadvantage is the tedious repetition of measurement for different values of excitation currents for all concerned positions. Altogether the number of repetitions is equal to the number of voltage levels concerned multiplied by the number of concerned positions. Since this is a one-off measurement task, the benefit of measurement accuracy outweighs the inconveniences from the repetitive measurements.

5.3 Experiment results

The experiment results from the Step Voltage method and AC excitation method are discussed in Section 5.3.1 and 5.3.2, respectively.

5.3.1 The Step Voltage method

In this experiment, a DC voltage source is supplied to the coil winding under a set of lead-acid batteries. This battery power source can eliminate current ripples due to RLC oscillations [48]. Instead of a classical mechanical switch which would introduce unnecessary mechanical bouncing and voltage disturbances, a fast response solid-state relay is employed, as shown in Fig.5.2. This can offer fast switching response, vibration-free voltage transients and proper isolation.

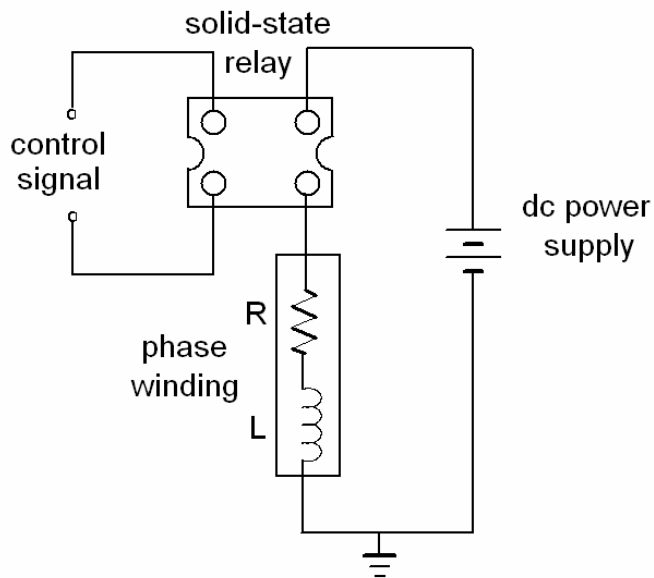
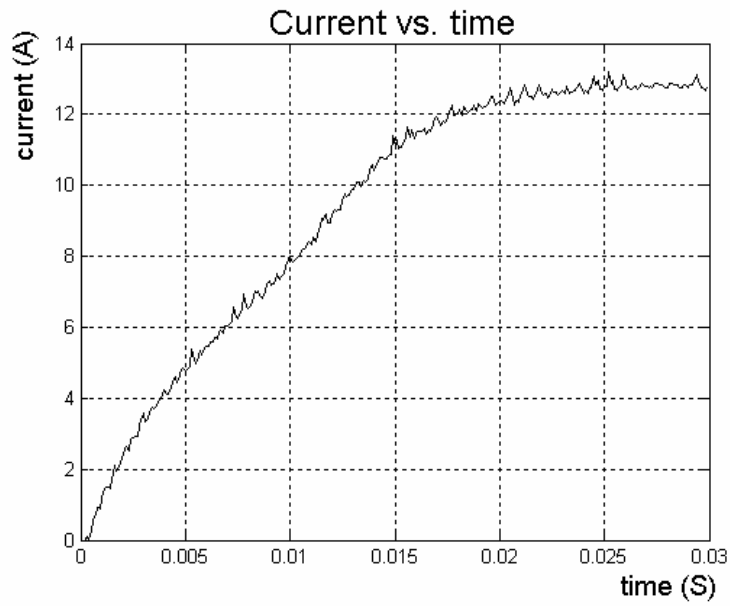
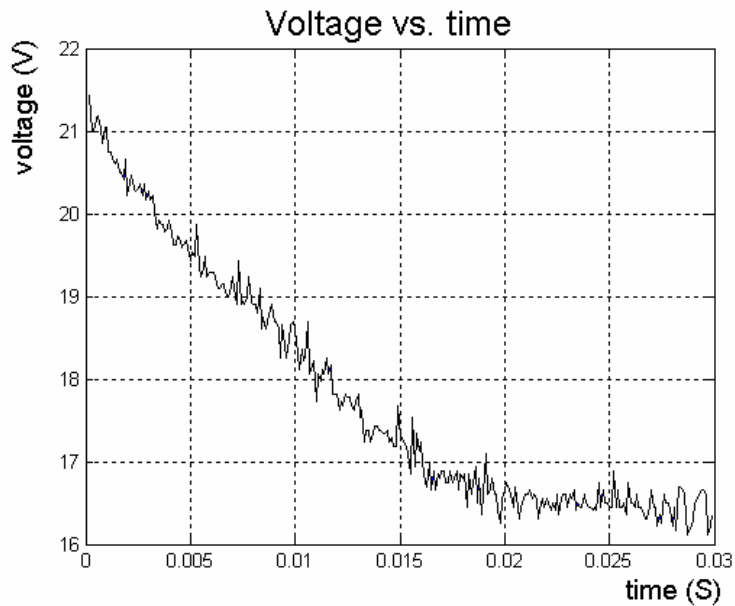


Fig.5.2 Experiment setup for Step Voltage measurement

Data is then collected from the fully aligned position to fully un-aligned position within half pole-pitch (6 mm). Fig.5.3 demonstrates the current rise and voltage drop waveforms at the aligned position.



(a)



(b)

Fig.5.3 Current and voltage waveform from the Step Voltage method at the aligned position (a) current rise (b) voltage drop

Due to the voltage limit of the batteries, the maximum value of current reaches 12A, however, it is clear that the slope gradually rises around 11A and the motor enters into saturated region as shown in Fig.5.4.

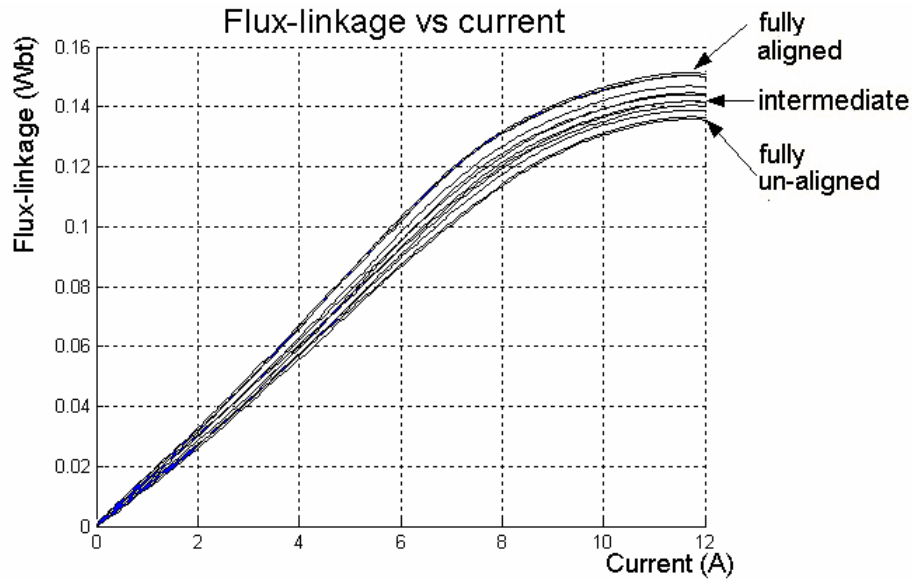


Fig.5.4 Flux-linkage waveform

From the flux-linkage profile of the planar motor, it can be concluded that the parameter of change of inductance is small. For the same force output, the planar motor should be excited with more current. Therefore force-to-weight ratio and the efficiency of this motor is low. Since the motor is exclusively designed for high-precision applications, the low force output will not affect the whole motor performance.

5.3.2 The AC excitation method

Since the excitation of current starts from the initial state and suspends when the motor is fully energized in the Step Voltage method, it can only simulate part of the real operating condition of the motor, i.e. from zero to full magnetization. Thus it is not able to depict motor state from demagnetization to magnetization.

Since any phase between each other in the PSRM is magnetically decoupled and all have the same electrical and magnetic characteristics, only one mover with a mounted search coil is sufficient to attain flux-linkage characteristics. In this experiment, the

moving platform should be tightly locked at particular positions and the excitation winding is supplied by a sinusoidal current [49].

As mentioned before, the experiment requires the use of search coils. The search coils with different mover locations have been installed before the assembly of the PSRM. Fig.5.5 shows their locations.

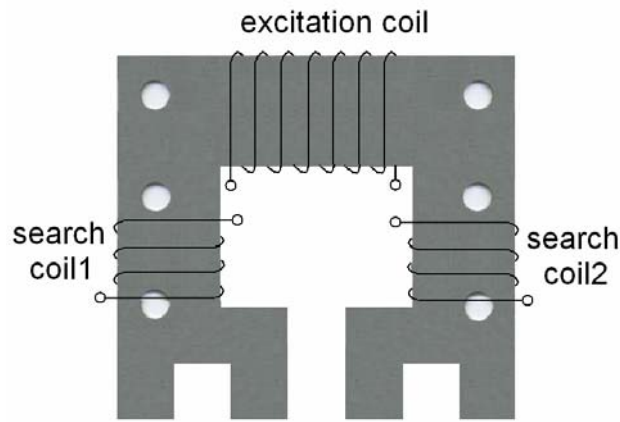


Fig.5.5 Search coil locations

As shown in Fig.5.6, the whole experiment setup includes an isolated auto-transformer with an adjustable voltage levels. The excitation coil is energized with bi-directional voltage signals. The induced voltage waveforms from the search coil(s) and the current from the main coil are measured and recorded. Flux-linkage can be calculated either online or offline by digital integration.

Hysteresis loops of one phase at three distinct positions are given in Fig.5.7. It can be clearly seen that flux-linkage does not differ much from fully aligned to fully un-aligned positions. The amount of difference reflects output force level and motor efficiency [8]. Unlike traditional RSRMs, which often own a significant change of flux-linkage value from the two positions [25], the PSRM is not suitable for applications that require large force

output due to relatively large air gap between the moving platform and stator and low change rate of inductance [25].

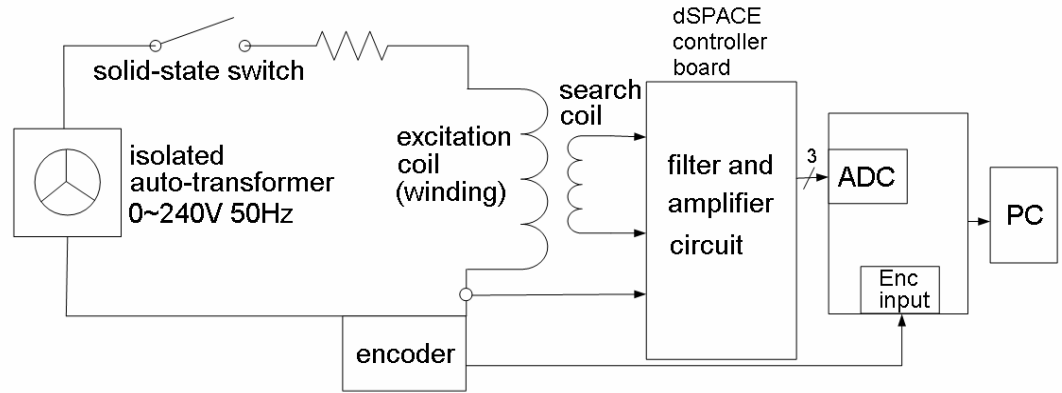


Fig.5.6 Experiment setup for AC excitation flux-linkage method

Due to the relatively large air gap, the motor enters saturated region at higher current levels. This means that efficiency is relatively low compared to RSRMs.

Hysteresis loops are also derived from the experiment with respect to different current levels. By joining the vertex of each loop, the “normal magnetization curve” can be obtained as shown in Fig.5.8.

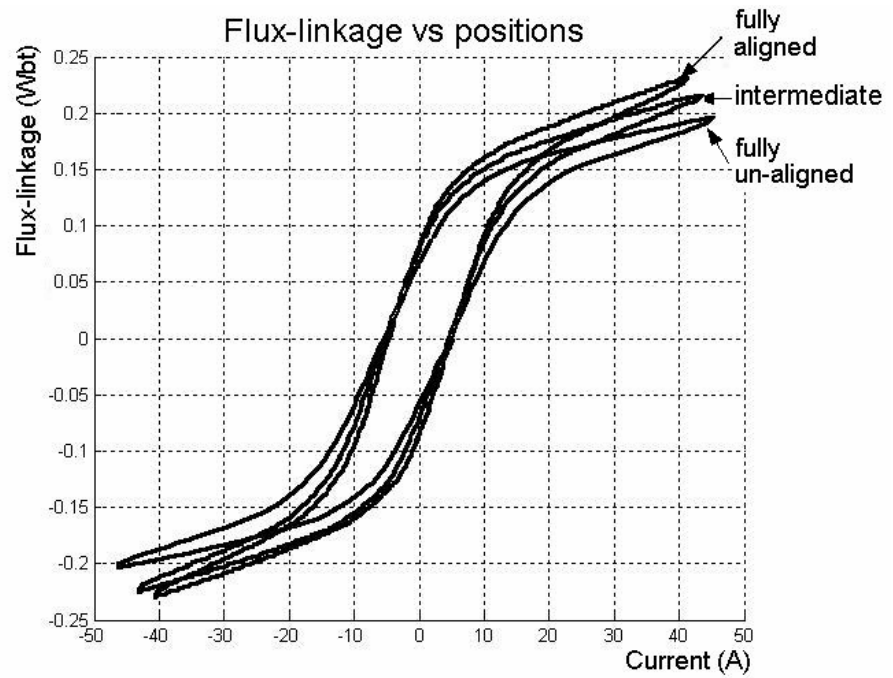


Fig.5.7 Hysteresis loops of the PSRM for one phase

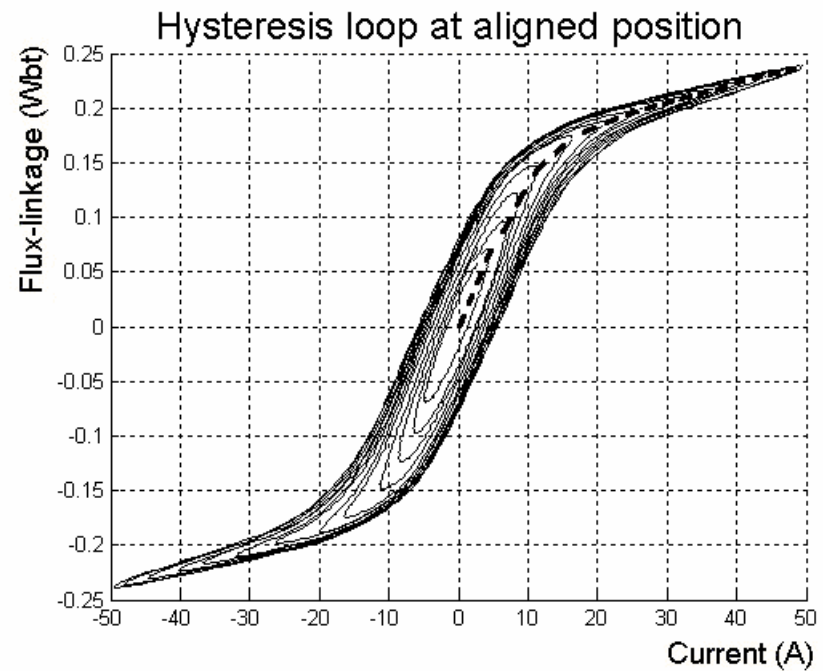


Fig.5.8 Flux-linkage at different current levels

5.4 Leakage flux-linkage

The possible leakage flux path is shown in Fig.5.9. With the search coils installed in Fig.5.5, leakage flux-linkage can be determined as the difference between the flux-linkage that flows through the legs of the mover supposing it flows clockwise.

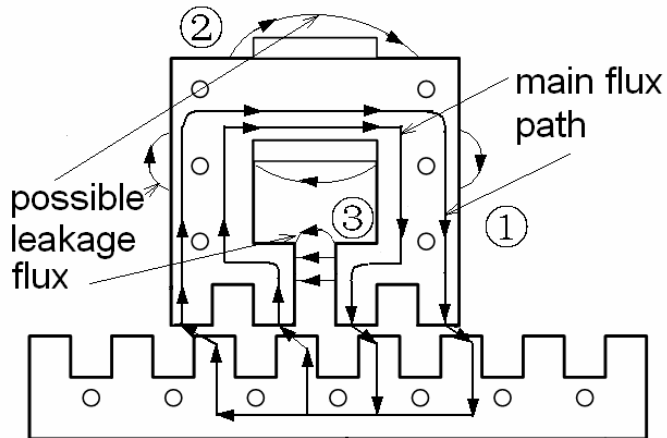


Fig.5.9 Possible flux paths

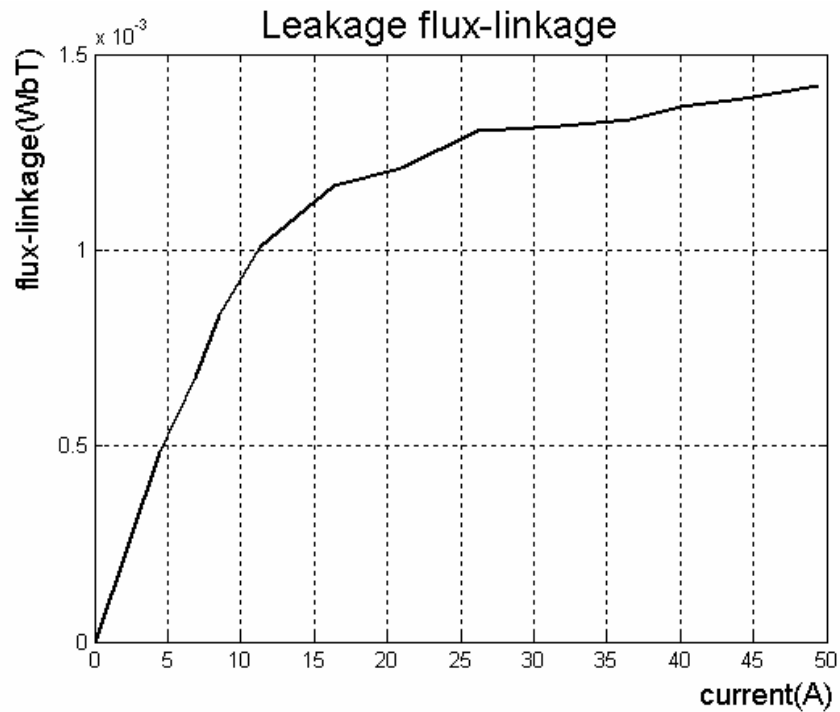


Fig.5.10 Leakage flux-linkage for the un-aligned position

Leakage flux-linkage can be easily determined from the difference of two search coils

mounted on the two legs of the U-shaped laminated sheet, as shown in Fig.5.5. Values are calculated and plotted according to different current levels for the un-aligned position. From Fig.5.10, the leakage flux-linkage is a two dimensional function with respect to both current and motor positions and takes only 0.6% of the total flux. Since the leakage flux-linkage is most predominant for the un-aligned situation [25], from the measurement results, leakage flux-linkage can be regarded as negligible.

Since the Step Voltage method only depicts the flux-linkage in the first quadrant and it requires decent DC power supplies for the measurement, the AC excitation method is more practical. The results from the AC excitation method are applied for modeling and control purposes.

5.5 Modeling of the planar switched reluctance motor

Modeling of flux-linkage characteristics plays an important role at the first stage for the control of SRMs. The main objective of flux-linkage modeling for the PSRM is to construct a mathematical model for simulation and controller design purposes. Unlike analytical and finite element approaches, modeling is based on the experiment data from magnetic characteristics.

The main goal of modeling is to provide a fairly good accuracy over the whole operating range of the machine but at the same time, issues such as memory occupation and calculation speed should also be considered. Therefore the choice of modeling techniques is a trade-off between precision and computation complexity.

Modeling of flux-linkage characteristics for SRMs is more complicated than that of DC

or AC machines, since the SR motor often operates under saturated region which typically includes the characteristics on i) the nonlinear B-H characteristics of the magnetic materials, ii) the dependence of flux-linkage on both current levels and positions and iii) the spatial effect such as local and bulk saturations [25].

A precise or a quasi-precise model for a SR motor, therefore, should take into account of i) the magnetic material's nonlinearity, ii) the saturation effect at different positions and iii) the mutual coupling effects.

SRMs are commonly designed as magnetically decoupled between any of the phases for single-phase excitation operation [8]. When multiple phases are excited at the same time, flux from different phase may share the same path, and flux from different phases may strengthen or counteract with each other. Therefore the behavior of the motor becomes more complex. As discussed before, this is not the case for the PSRM due to its magnetically decoupled structure of each mover.

5.6 Review of flux-linkage modeling methods

Several flux-linkage modeling techniques for SR machines have been proposed, such as piecewise approximation [53], parabolic approximation [54], or cubic-spline functions [55]. Some even directly incorporate a large scale look-up table and stores the entire flux-linkage data into the model [56]. Considering all the methods from a mathematical view, they can be classified as either an interpolation representation or a close-form function.

5.6.1 The look-up table method.

This method directly makes use of experiment data of flux-linkage vs. current levels and positions without introducing any data interpolation techniques or mathematical expressions [56]. The more the data, the more accurate the model will be. However this approach is slow and requires large memory storage and often introduces a heavy computation load. Furthermore, data falling outside the table still rely on interpolation techniques.

5.6.2. Piecewise linear approximation

Approximation with linear polynomials is the simplest approach for the modeling of SRMs [53]. Instead of modeling the flux-linkage directly from a close-form function, it divides the flux-current relationship into several sections with a few different linear polynomials. Generally the approximation is classified into linear, saturated and highly saturated regions, respectively.

This is not an accurate method because the motor does not behave linearly as it enters the saturation region. However it is simple for implementation and useful for rough prediction of SRM characteristics..

5.6.3 Parabolic approximation

Similar to linear polynomials, it is still a piecewise technique but with parabolic interpolation [57]. Generally the complete flux-linkage curve is divided into three sections as shown in Fig.5.11. Curve ① is used to approximate the magnetization curve for the un-aligned position and other two curves ② and ③ for the aligned position. Curve ①, ②,

③ can be respectively represented as [57],

$$\begin{cases} \lambda_u(i) = L_u \cdot i & \text{un-aligned} \\ \lambda_a(i) = L_a \cdot i & \text{aligned linear region} \\ \lambda_a(i) = \lambda_{so} + \sqrt{4a(i - i_{so})} & \text{aligned saturated region} \end{cases} \quad (5.11)$$

where L_u and L_a represent equivalent inductance in the un-aligned and aligned position.

Flux-linkage in the aligned region is divided into two parts according to current level i .

λ_u, λ_a are flux-linkage at the un-aligned and aligned position. λ_{so} and i_{so} are constants to be determined. This method requires two points in curve to be known to decide the values of λ_{so} and i_{so} .

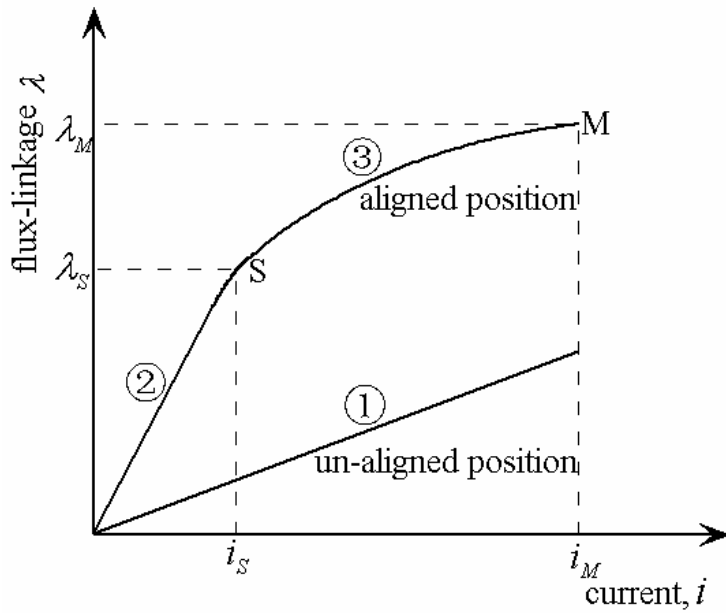


Fig.5.11 Approximation of flux-linkage vs. current curves

Generally the points of entering and leaving the saturation region are selected. According to article [57], the choice of point S and M significantly affects the accuracy of the modeling result. One limitation from this method is that it takes the assumption that the mover and stator pole have the same length. Another limitation is that it also assumes the saturation current to be constant at all positions which is often not the case in real SRM

operations.

5.6.4 Arc-tangent representation

This new proposed method is proposed in [58] and it is a piecewise method with interpolation skills. Three curves where the motor resides in the fully aligned, midway and fully un-aligned positions are taken into consideration to represent the magnetization characteristics. The curve for the un-aligned position is described the same as Equ.5.11 as a straight line.

Flux-linkage in other two positions (fully-aligned and midway) are described as,

$$\lambda_a = \frac{\arctan(a_1 \cdot i)}{a_2} \quad (5.12)$$

$$\lambda_m = \frac{\arctan(m_1 \cdot i)}{m_2} \quad (5.13)$$

where a_1 and a_2 are constants to be determined. a_1 can be obtained by curve-fitting as,

$$\frac{\lambda_{ma}}{\lambda_{sa}} = \frac{\arctan(a_1 \cdot i_m)}{\arctan(a_1 \cdot i_s)} \quad (5.14)$$

and a_2 can be determined as follows [58],

$$a_2 = \frac{\lambda_{sa}}{\arctan(a_1 \cdot i_s)} \quad (5.15)$$

Before the constants are solved, the point of saturated threshold (i_s, λ_{sa}) and one point with current i_m falling between the values of the triple to quadruple of i_s should be selected. The constants for the midway flux-linkage can be determined in the same way.

Compared with parabolic approximation, this method has no limitations of the same pole length from the mover and stator. However it needs a more complex curve-fitting

technique to find a_1 and a_2 , therefore it requires more memory and computation time.

5.6.5 Cubic-spline

Cubic-spline function is a precise modeling technique especially for nonlinear characteristics of electric machines [59]. High accuracy can be achieved with a two dimensional curve-fitting [55] for a wide range of SR motors.

In article [55], first the relationship of flux-linkage between current and position is considered in 3D format. Then flux-linkage function is divided into numerous small rectangular regions represented by nodes. For each rectangle, it can be represented with the following equation [55],

$$\lambda(x(y), i) = [g_{k1}(x(y)), g_{k2}(x(y)), g_{k3}(x(y)), g_{k4}(x(y))] A \begin{bmatrix} g_{j1}(i) \\ g_{j2}(i) \\ g_{j3}(i) \\ g_{j4}(i) \end{bmatrix} \quad (5.16)$$

where $x(y)$ and i are position at X- or Y-axis and current levels which are bounded by the nodes of corresponding rectangles and $x(y)_k \leq x(y) \leq x(y)_{k+1}$, $i_j \leq i \leq i_{j+1}$.

Besides, g_{km} and g_{jn} have to satisfy the equations below ($m, n = 1, 2, 3, 4$),

$$\begin{cases} g_{k1}(i) = 1 \\ g_{k2}(i) = x(y) - x(y)_k \\ g_{k3}(i) = (x(y) - x(y)_k)^2 \\ g_{k4}(i) = (x(y) - x(y)_k)^3 \end{cases}, \begin{cases} g_{j1}(i) = 1 \\ g_{j2}(i) = i - i_j \\ g_{j3}(i) = (i - i_j)^2 \\ g_{j4}(i) = (i - i_j)^3 \end{cases} \quad (5.17)$$

and A is a 4×4 matrix,

$$A = \begin{bmatrix} a_{kj11} & a_{kj12} & a_{kj13} & a_{kj14} \\ a_{kj21} & a_{kj22} & a_{kj23} & a_{kj24} \\ a_{kj31} & a_{kj32} & a_{kj33} & a_{kj34} \\ a_{kj41} & a_{kj42} & a_{kj43} & a_{kj44} \end{bmatrix} \quad (5.18)$$

The flux-linkage for any one of the rectangle can be known as long as matrix A is found.

Altogether there are $16 \times (n-1) \times (m-1)$ coefficients for the whole rectangular region. Hence the computation is complex and needs high calculation power. Furthermore the intermediate data should be stored all the time during calculation which requires lots of memory space. Therefore it is not a suitable choice for SR motors with real-time simulation and implementation purposes.

5.6.6 Exponential description

The modeling techniques discussed above all involve interpolation procedures, in which the magnetization curve should be split into several regions and interpolation is performed for each region respectively. The exponential description function is a model tailored for SR motors. First of all it does not split the magnetization curve into different regions. Unlike other methods, it obtains a closed form of flux-linkage function and avoids continuity problem.

Self flux-linkage is expressed as a flux model with a constant multiplied by an exponential function [60], then a least square curve-fitting method is applied to the flux-current diagram so that the nonlinear exponential function can be represented by the following equation,

$$\lambda_s(x(y), i) = \lambda_{sat} (1 - e^{i \cdot f(x(y))}) \quad (5.19)$$

where λ_{sat} is saturation flux-linkage value. The function $f(x(y))$ is a fifth Fourier series expansion as,

$$f(x(y)) = a + b \cos(x(y)) + c \cos 2(x(y)) + d \sin(x(y)) + e \sin 2(x(y)) \quad (5.20)$$

5.7 Modeling of the planar switched reluctance motor

Fig.5.12 shows the 3D profile of the flux-linkage modeled with exponential description function for one mover. The modeling parameters are tabulated in Table 5.1.

Flux-linkage from exponential function

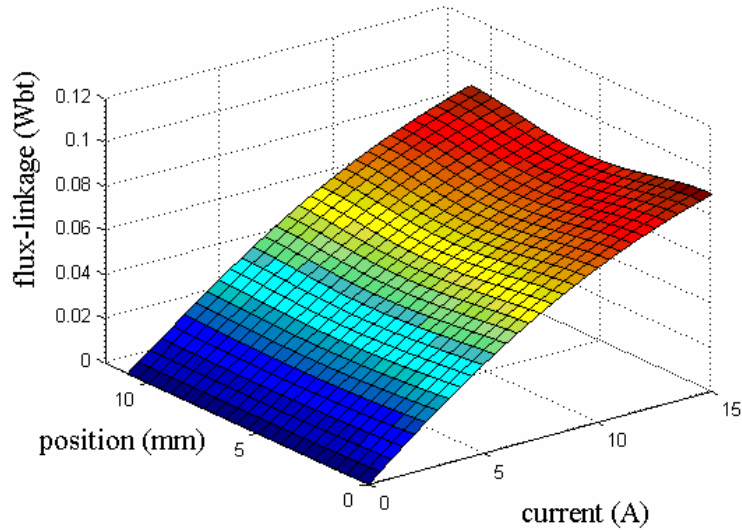


Fig.5.12 Flux-linkage modeling

The result of flux-linkage measurement is compared with that of the modeling. As shown in Fig.5.13, the maximum absolute error falls between 2% of the measured value of flux-linkage.

Parameters	Values
a	5.83
b	-14.29
c	1.87
d	-9.34
e	3.56
λ_{sat}	0.056

Table 5.1 Modeling parameters of the PSRM

Error from exponential curve-fitting

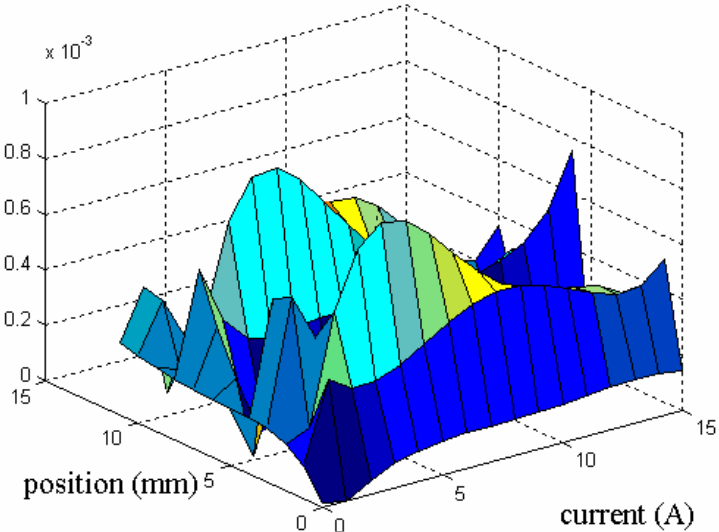


Fig.5.13 Error from exponential curve-fitting

5.8 Dynamic model of the planar switched reluctance motor

The mechanical equations that govern the entire system model can be described in state-space form as the following,

$$\frac{ds_{x(y)}}{dt} = v_{x(y)} \quad (5.21)$$

$$\frac{dv_{x(y)}}{dt} = (F_{x(y)} - B_{x(y)}v_{x(y)} - f_{lx(y)}) / M_{x(y)} \quad (5.22)$$

Rearranging voltage balance equation in state-space and neglecting mutual and leakage flux-linkage,

$$\frac{di}{dt} = \frac{U - Ri - \frac{\partial \lambda_s}{\partial s_{x(y)}} \cdot \frac{ds_{x(y)}}{dt}}{\frac{\partial \lambda_s}{\partial i}} \quad (5.23)$$

With the exponential representation of flux-linkage as discussed above,

$$\frac{\partial \lambda_s}{\partial s_{x(y)}} = \lambda_{sat} \cdot i \cdot e^{-i \cdot f(s)} \frac{\partial f(s)}{\partial s} \quad (5.24)$$

$$\frac{\partial \lambda_s}{\partial i} = \lambda_{sat} \cdot e^{-i \cdot f(s)} f(s) \quad (5.25)$$

In this model, nonlinear friction, hysteresis and eddy current effect are not included.

5.9 Summary

In this chapter, characterization of the PSRM is achieved with two different flux-linkage measurement techniques. Other magnetic characteristics such as hysteresis and leakage flux-linkage are also obtained. The measured flux-linkage characteristic of the PSRM is modeled with a closed form exponential function. Results show that the measurement results match the modeling closely. It can be concluded that with an accurate dynamic model developed, the PSRM is ready for controller design and simulation processes.

Chapter 6

Trajectory control of the planar switched reluctance motor

In this chapter, a suitable current control scheme is proposed before applying the position control algorithms. Then, review of different current excitation schemes is carried out and the multi-phase excitation scheme is selected for a smooth motor operation. Next, a PD controller is implemented to test the motor performance. Finally, to improve the motor performance under the environment of increased frequency, an improved dual-loop controller is proposed and implemented.

6.1 The current controller

Section 6.1.1 reviews the commonly used current control techniques. Design and analysis of a proper current controller for the PSRM is described in Section 6.1.2. Test verification of the current controller is provided in Section 6.1.3.

6.1.1 Introduction

Before the construction of the overall control scheme, a proper current regulator should be built to provide a satisfactory current response for the PSRM. Since the current regulator serves as the innermost loop within the entire control system, a poor current response will have a severe impact on the overall system performance. The designed current regulator

serves as a basis for future implementation of outer loop control schemes that are suitable for either velocity or trajectory control strategies.

On the control of current, two types of current regulators are commonly used. They are hysteresis regulator and Proportional Integral and Differential (PID) regulator with Pulse-Width Modulation (PWM), as shown in Fig.6.1 (a) and (b) respectively.

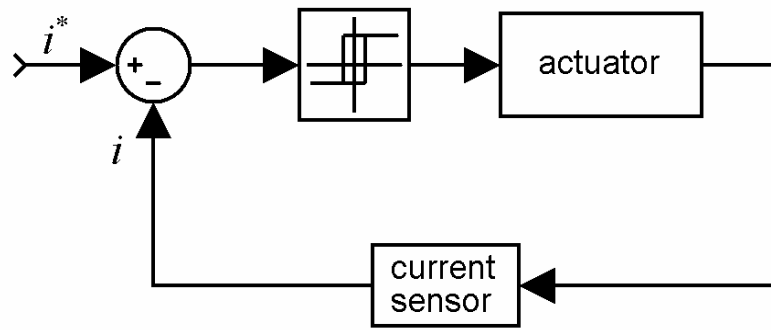


Fig.6.1 (a) A typical hysteresis current regulator

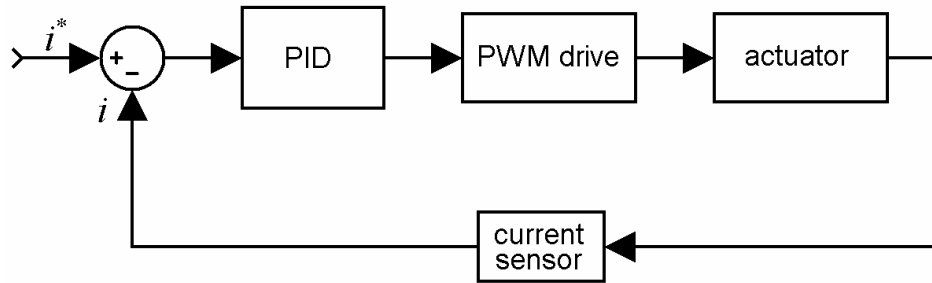


Fig.6.1 (b) A typical PWM current regulator

The hysteresis regulator has an upper (i_{up}) and lower (i_{low}) band of current limit. When the error from the reference(i) and actual signal(i^*) is positive, the regulator switches on and current rises accordingly; after the error changes its symbol, the switch turns off and allows current to fall. Therefore by turning on and off the switch with respect to the error, the actual current waveform behaves a “saw tooth” within the upper and lower band limit as shown in Fig.6.2. The hysteresis regulation is classified as a type of “Bang-Bang” control

strategy.

The switching frequency carries along one fundamental cycle with a fixed band. Hysteresis regulators are easy to implement and robust to load variations, which can be found vastly in applications of stepper current drives and power electronic circuits. However the working manner results in fast dynamics and large current ripples, especially at low current levels.

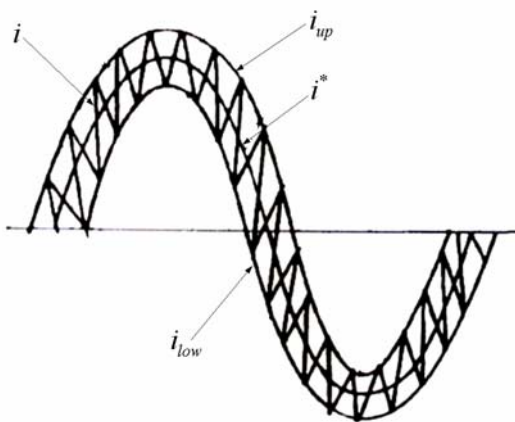


Fig.6.2 Current waveform in a typical hysteresis controller

Combined with PID control algorithm, the switching frequency of the PWM drive is high and has less current ripples [57]. It is widely used in industrial applications as current amplifiers for PM and SR motors since it provides a better solution for controller design. It is also a simple and effective method for hardware implementation.

6.1.2 Current controller for the planar switched reluctance motor

Considering the mechanical resonance of the mover, the operating frequency is within the order of 10 Hz. Therefore a sampling rate in the range of KHz is enough to correct current errors in time. The fast inner loop controller is employed to trace the currents through the motor windings, while the slower outer loop trajectory controller is used to track the

reference position profiles. Once the inner current controller is fully set up, future research work will concentrate on the design of the outer control loop.

For the current controller for either axis, three asymmetric bridge PWM inverters are employed so that high dynamic response can be enjoyed independently in each motor phase [8]. Fig.6.3 shows the circuit of the inverter for one axis.

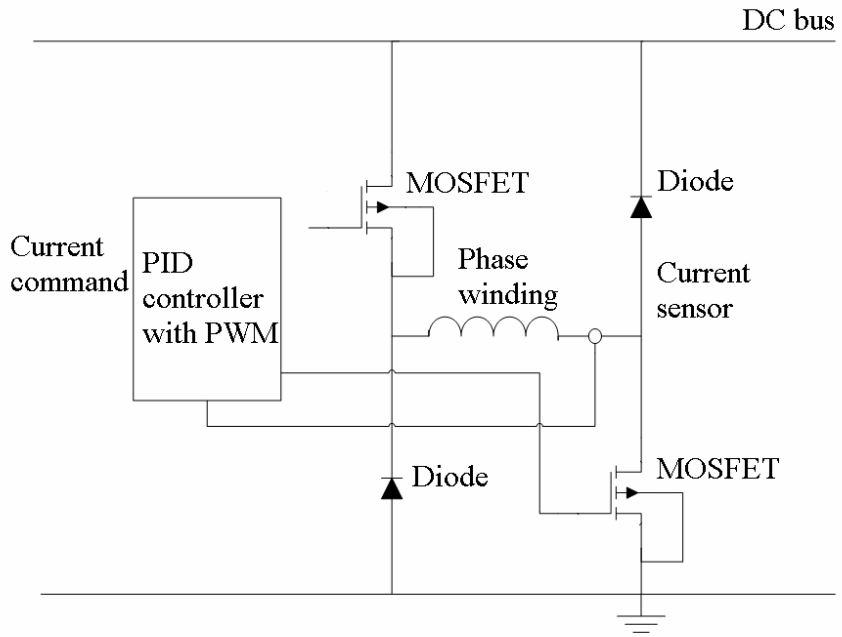


Fig.6.3 An asymmetric bridge PWM inverter

As the PSRM is a unipolar current driving motor, only two power switches (e.g. MOSFETs) are needed in any one single phase in the asymmetric inverter and two diodes are used as the current return path. At the side of pulse width modulation (PWM) drive, the relationship between output current and input voltage for any one phase is [62],

$$\dot{i}_k = -\frac{R}{L_k(x,i)} \cdot i_k - \frac{\partial L_k(x,i)}{\partial x} \cdot \dot{x} \cdot \frac{1}{L_k(x,i)} \cdot i_k + \frac{1}{L_k(x,i)} \cdot V_k \quad (6.1)$$

where i_k is output current, V_k is input voltage. R is the winding resistance and L_k is phase inductance. At the side of the PWM drive, the relationship between output and input is,

$$\dot{i}_k = -\frac{R}{L_k(x)} \cdot i_k + \frac{C}{L_k(x)} \cdot U_k \quad (6.2)$$

where C is the converter gain and U_k is the controller input.

From Fig.5.8, it can be seen that the gradient of flux-linkage remains relatively constant from 0 to 12A, before it enters the saturation region. Even in the saturation region the gradient of flux-linkage gently declines in a uniform fashion. Through this inspection, a simple PI current controller is sufficient [25]. The reduction in the flux-linkage gradient is merely treated as a disturbance and it can be regulated quite easily from the controller. The block diagram of the current controller is shown in Fig.6.4 for one phase. With the help of the PWM modulator, the system plant can be represented by a first order system as,

$$H(s) = \frac{K_c}{L_k s + R} \quad (6.3)$$

where K_c is the converter gain. The Proportional and Integral gain K_p and K_i are coefficients to be considered.

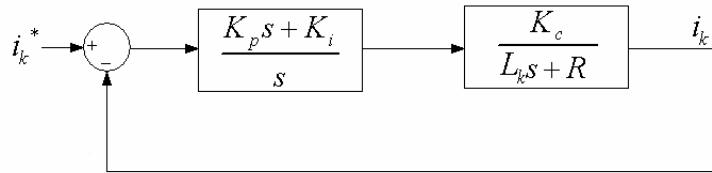


Fig.6.4 Block diagram for current control loop

The transfer function governing the controller is as follows,

$$G(s) = \frac{i_k(s)}{i_k^*(s)} = \frac{K_c(K_p s + K_i)}{L_k s^2 + (R + K_c K_p)s + K_c K_i} \quad (6.4)$$

Noticing that $K_c K_p \ll R$, the transfer function can be further simplified as,

$$G(s) = \frac{i_k(s)}{i_k^*(s)} = \frac{K_c(K_p s + K_i)}{L_k s^2 + (R + K_c K_p)s + K_c K_i} = \frac{\frac{K_c K_p}{L_k} s + \frac{K_c K_i}{L_k}}{s^2 + \frac{K_c K_p}{L_k} s + \frac{K_c K_i}{L_k}} \quad (6.5)$$

The coefficients K_p and K_i then can be determined from damping factor and natural frequency of a second order system,

$$K_p = \frac{2\zeta\omega_n L_k}{K_c} \quad (6.6)$$

$$K_i = \frac{\omega_n^2 L_k}{K_c} \quad (6.7)$$

By choosing a proper value of K_p and K_i , the error will diminish to zero within a relatively short time and an overshoot free response can be achieved [31].

6.1.3 Test verification

The current controller is implemented with the above control law and the current step response is shown for the aligned and un-aligned position in Fig.6.5 (a) and (b) respectively. The sampling rate of the current loop with 2 KHz is adequate for applications with a sampling frequency in the order of Hertz. Fig.6.5 (a) shows the current step response when the motor winding is in the aligned position where the phase inductance attains its maximum value. The output does not exhibit any overshoot when the proposed adaptive PI controller is used. The rise time is around 180 μ s which is equivalent to a 1.2 kHz bandwidth. Next the current response is measured and shown in Fig.6.5 (b) when the motor winding is at the un-aligned position where the phase inductance attains its minimum value. As the inductance variation is compensated by the adaptive tuning of the PI gains, the overshoot-free step response and the 180 μ s rise time are still maintained. The PI controller

employed in this current loop ensures a desirable tracking response, so that the perfect current tracking condition can be assumed in the outer loops with slow dynamics.

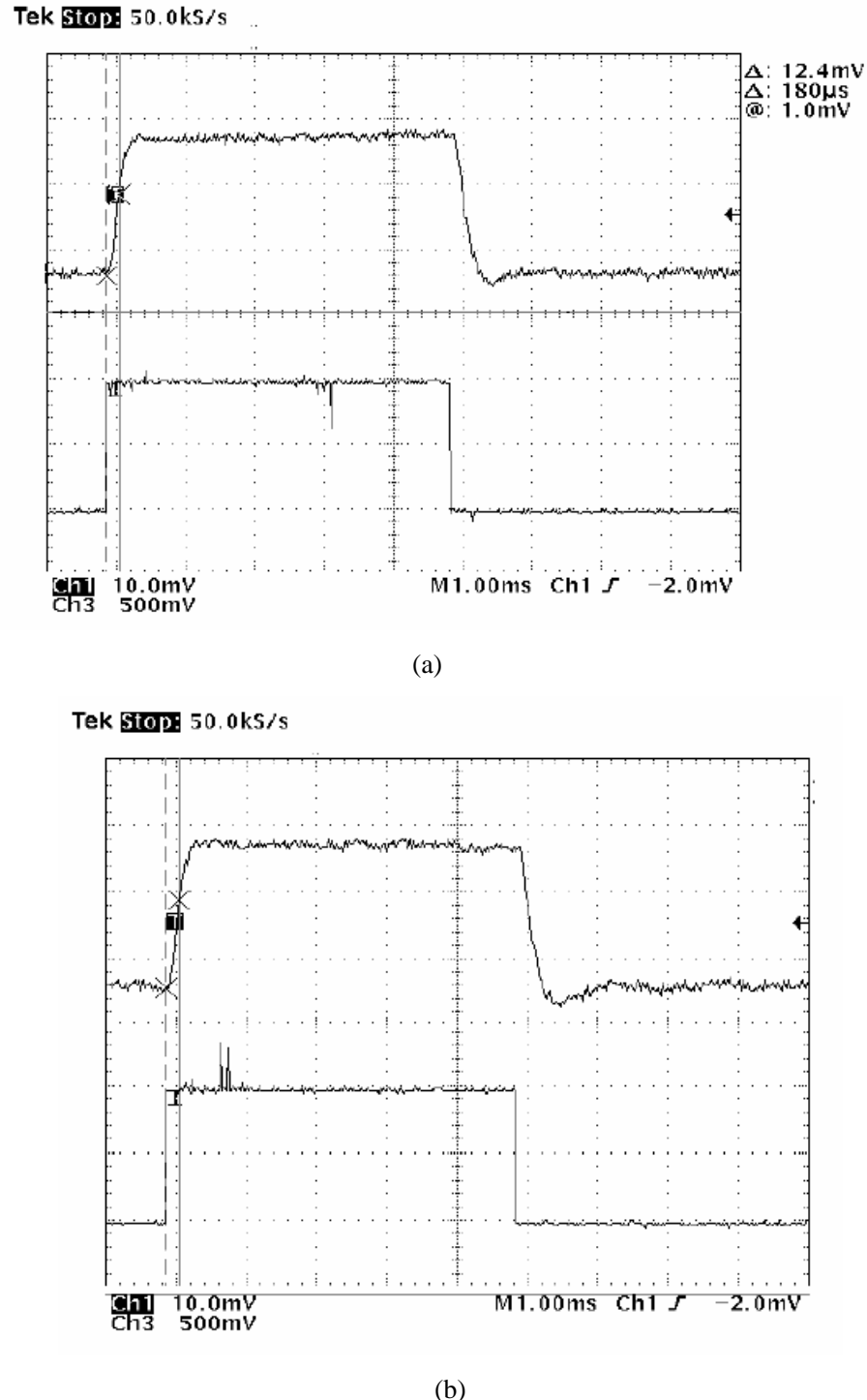


Fig.6.5 Current response of the motor's coil at (a) fully aligned position, and (b) fully un-aligned position.

6.2 Phase excitation schemes

In traditional torque/force control method for AC and DC motors, torque/force is proportional to excitation current or transformed current variables [25]. In the case of SR motors, torque/force is not only dependent on current levels but also on different positions. As shown in article [31] of measured force profile, output force of the PSRM is a complex three dimensional relationship with both current and position.

6.2.1 Single phase excitation

The single phase excitation scheme, by definition, describes that each phase of the three phases in a 6/4 SR machine is excited in a sequential manner as required by the force command. The commutation angle for a RSRM is often optimized by selecting an angle for a given torque that requires minimum current for a maximum possible motor efficiency. This typically belongs to torque/force control category and can be found in various RSRM applications [8, 25]. The characteristics of this excitation method for the PSRM can be summarized as below with the motor example as the PSRM.

For simplicity, suppose perfect flat topped current waveforms can be obtained from the current controller for each phase and the PSRM has an ideal inductance profile as shown in Fig.6.6. According to the force relationship in the unsaturated region,

$$F_{x(y)} = \frac{1}{2} \cdot \frac{dL_k}{dx(y)} \cdot i_k^2 \quad (6.8)$$

It can been seen that a positive force can be generated at rising slope of the inductance and a negative one in the falling region, regardless of current directions. In order to obtain positive force, phase A can be energized during 0 mm to 6 mm, phase B, 4 mm to 8 mm and

phase C 8 mm to 12 mm. Then with a flat topped current input for each phase, a uniform force profile can be derived.

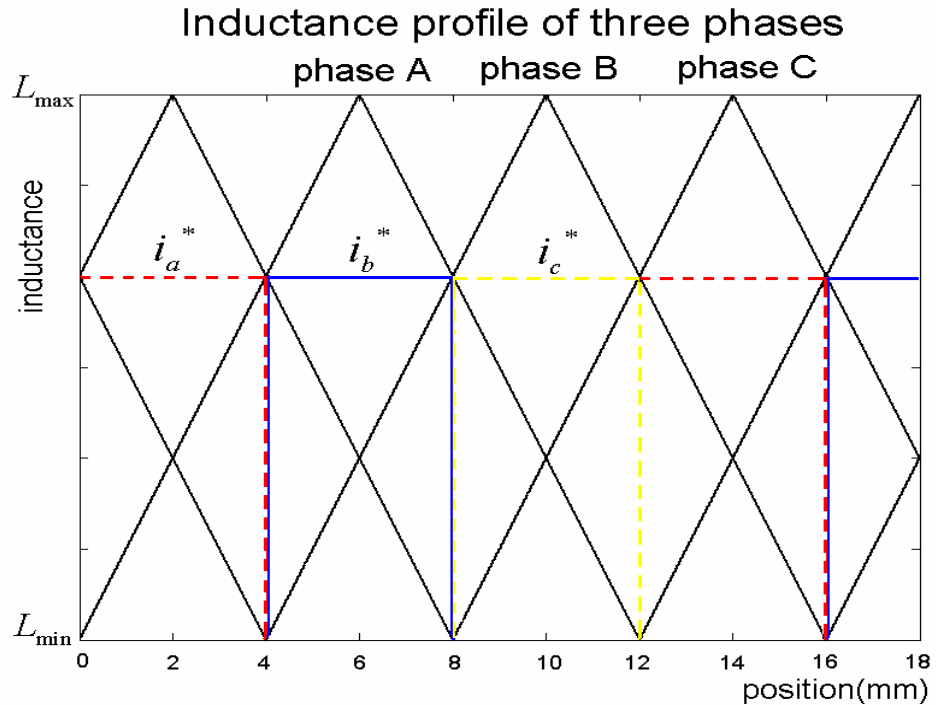


Fig.6.6 Ideal inductance profile

However, in real motor operation, perfect flat topped current waveforms can not be obtained from winding with inductances [8]. There should be a finite period for the current to rise and another one allowing the current to fall. A typical current waveform is shown below in Fig.6.7 (a). With the inductance profile shown in Fig.6.6, the instantaneous output force produced at a fixed speed can be derived as shown in Fig.6.7 (b).

As can been seen from the diagrams, force is bound to be produced in a pulsed manner, resulting in a possible increase in force ripples. Moreover, the motor will inevitably encounter force dips during switch between phases. Furthermore, in actual motor operation, there are many types of force ripples due to saturation and nonlinear force production when only one phase is conducted, which also adds to increased audible noise and stress on the

motor's mechanical structure [31]. It can also be observed that force ripples are inversely related to the smoothness of current transition between phases, and it is possible to minimize the ripples during these transitions by controlling currents in the overlapping phases [63].

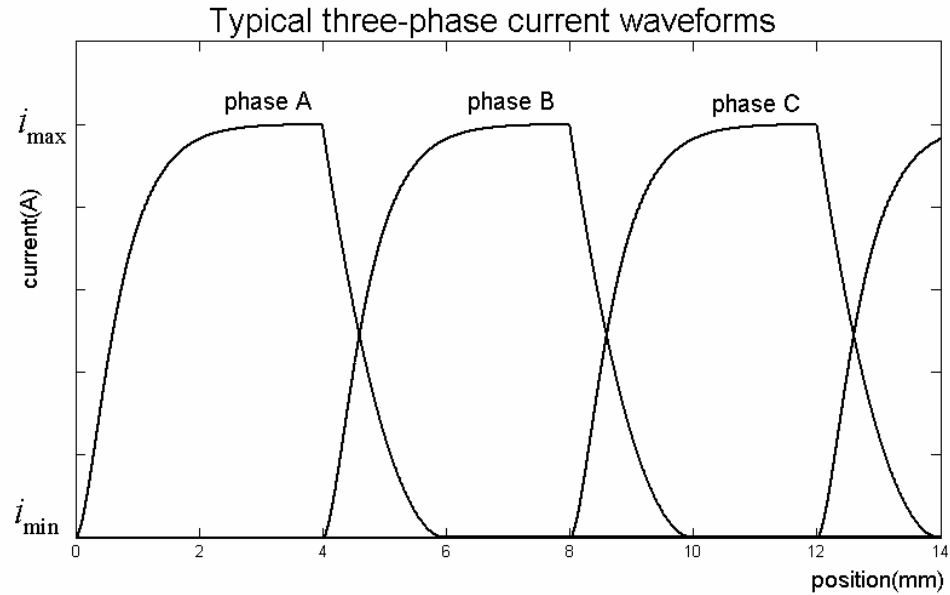


Fig.6.7 (a) Waveform of three phases

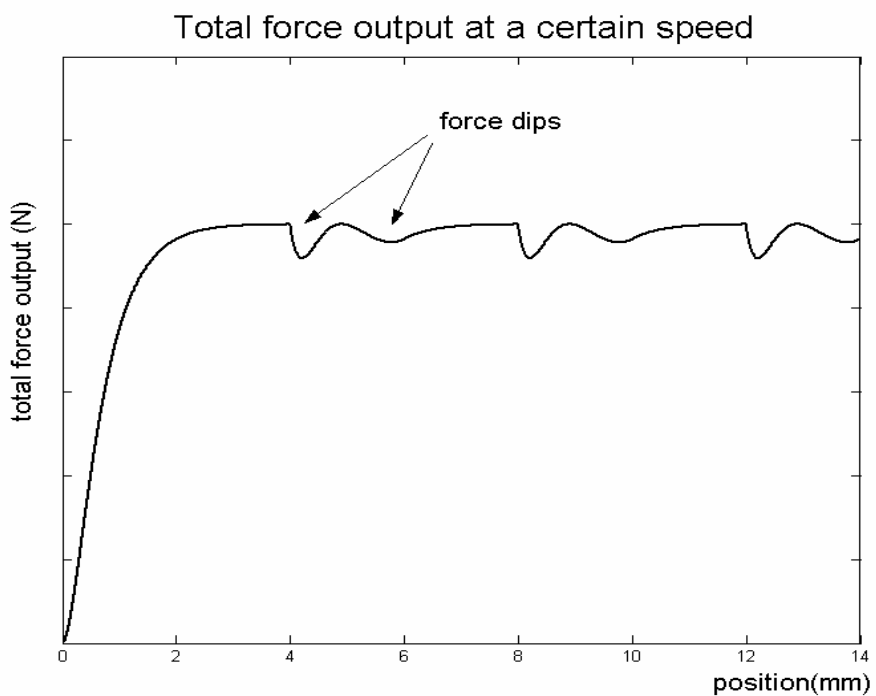


Fig.6.7 (b) Total force output at a certain speed from single phase excitation

6.2.2 Multi-phase excitation

The multi-phase excitation method describes that at a certain position, according to the force command (value and direction), the scheme decides which one or two phases should be turned on. The conduction angle/position for multi-phase excitation scheme depends on the inductance profile of a SRM.

Before determination of the force distribution algorithm, some constraints can be derived based on the observations of the inductance profile that i) the sum of the force from each phase equals to the force command and ii) both contribute to the force output with the same sign as required by the force command.

These rules can be summarized in equations as,

$$\begin{cases} f_1(x(y)) = g_1(x(y))f^*(x(y)) \\ f_2(x(y)) = g_2(x(y))f^*(x(y)) \end{cases} \quad (6.9)$$

where number 1 and 2 can be replaced by phase from A to C, with the constraints satisfying,

$$g_1(x(y)) + g_2(x(y)) \equiv 1$$

$$0 \leq g_1(x(y)) \leq 1, \quad g_1(on) = 1, \quad g_1(off) = 0 \quad \text{for } on \leq (x(y)) \leq off \quad (6.10)$$

$$0 \leq g_2(x(y)) \leq 1, \quad g_2(on) = 0, \quad g_2(off) = 1$$

Symbol *on* and *off* are the turn-on and turn-off positions (0, 2, ..., 12 mm) of the commutation region, respectively.

The determination of the force distribution algorithm can be based on many criteria such as [64], i) minimal integral from the square of the rate of change of current, ii) minimal rate of change of current, iii) minimal peak current and minimum stator losses.

6.2.3 The excitation scheme for the planar switched reluctance motor

For position control applications, the motor's operation should be focused on smooth tracking ability with gradual variations of phase currents, therefore a force distribution table (FDF) is proposed in [64] for the PSRM.

Observing the ideal inductance change profile in Fig.6.6 it is reasonable to divide one pole-pitch (12 mm) into six excitation regions and force components from each phase. Then the force for simultaneously conducted phases can be expressed as shown in Table 1 with reference position defined in Fig.6.8.

Position range (mm)	Positive force command ($f^* > 0$)	Negative force command ($f^* < 0$)
$0 < x(y) \leq 2$	$f_a = 0, f_b = f^*, f_c = 0$	$f_a = g_a f^*, f_b = 0, f_c = g_c f^*$
$2 < x(y) \leq 4$	$f_a = 0, f_b = g_b f^*, f_c = g_c f^*$	$f_a = f^*, f_b = 0, f_c = 0$
$4 < x(y) \leq 6$	$f_a = 0, f_b = 0, f_c = f^*$	$f_a = g_a f^*, f_b = g_b f^*, f_c = 0$
$6 < x(y) \leq 8$	$f_a = g_a f^*, f_b = 0, f_c = g_c f^*$	$f_a = 0, f_b = f^*, f_c = 0$
$8 < x(y) \leq 10$	$f_a = f^*, f_b = 0, f_c = 0$	$f_a = 0, f_b = g_b f^*, f_c = g_c f^*$
$10 < x(y) \leq 12$	$f_a = g_a f^*, f_b = g_b f^*, f_c = 0$	$f_a = 0, f_b = 0, f_c = f^*$

Note: Reference position (0 mm) is fully aligned position for phase A and right stands for the positive force command.

Table 6.1. The multi-phase excitation scheme.

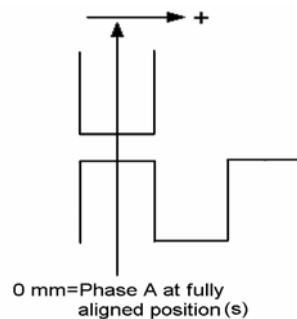


Fig.6.8 Reference position

Fig.6.9 shows the position control diagram with the force distribution function (FDF) for one axis of the PSRM. The position controller determines the force command from the position error. First the force command f^* from the position controller is divided in three parts— f_a^* , f_b^* and f_c^* , depending on the motor's current position. Then each phase calculates current values for corresponding force generation. The current controller outputs a current value according to the current command. Last output force is computed corresponding to position and current requirements for each phase and total force is summed up to drive the control object.

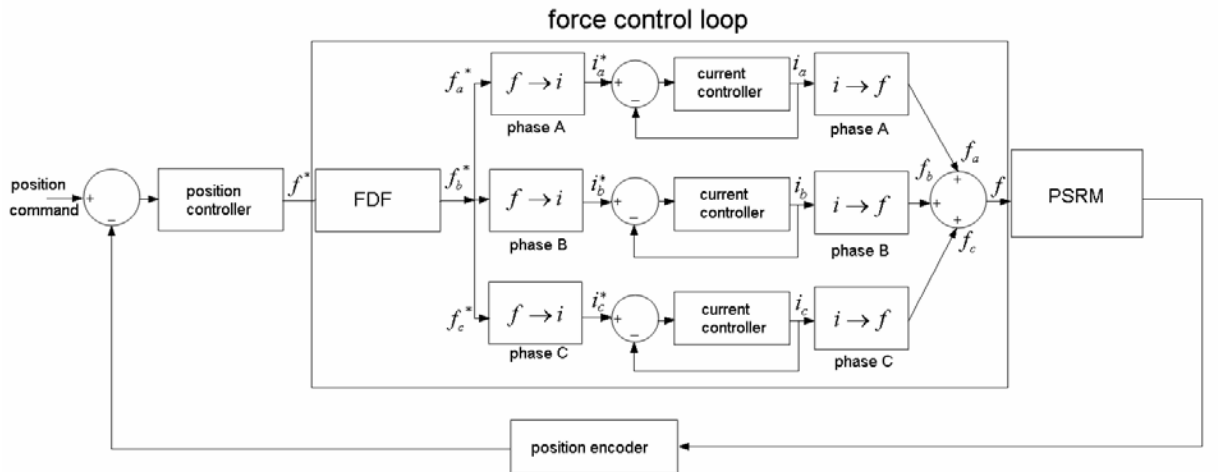


Fig.6.9 Position control block with multi-phase excitation for one axis

If the motor operates under linear region only, then the force control loop can be represented as,

$$f^* = \sum_{k=1,2,\dots,6} \frac{1}{2} \cdot g_k \cdot (i_k^*)^2 \cong \frac{1}{2} \sum_{k=1,2,\dots,6} g_k \cdot i_k^2 = f \quad (6.11)$$

where g_k stands for the change rate of inductance for any phase. As long as the actual phase current tracks the current command precisely, the required force can be obtained by controlling the current from each phase. With a current controller having a good dynamic

response, it can be assumed that,

$$i_k \approx i_k^* \quad (6.12)$$

Similar with DC or AC motors, the ultimate goal of torque/force control is to obtain a linear or quasi-linear model for simplification of control issues. In the case of SRMs, since force is a three dimensional relationship with both current and position, it is expected that by implementation of a proper multi-phase scheme together with the representation of the electromechanical property that describes the relationship of current and output force for each phase and its inverse function, a simplified control model can be achieved to compensate the nonlinearities of the PSRM.

6.3 Linearization of the planar switched reluctance motor

First, analysis of different linearization schemes is given in Section 6.3.1. Then, a linearization scheme toward smooth motor operation and easy implementation is selected for the PSRM as described in Section 6.3.2. Finally, experiment verification of the effectiveness of the linearization scheme is provided in Section 6.3.3.

6.3.1 Introduction

After a proper phase excitation scheme is determined, the representation of the relationship for the output force and input current and position is of high importance. In real operations, SR motors often enter the saturated region. To compensate the saturation nonlinearity, several ideas have been developed. These include the construction of a nonlinear force function table by i) using polynomial or bi-cubic spline curve-fitting

technique [55], ii) using a 2D look-up table [65] and iii) implementing a neural network [66].

The polynomial curve-fitting method requires the least memory, but it involves complex computations, especially in the case of two dimensional calculations. The bi-cubic spline strategy can be more precise if the order of approximation is high. However, higher order computation requires more computational effort, because there are many matrix coefficients needed to be computed online. The second method is the fastest and requires least computation, but the memory requirement may be very large if a high resolution output is required. The last method also involves heavy computation load. It is best used for learning unknown nonlinear functions. In this case the characteristics motor can be fully determined from experiment and there is no need for a neural network.

6.3.2 Linearization scheme for the planar switched reluctance motor

To optimize between computation efficiency and memory consumption, a pair of low-resolution two dimensional look-up tables are used for each axis of motion with bi-linear interpolation to calculate the intermediate values [31].

Since force, current, and position are related in three dimensions, a 2D force-current-position look-up table for each axis is sufficient to describe the nonlinear force profile. To find out the inverse relationship between current, force and position, another experiment has been conducted by fixing the moving platform at corresponding positions within one pole width, and then currents are measured to generate the desired force [31]. Alternatively, the table can be generated from the inverse function of force versus current and position.

Fig.6.10 and Fig.6.11 demonstrate the method of obtaining the required current i^* by bi-linear interpolation method. Firstly, from the position input x and force command f^* , two pairs of data $i(f_1, x_1)$, $i(f_1, x_2)$ and $i(f_2, x_1)$, $i(f_2, x_2)$ in the look-up table are located. For each pair, a linear interpolation is done according to the ratio of f_1 , f_2 and f^* . As a result, two intermediate elements, $i(f_{1-2}, x_1)$ and $i(f_{1-2}, x_2)$ can be obtained. Finally, the output current command i^* is obtained by interpolating the two intermediate elements with x_1 and x_2 .

For the implementation of the inverse force current position look-up tables, continuity and smoothness of the profile are more important than accuracy. Therefore a relatively low 27×27 -matrix is applied to build up the look-up table for the force compensation values. To ensure smoothness, a two dimensional linear interpolation scheme is implemented for the intermediate values. This produces a considerably low worst-case deviation from the original nonlinear function and the output values can also follow a smooth profile. A 27×27 elements look-up table with two dimensional linear interpolation is sufficient to describe the force profile with an error of $\pm 5\%$ [31].

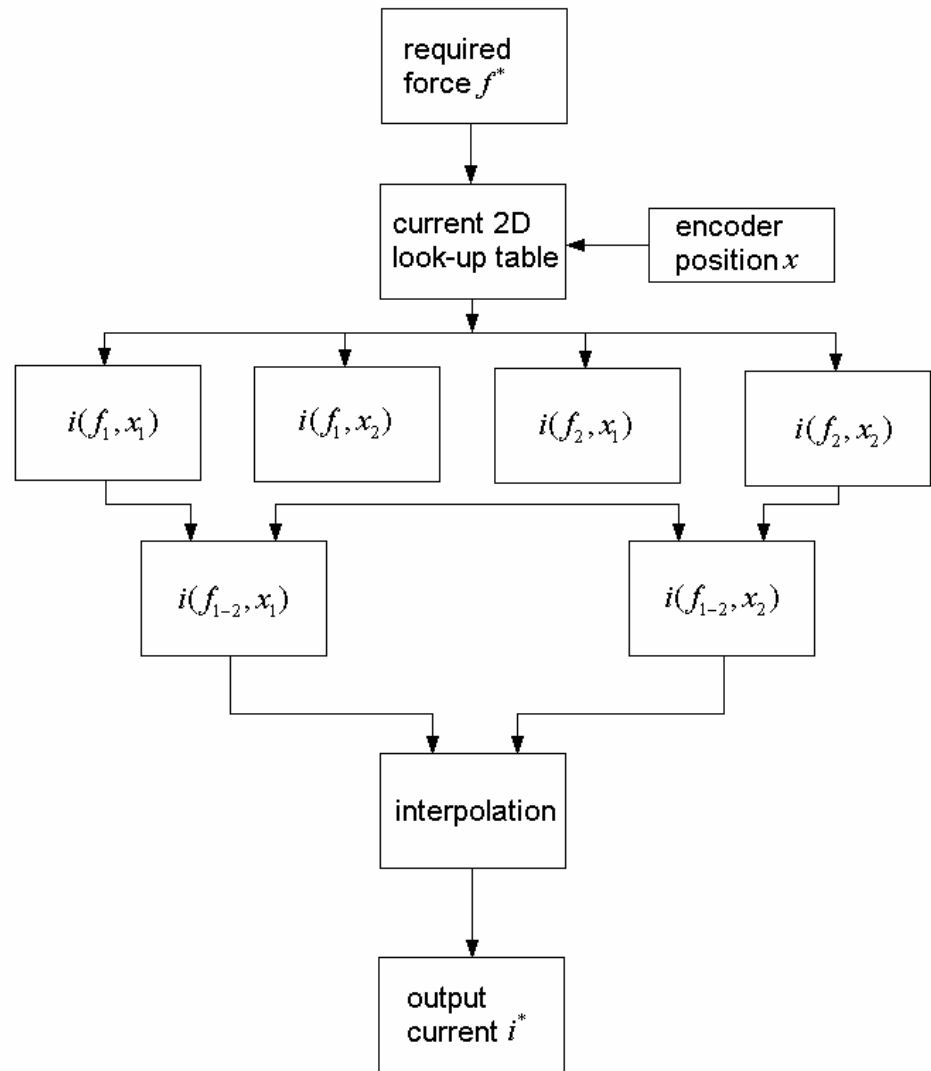


Fig.6.10 Flow chart for obtaining i^*

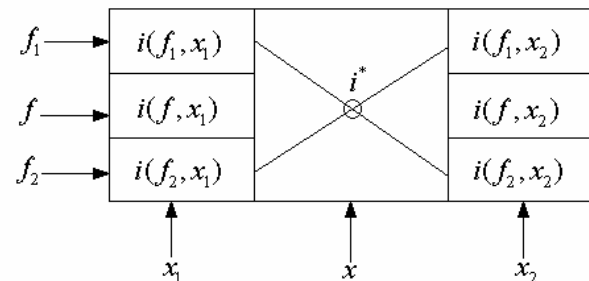


Fig.6.11 Bi-linear interpolation from the look-up table

6.3.3 Experiment verification

To further verify that the nonlinearity can be compensated from the above proposed force control scheme as shown in Fig.6.9, an experiment regarding to the measurement of input and output force is performed. From the 3D relationship as shown in Fig.6.12 (a), there are force variations according to different positions with force command as a parameter. As shown in Fig. 6.12 (b), the 2D relationship shows that output force changes with input force approximately in a linear way. Therefore the linearization scheme of the force input and output is confirmed to be successful.

Relationship between force input and output

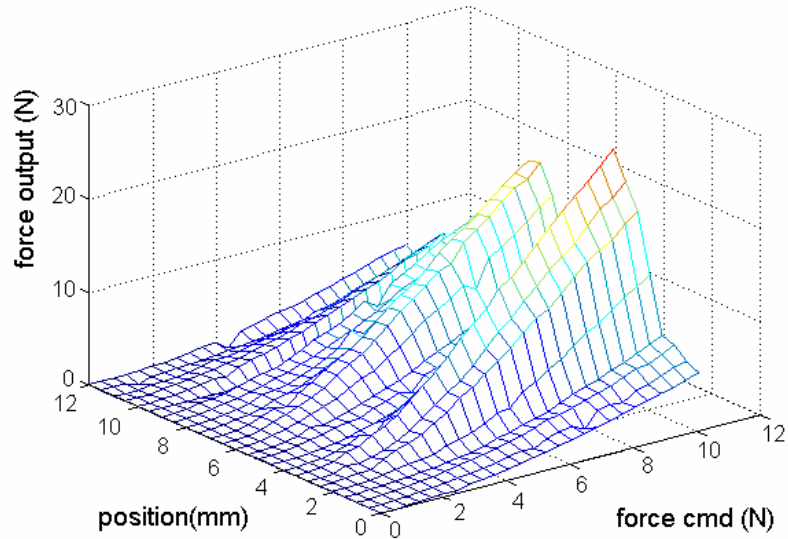


Fig.6.12 (a) 3D relationship between force output with respect to position and force command

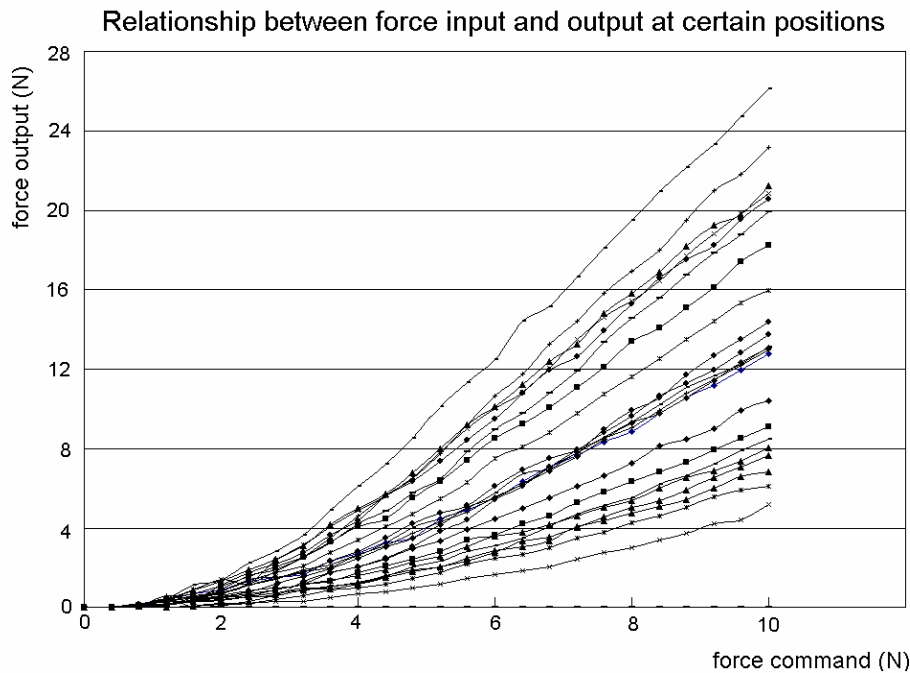


Fig.6.12 (b) 2D relationship between force output and force command at certain positions

The introduction of a nonlinear function $h(x, f^*)$ with respect to position and force command can fully describe the force control loop in Fig.6.8. Therefore the diagram can be redrawn as below in Fig.6.13.

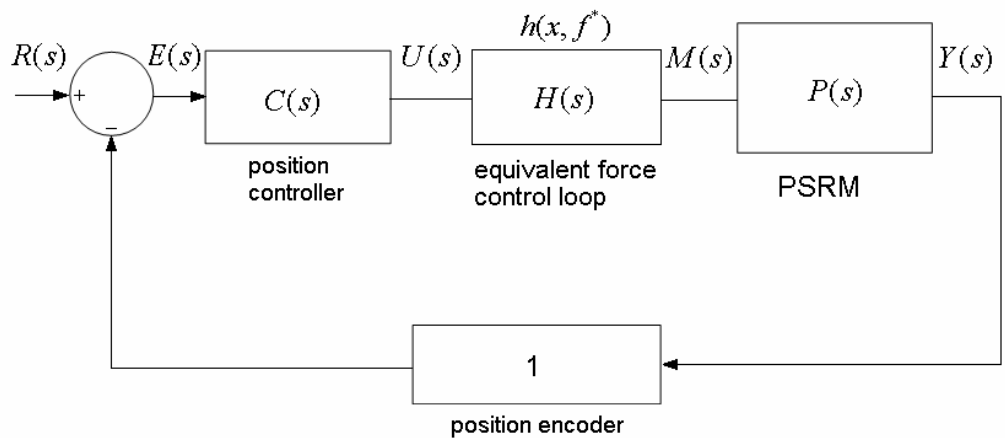


Fig.6.13 Simplified position control block

Since the output force should have the same polarity with force command, the

equation can be satisfied as,

$$h(x, f^*) > 0 \quad (6.13)$$

6.4 The position controller

The position controller forms the essential part of the slow subsystem. Its operation is based on the assumption that the current controller has perfect tracking capability and linearity. In order to have a good control of force, current must be highly stable, fast in dynamics and excellent in linearity with minimal drifting of current against time and temperature.

6.4.1 The Proportional Derivative (PD) controller

The equivalent open loop transfer function of the PSRM for one axis can be described as a typical second order differential equation,

$$M\ddot{x} + B_v\dot{x} + f_l = K_s \sum_{k=a}^c f_k(i_k(t), x(t)) = K_s f \quad (6.14)$$

where f is the totally generated electromechanical force, f_l is load, and M , B_v are the mass and friction constant for the axis of motion respectively. K_s is a constant of 1000, the conversion from unit millimeter to meter.

From Fig.6.13 above and regardless of load, the open loop transfer function for the PSRM is,

$$P(s) = \frac{Y(s)}{M(s)} = \frac{X(s)}{F(s)} = \frac{K_s}{Ms^2 + B_v s} \quad (6.15)$$

For the position controller, a simple and effective PD controller is considered with the form

of,

$$C(s) = K_p + K_d s \quad (6.16)$$

where K_p and K_d are the proportional and derivative gain respectively.

Therefore the closed loop transfer function for the whole control block can be expressed as,

$$H'(s) = \frac{Y(s)}{R(s)} = \frac{(K_p + K_d s) \cdot H(s) \cdot \frac{K_s}{Ms^2 + B_v s}}{1 + (K_p + K_d s) \cdot H(s) \cdot \frac{K_s}{Ms^2 + B_v s}} = \frac{K_s \cdot H \cdot (K_p + K_d s)}{Ms^2 + (B_v + K_d K_s H)s + K_p K_s H} \quad (6.17)$$

$$\text{Let } a = K_s K_d H \text{ and } \lambda = \frac{K_p}{K_d}, \text{ then } H'(s) = \frac{as + a\lambda}{Ms^2 + (B_v + a)s + a\lambda} \quad (6.18)$$

The transfer function has one zero $z = -\lambda$ and two poles,

$$s_{1,2} = \frac{-(a + B_v) \pm \sqrt{(a + B_v)^2 - 4Ma\lambda}}{2M} \quad (6.19)$$

Here $M > 0$, $B_v > 0$, $K_s > 0$ and $H > 0$ are satisfied. Since the parameters for the position controller are always positive with $K_p > 0$ and $K_d > 0$, it can be concluded that the two poles of the closed loop transfer function are all located on the left-hand plane. Therefore

the system is stable. Since $\lambda = \frac{K_p}{K_d} \ll 1$ and $\lambda \ll Bv$, the transfer function can be simplified

as $H(s) = \frac{as + a\lambda}{Ms^2 + as + a\lambda}$. Moreover, the only zero point ($z = -\lambda$) is located far from origin compared with zero points of the system, thus the effect of this zero point can be neglected and the effect of the two poles are considered as dominant.

Therefore the transfer function can be further simplified as,

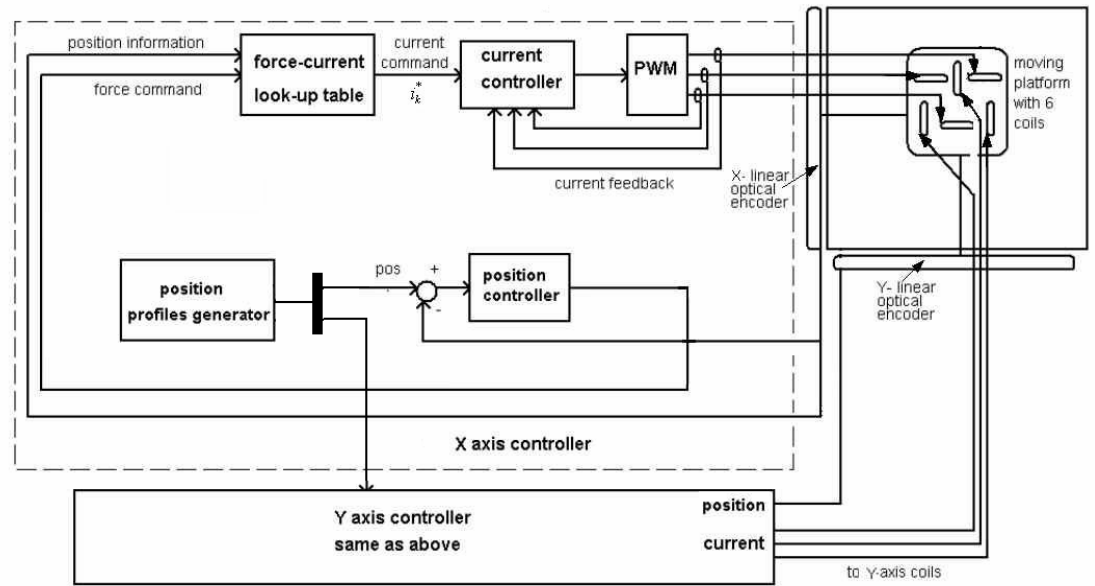
$$H'(s) = \frac{1}{Ms^2 + as + a\lambda} \quad (6.20)$$

where the damping ratio $\zeta = \frac{1}{2} \sqrt{\frac{a}{M\lambda}}$ and natural frequency $\omega_n = \sqrt{\frac{a\lambda}{M}}$ can be derived

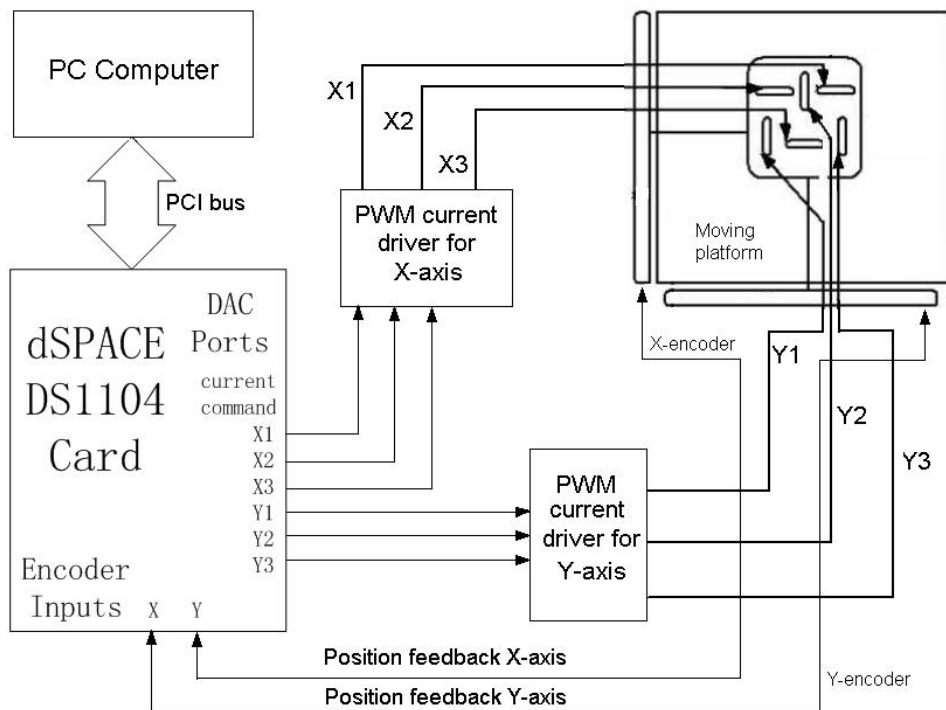
compared with a typical second order system [67].

6.4.2. Experiment results

Practically the machine works under the command of low-change-rate tracking profile. So sinusoidal waveforms are suitable as test signals for the PSRM. To verify the machine is capable of decoupled operation, a pair of “*sin*” and “*cos*” signals is selected as the tracking command for each axis of motion respectively. Under the compound command signal with no coupling effect between each axis, the motor will run as a circle. The control block and experiment setup diagram is given in Fig.6.14 below [31].



(a)

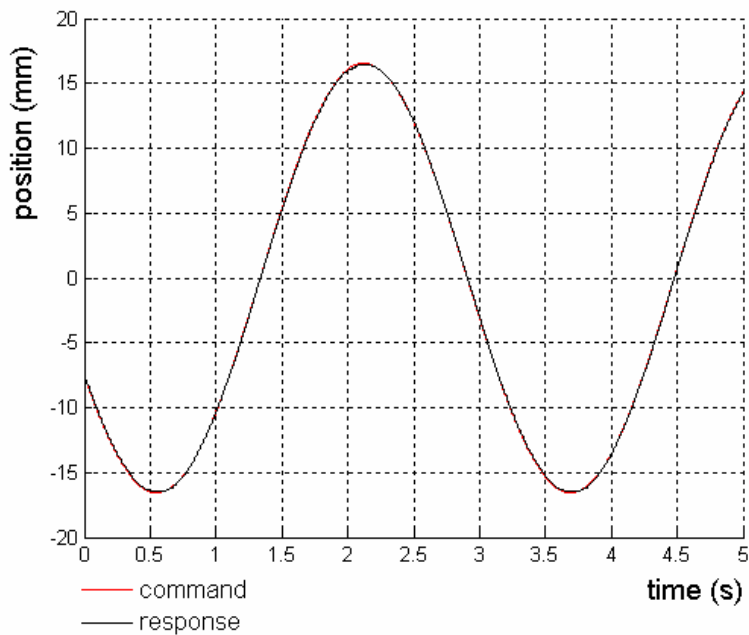


(b)

Fig.6.14 (a) Control block of the PSRM and (b) the experiment setup

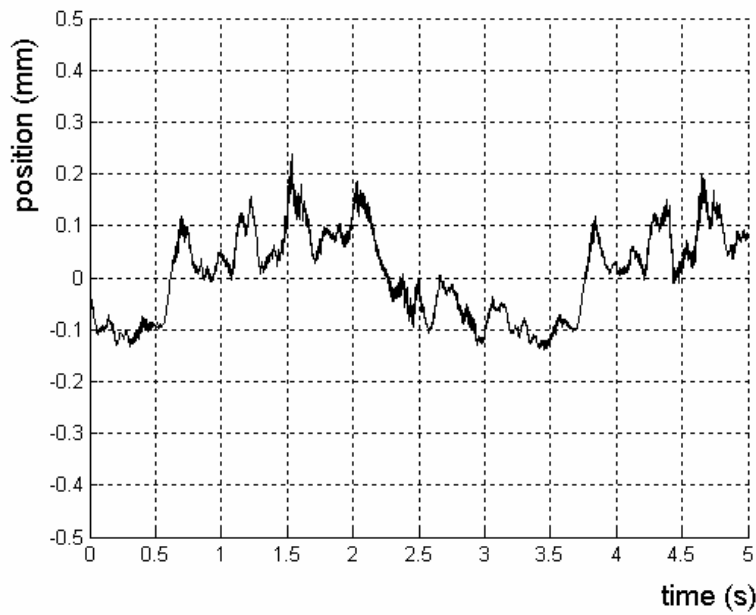
The experiment results are given below as shown in Fig.6.15 (a)—(d) and Fig.6.16.

Tracking response of X-axis

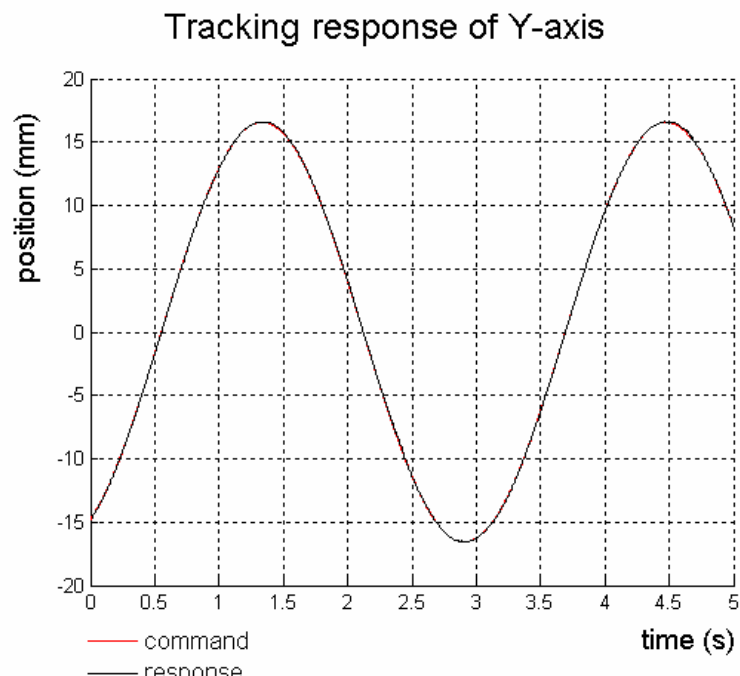


(a)

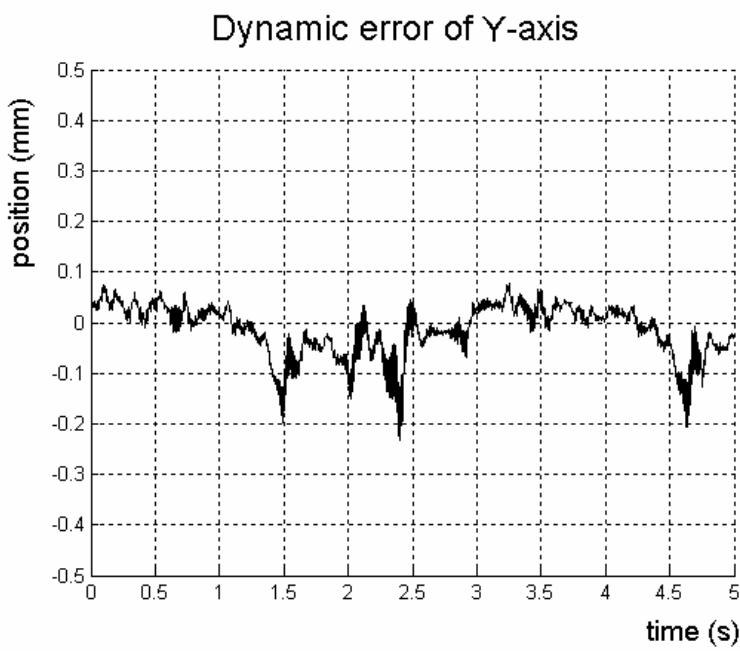
Dynamic error of X-axis



(b)



(c)



(d)

Fig.6.15 Trajectory response of the PSRM for circular motion. (a) Response of the X-axis (b) Tracking error of the X-axis (c) Response of the Y-axis (d) Tracking error of the Y-axis

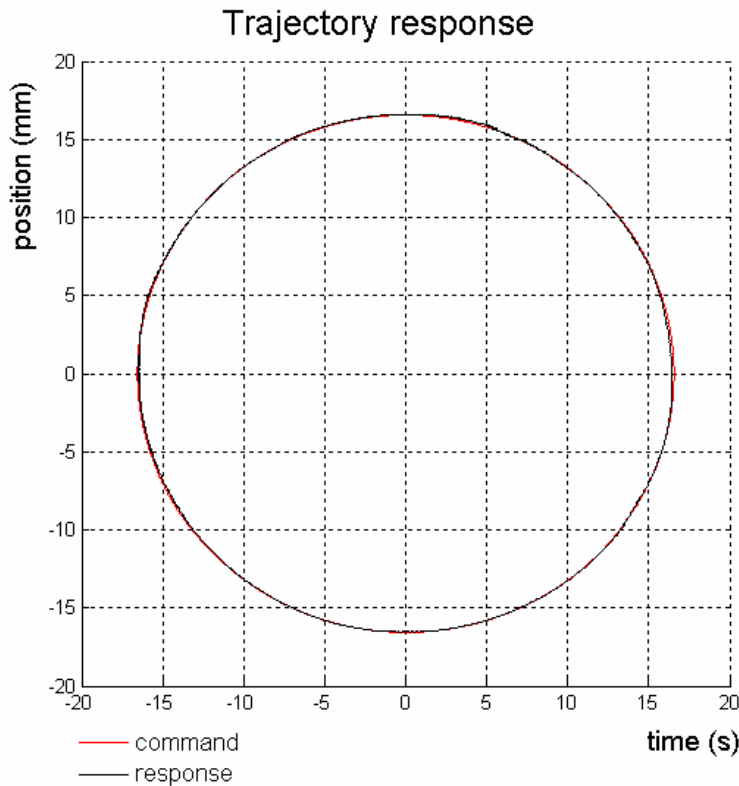


Fig.6.16 Overall performance

The tracking profiles show that each axis of motion is capable of following the command signal precisely. The command signal and response almost overlap for both axes as shown in Fig.6.15 (a) and (c). The error dynamics can be found in Fig.6.15 (b) and (d). The absolute errors fall within 0.2 mm, 1.2% of the total range (16.56 mm). It is clear that for both diagrams, the errors for opposite directions are not identical in each axis of motion. This is because the mechanical structures in both axes are not uniform such that the motor experiences unbalanced frictions at different positions. However, from the above experiment results, the position controllers are capable of correction for such imperfections that exist in mechanical manufacture and the simple yet effective feature of the controller ensures the implementation for future industrial applications of the PSRM.

As can be seen from Fig.6.15 (b) and (d) as well, there is no regular rules where the

maximum errors would occur during full range of operation for each axis of motion. If the anchor point (position=0 mm) is altered, the overall distribution of maximum error will change accordingly. This phenomenon is due to model uncertainties and real-time disturbances both from mechanical and electrical aspects. Therefore it is expected that an advanced control algorithm can be applied to compensate these uncertainties and disturbances in real-time operations.

6.5 The dual-loop position controller

6.5.1 Introduction

The transfer function of the error-input for any one axis of motion can be derived from the control block as shown in Fig.6.13 and the equation as given below,

$$\frac{E(s)}{R(s)} = \frac{Ms^2 + B_v s}{Ms^2 + (B_v + K_d K_s h(x, f^*)) s + K_p K_s h(x, f^*)} \quad (6.21)$$

According to PID tuning methods, to meet the dynamic response of a second order system with proper overshoot and fast enough rising time, the proportional gain K_p is often set to a large value while the derivative gain K_d is small. By further exploring the above equation, it can be deducted that the steady error with a sinusoidal input signal is not virtually zero.

A simulation for the response of the above error system is performed with sinusoidal input signal by increasing input frequency from 0—20 Hz. The diagram in Fig.6.17 shows that at first the error response becomes larger as frequency increases, then decreases to some extent but it never reaches zero. Due to the mechanical and electrical constraints, the PSRM is designed to operations under a frequency of 2 Hz with a peak-to-peak range of 30 mm

from the input command signal. The corresponding experiment results of X-axis at 0.5 Hz and 1 Hz are conducted and the dynamic error response is shown in Fig.6.18 (a) and (b) respectively. As shown in the diagrams, error increases prominently as the frequency gets larger. Therefore the error-input transfer function behaves as a high-pass filter.

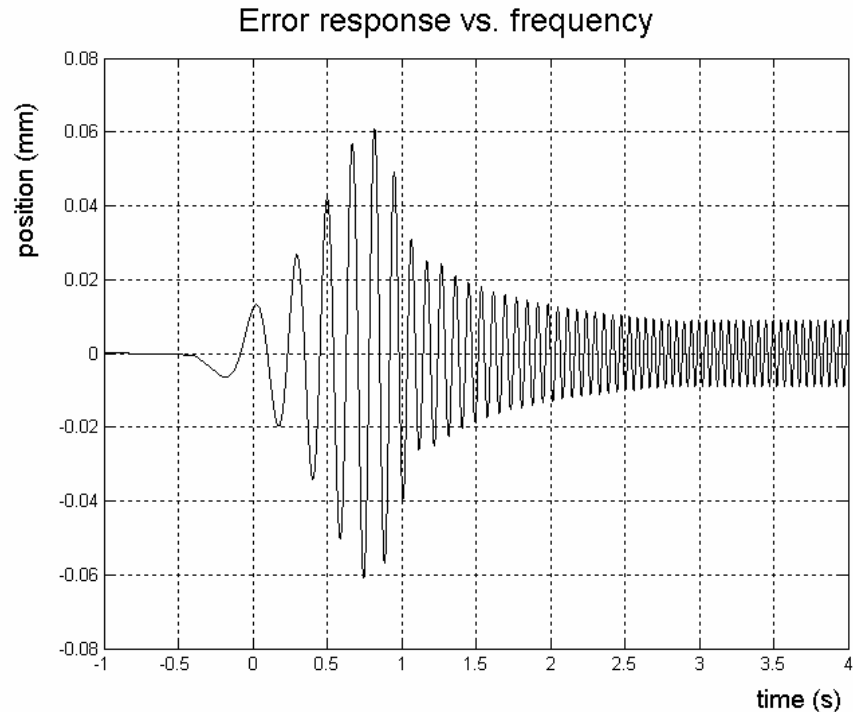
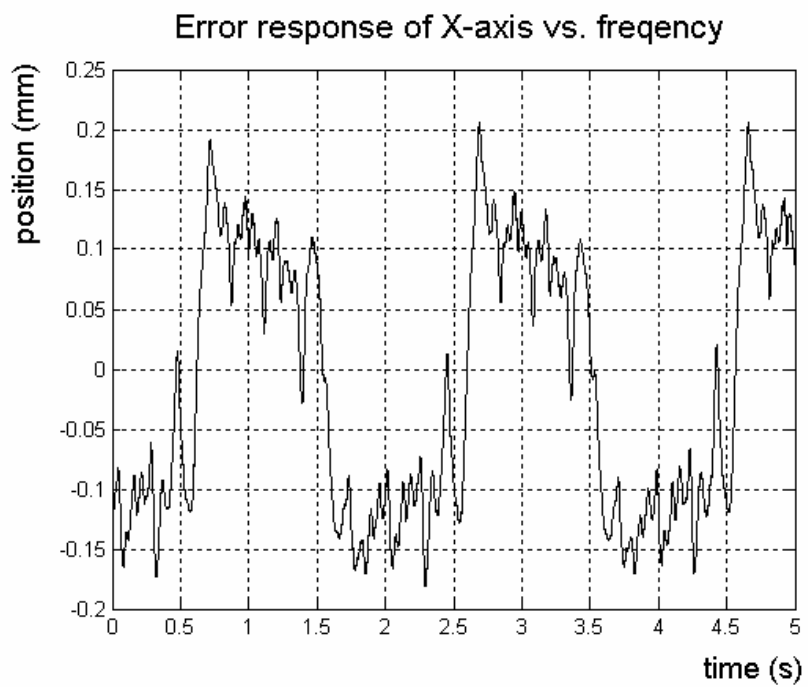
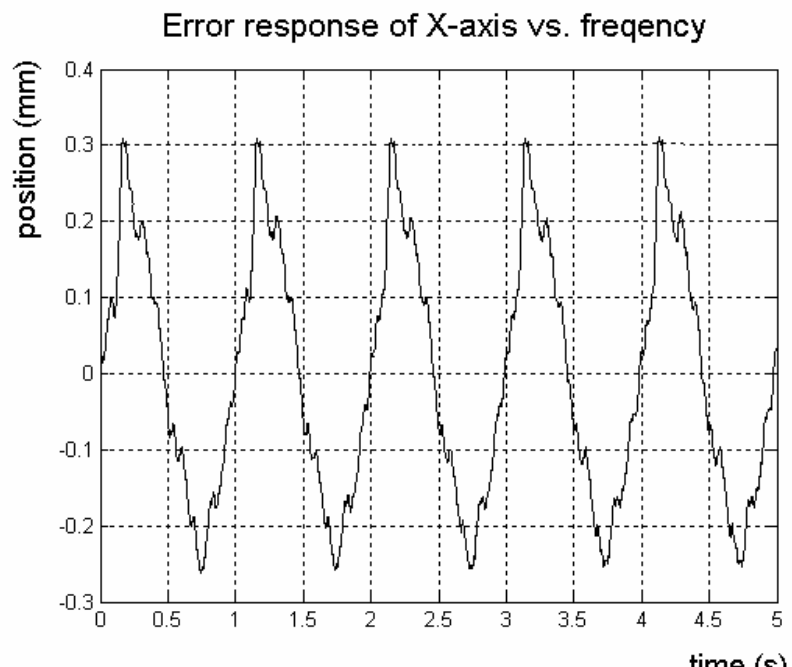


Fig.6.17 Error response from simulation



(a)



(b)

Fig.6.18 Error response from experiment for X-axis at (a) 0.5 Hz and (b) 1 Hz

6.5.2 Controller derivation

The goal of the construction of the dual-loop controller is to transform the error-input function into a low-pass filter and decrease the error to zero in the low frequency band.

An inner proportional loop with feedback is added after the position controller as shown in Fig.6.19 [68].

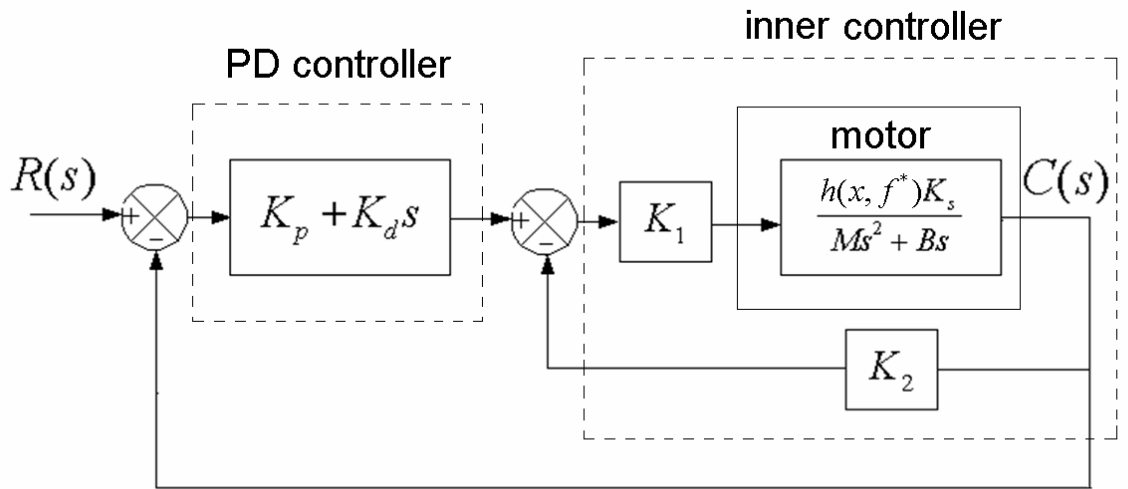


Fig.6.19 The construction of the inner controller

Here K_1 and K_2 are the proportional gains. Then the system becomes,

$$\begin{aligned} \frac{C(s)}{R(s)} &= \frac{K_1 K_s h(x, f^*) \cdot (K_p + K_d s)}{Ms^2 + (B_v + K_1 K_s K_d h(x, f^*))s + K_1 K_s (K_2 + K_p) h(x, f^*)} \\ &= \frac{K(s + \lambda \omega_n \zeta)}{s^2 + 2\omega_n \zeta s + \omega_n^2} \end{aligned} \quad (6.22)$$

where $K = \frac{K_1 K_d K_s h(x, f^*)}{M}$, damping ratio $\zeta = \frac{B + K_1 K_d K_s h(x, f^*)}{2\sqrt{MK_1 K_s (K_p + K_2) h(x, f^*)}}$, natural

frequency $\omega_n = \sqrt{\frac{K_1 K_s h(x, f^*) (K_p + K_2)}{M}}$ and $\lambda = \frac{2MK_p}{K_d (B + K_1 K_s K_d h(x, f^*))}$. Then the poles

can be found as,

$$s_{1,2} = \frac{-\left(B_v + K_1 K_s K_d h(x, f^*)\right) \pm \sqrt{\left(B_v + K_1 K_s K_d h(x, f^*)\right)^2 - 4M K_1 K_s (K_p + K_2) h(x, f^*)}}{2M} \quad (6.23)$$

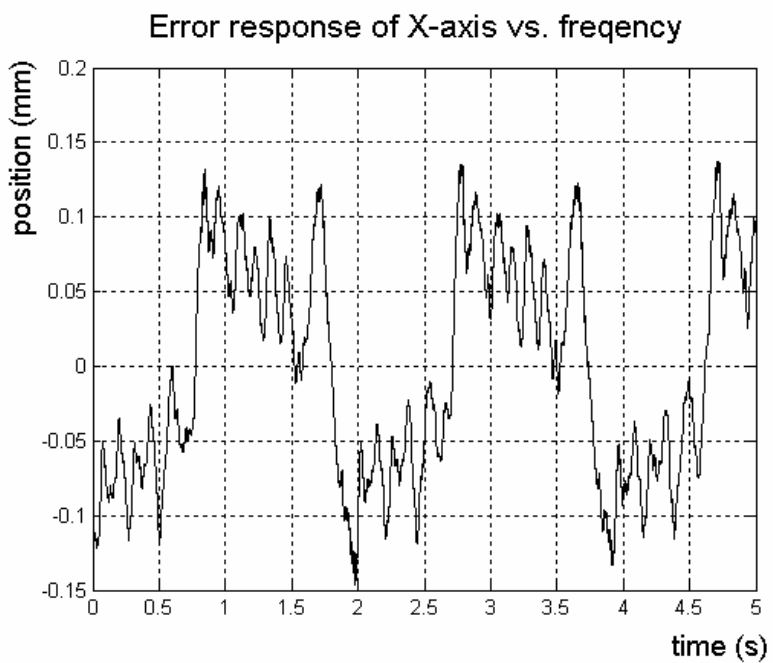
The variables or constants in the equation are all positive. The real part of the poles can be negative if K_1, K_2, K_s and K_p are properly chosen. Furthermore, after K_1 and K_2 are set, $K_1 K_2 K_s h(x, f^*) \square M s^2 + B_v s$ can be satisfied in low frequency bands. Then the error-input transfer function of the new system becomes,

$$\frac{E(s)}{R(s)} = \frac{K_1 K_2 K_s h(x, f^*)}{M s^2 + \left(B_v + K_1 K_s K_d h(x, f^*)\right) s + K_1 K_s (K_2 + K_p) h(x, f^*)} \quad (6.24)$$

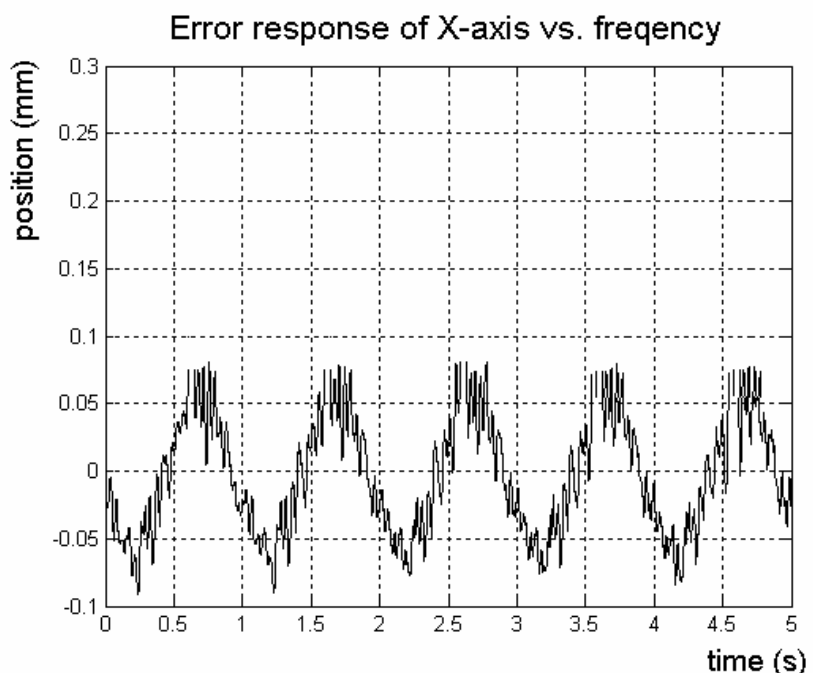
The error approaches zero as long as the difference between the order of numerator and denominator is less than two from the transfer function of the input signals, so the model belongs to a II-type (second order error free) system [67]. As can be seen from the above equation, the error decreases when the frequency of the input signal increases.

6.5.3 Experiment verifications

Experiment is conducted for X-axis of motion only. Input frequency varies from 0.5 to 1 Hz at a peak-to-peak range of 30 mm. From the experiment results shown in Fig.6.20 (a) and (b), error response from X-axis of motion has a tendency of decreased error for increased signal frequency. It can be concluded from the experiment result that the dual-loop controller is effective for the regulation of error response under increased frequency.



(a)



(b)

Fig.6.20 Error response under dual-loop position controller for X-axis at (a) 0.5 Hz and (b) 1 Hz

6.6 Summary

In this chapter, an effective current controller is first proposed as the inner loop controller. Before the implementation of an appropriate position controller, a multi-phase excitation scheme for the smooth operation of the PSRM is incorporated with a 2D look-up table as the linearization strategy. Experiment results verify that force output varies linearly with force command with position as a parameter. Then a simple and effective PD controller is implemented. Through experiment verification, the PD controller is confirmed to be effective and practical. Finally, an improved dual-loop position controller is proposed which aims at reduced dynamic error with increased frequency. Both theoretical deduction and experiment results verify the effectiveness of the improved controller.

Chapter 7

Speed regulation with auto-disturbance rejection control (ADRC)

7.1 Introduction

After the implementation of the position controller on the novel planar switched reluctance motor, velocity control has been carried out and results are compared with a classical PID controller. Experiment results demonstrate that the motor's operation is more resistant to disturbances under different operations with ADRC control scheme.

In trajectory control applications, it is often required that velocity response should strictly follow a smooth profile as well to ensure a proper transient process for position tracking. The PSRM is a direct-drive machine that eliminates the use of mechanical translators such as gears and belts. However, some of the advantages inherent in mechanical transmissions are lost, like the ability to reduce the effects of model uncertainties and external disturbances.

Modern control engineering usually uses model based state-space representation to obtain a suitable nonlinear control algorithm. The basis of analysis and synthesis relies on an accurate mathematic model of the control object [67]. However, the model is not easily attainable in many engineering problems. Even if it is available, the consequent control law could be too dependent on the accuracy of the model parameters and suffer poor robustness.

Therefore an effective control strategy which is based on general characteristics of the

working process in real-time is in high demand. Among the widely used control methods in practice is the Proportional Integral Derivative (PID) control and it dominates over 90% of the industrial applications [69]. Since it is based on process control strategy, where the controller makes decisions according to the error information, it does not rely on detailed mathematical model of the object. Its easy-to-implement feature also makes it an inevitable choice for industrial applications. However, PID controllers consist of a few fundamental weaknesses. These include i) derivation of signal noise, and ii) the treatment of error behaviors.

For the derivative signals' noise, sometimes the reference signal cannot be differentiated or the derivatives are hard to retrieve or the actual output signal is populated by noise. Therefore, the differential signals from the difference between actual and reference signal may be distorted or the noise could be amplified from the output of a classical differentiator.

A classical form of a typical differentiator can be described as,

$$y(t) = w(s) * v = \frac{S}{(\tau S + 1)v} = \frac{1}{\tau} \left(1 - \frac{1}{\tau S + 1} \right) v \approx \frac{1}{\tau} (v(t) - v(t - \tau)) \approx \dot{v}(t) \quad (7.1)$$

where $v(t)$, $y(t)$ is input and output signal, respectively, $w(s)$ is the transfer function of some system. If noise $n(t)$ is added, the above equation can be modified as,

$$y(t) \approx \frac{1}{\tau} (v(t) - v(t - \tau)) + \frac{n(t)}{\tau} \approx \dot{v}(t) + \frac{1}{\tau} n(t) \quad (7.2)$$

It can be seen that the amplification of noise becomes very serious when τ is a very small value.

For the problem of the treatment of different error behaviors—past ($\int edt$), present (e) and future (de/dt), a common PID controller can be described as,

$$u = K_p * e(t) + K_d * \frac{de(t)}{dt} + K_i * \int e(t) * dt \quad (7.3)$$

where u is controller output, $e(t)$ is the error between reference and actual output signals. K_p , K_d and K_i are the coefficients for the proportional, derivative and integral loop.

In a typical PID controller, the different error states (past, present and future) are combined by simple linear summations with weighting factors K_p , K_d and K_i . This can unavoidably lead to the conflict between response time and overshoot [70].

7.2 The auto-disturbance rejection controller

To combat the problems inherent in PID control of the planar motor, a novel control strategy based on auto-disturbance rejection control (ADRC) scheme is proposed [84]. The ADRC concept is derived from the idea of using nonlinear configuration assignment feedback based on process control strategy [82]. It is initially applied to industrial applications such as time-variant, highly coupled systems [71, 72]. Because it does not rely on exact mathematical model and the whole disturbance including model inconsistency together with outside disturbance can be compensated, the interest of applications in motion control area is increasing. Past work proves its successful implementation on permanent magnetic motor [73, 74] and induction motor [75]; it is also applied on different kinds of motion systems with satisfactory results [76, 77]. Moreover, an ADRC control scheme is more suitable than a PID controller for this type of motor, since the un-modeled parameter variations and external disturbances, can be observed and compensated by the control system in real-time. Therefore, the motor is much more robust and more resistant to external disturbances.

7.2.1. Whole structure

A typical ADRC controller is shown in Fig.7.1 and it consists of the following parts,

- i) Tracking Differentiator (TD)
- ii) Nonlinear State Error Feedback (NLSEF)
- iii) Extended State Observer (ESO)

The TD is responsible for the arrangement of an appropriate transient process and provides proper differential signals of each order from the input reference signal; the NLSEF block determines control input by tracking error signal and its different formats for optimal combinations with nonlinear algorithms for output; the core for an ADRC controller is ESO, which can observe system uncertainties and external disturbances and feed them back for compensation.

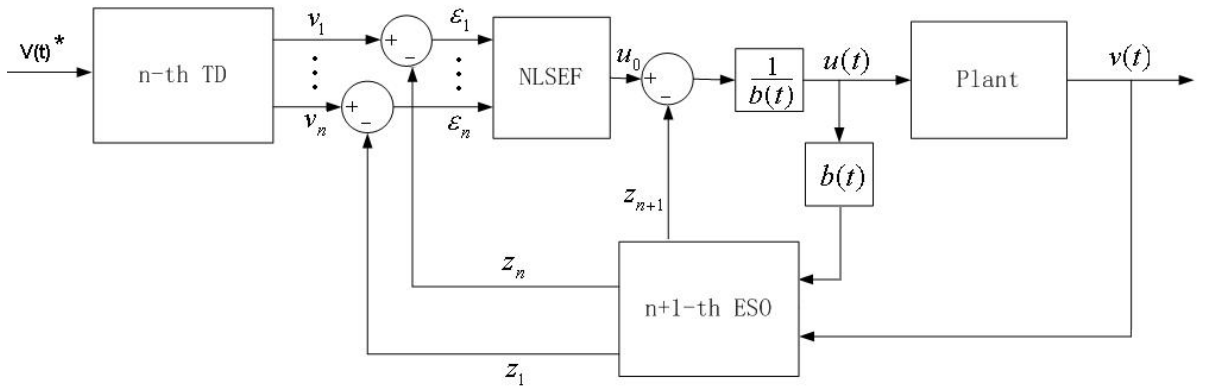


Fig.7.1 The ADRC control block

7.2.2 Tracking differentiator (TD)

In motor control systems, the differential signal is usually obtained by backward difference of the given signal such as position. Unavoidably, it will contain certain amount of stochastic noise. TD can resolve the problem of differential signal extraction via

integration. Detailed description of a tracking differentiator can be found in [70, 78].

For any dynamic system described as the following equations below,

$$\begin{cases} \dot{x}_1 = x_2 \\ \dot{x}_2 = -g(x_1, x_2) \end{cases} \quad (7.4)$$

The following theorem exists that if the system is stable at origin, then for any bounded integrable function $v(t)$, $t \in [0, \infty)$ there exists,

$$\begin{cases} \dot{x}_1 = x_2 \\ \dot{x}_2 = R^2 g(x_1 - v(t), x_2 / R) \end{cases} \quad (7.5)$$

that satisfies, $\lim_{R \rightarrow \infty} \int_0^T |x_1(R, t) - v(t)| dt = 0$. x_1 tracks reference $v(t)$, and $x_2(R, t)$ approximates to the “generalized differentiation” of $v(t)$ [78]. Besides, as long as R is sufficiently large, x_1 can track $v(t)$ arbitrarily fast with certain precision.

Generally a second order TD takes the following form of,

$$\begin{cases} \varepsilon_0 = v_1 - v^* \\ \dot{\varepsilon}_1 = -r^* fal(\varepsilon_0, a_0, \delta_0) \end{cases} \quad (7.6)$$

where v^* is the reference velocity, v_1 is the tracking signal, r , a_0 and δ_0 are parameters to be regulated. The *fal* function is expressed as,

$$fal(\varepsilon, a, \delta) = \begin{cases} |\varepsilon|^a \operatorname{sgn}(\varepsilon), & |\varepsilon| > \delta \\ \frac{\varepsilon}{\delta^{1-a}}, & |\varepsilon| \leq \delta \end{cases} \quad (7.7)$$

The most important feature of a TD is its capability to obtain the derivatives of noisy signals with a good signal to noise ratio and the derivatives are acquired via integration [70]. Therefore, TD can avoid unnecessary noise and be used as a reference generator as well.

7.2.3 Nonlinear state error feedback (NLSEF)

A PID controller simply takes the linear summations with weighting factors as the

controller output, which is problem oriented and difficult for repeatability of different problems [70, 79]. While in an ADRC, the errors are combined with nonlinear manners and the parameters can be regulated according to the actual response of output performance.

A typical nonlinear relationship for a n-th NLSEF can be expressed as,

$$u_0 = k_1 fal(\varepsilon_1, \alpha, \delta) + \dots + k_n fal(\varepsilon_n, \alpha, \delta) \quad (7.8)$$

where $k_i (i=1\dots n)$, α , and δ are parameters to be regulated. ε_i is error signal and its derivatives are obtained from a n-th order TD. The *fal* function is derived from Equ.7.7. The reason why a nonlinear combination of error signals over a linear one can be explained from the graphic interpretation below.

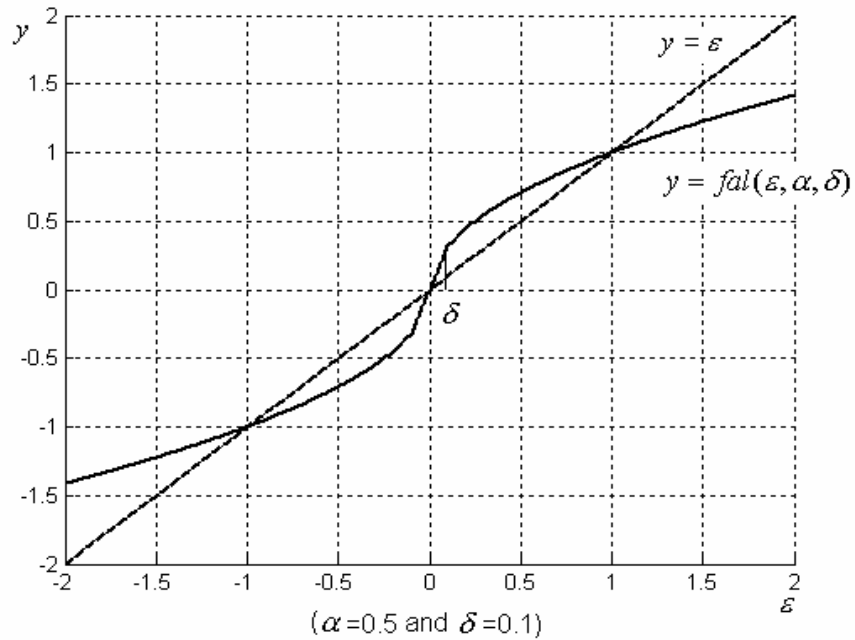


Fig.7.2 Comparison of linear and nonlinear gains

Fig.7.2 shows that, at higher gains, error is relatively small and it becomes larger at lower gains, while the gain remains uniformly the same in the linear combination method. Furthermore, from the graphical illustration, there is a linear region when the error ε falls into the intervals of $\pm\delta$ while the error is getting larger and the gain diminishes accordingly.

This avoids excessive gain when error is small, which might lead to high frequency chattering [70, 78, 79].

7.2.4 Extended state observer (ESO)

The observer construction is derived from the problem that “for a system with the expression,

$$a(t) = f(x, \dot{x}, \dots, x^{(n-1)}(t), t) + u(t) \quad (7.9)$$

where $f(x, \dot{x}, \dots, x^{(n-1)}, t)$ is an unknown function and $u(t)$ is the unknown disturbance, how to construct a nonlinear system which is independent of both the detailed format of function $f(x, \dot{x}, \dots, x^{(n-1)}, t)$ and $u(t)$, so that the system can observe each state variable $x(t) \dots x^{(n-1)}(t)$ ” [80].

Suppose the solution to the above question exists, then the following nonlinear system can be derived as,

$$\begin{cases} \varepsilon = z_1 - x(t) \\ \dot{z}_1 = z_2 - g_1(\varepsilon) \\ \dot{z}_2 = z_3 - g_2(\varepsilon) \\ \vdots \\ \dot{z}_{n+1} = -g_{n+1}(\varepsilon) \end{cases} \quad (7.10)$$

and the system satisfies that each state (from z_1 to \dot{z}_{n+1}) can track corresponding input states correctly, $z_1(t) \rightarrow x(t) \dots z_{n+1}(t) \rightarrow x^{(n)}(t)$.

The system can satisfy the condition that for each state (from z_1 to z_{n+1}), it can track corresponding input states correctly, so that $z_1(t) \rightarrow x(t) \dots z_{n+1}(t) \rightarrow x^{(n)}(t)$. If the above statement is true, and $a(t) = f(x, \dot{x}, \dots, x^{(n-1)}(t), t) + u(t)$ is assigned, then $z_{n+1}(t) \rightarrow x^{(n)}(t) = a(t)$. This means that despite of the unknown formats for both

$f(x, \dot{x}, \dots, x^{(n-1)}, t)$ and $u(t)$, the real-time value of $a(t)$ can be observed and estimated.

Let $x_1(t) = x(t) \dots x_{n+1}(t) = a(t)$, then system 7.10 becomes,

$$\begin{cases} \dot{x}_1(t) = x_2(t) \\ \dot{x}_2(t) = x_3(t) \\ \vdots \\ \dot{x}_n(t) = x_{n+1}(t) \\ \dot{x}_{n+1}(t) = b(t) \end{cases} \quad (7.11)$$

Now let $\delta x_1 = z_1 - x_1(t) \dots \delta x_{n+1} = z_{n+1} - x_{n+1}(t)$, then

$$\begin{cases} \dot{\delta x}_1 = \delta x_2 - g_1(\delta x_1) \\ \dot{\delta x}_2 = \delta x_3 - g_2(\delta x_1) \\ \vdots \\ \dot{\delta x}_{n+1} = -b(t) - g_{n+1}(\delta x_1) \end{cases} \quad (7.12)$$

For any values of $b(t)$ within certain ranges, proper functions $g_1(\delta x_1) \dots g_{n+1}(\delta x_1)$ can be selected to make System 7.12 stable at origin. It is named as “Extended State Observer” such that besides all system states to be observed, $z_1(t) \dots z_n(t)$, the state of both the parameter uncertainties and external disturbances—the extended state, can also be estimated. The convergence derivation of TD and ESO can be found in [78, 80].

From the above reasoning, the format of ESO is irrelevant of System 7.10, but merely dependent on the range of $b(t)$ (change of $a(t)$). Therefore as long as any set of functions $g_1(\delta x_1) \dots g_{n+1}(\delta x_1)$ can be found, the output δx_{n+1} is capable of real-time estimation of the unpredictable altogether. In [80], an approximate design method of function $g(x)$ is proposed.

Let $g_i(\delta x_1) = l_i g(\delta x_1)$, from Equ.7.12,

$$\begin{cases} \dot{\delta x}_1 = \delta x_2 - l_1 g(\delta x_1) \\ \dot{\delta x}_2 = \delta x_3 - l_2 g(\delta x_1) \\ \vdots \\ \dot{\delta x}_{n+1} = -b(t) - l_1 g_{n+1}(\delta x_1) \end{cases} \quad (7.13)$$

where $b(t) = a'(t)$. Suppose $b(t)$ is bounded, $g(x)$ is smooth, and satisfies $g(0) = 0$

and $g'(x) = \frac{dg(x)}{dx} \neq 0$. From series expansion of first derivative at δx_1 ,

$$\begin{cases} \dot{\delta x}_1 = \delta x_2 - l_1 g'(\delta x_1) \cdot \delta x_1 \\ \dot{\delta x}_2 = \delta x_3 - l_2 g'(\delta x_1) \cdot \delta x_1 \\ \vdots \\ \dot{\delta x}_{n+1} = -b(t) - l_1 g'_{n+1}(\delta x_1) \cdot \delta x_1 \end{cases} \quad (7.14)$$

also let $l_i = \frac{k_i}{g'(\delta x_1)}$, the following matrix equation can be derived,

$$\begin{pmatrix} \delta \dot{x}_1 \\ \vdots \\ \delta \dot{x}_{n+1} \end{pmatrix} = \begin{pmatrix} -k_1 & 1 & \cdots & 0 \\ \vdots & 1 & & \\ -k_{n+1} & & \ddots & 1 \end{pmatrix} \begin{pmatrix} \delta x_1 \\ \vdots \\ \delta x_{n+1} \end{pmatrix} + \begin{pmatrix} 0 \\ \vdots \\ -1 \end{pmatrix} \quad (7.15)$$

let $A = \begin{pmatrix} -k_1 & 1 & \cdots & 0 \\ \vdots & 1 & & \\ -k_{n+1} & & \ddots & 1 \end{pmatrix}$, $E = \begin{pmatrix} 0 \\ \vdots \\ -1 \end{pmatrix}$ the compact matrix form can be derived as,

$$\ddot{\delta x} = A \delta x + Eb(t) \quad (7.16)$$

where $\ddot{\delta x} = (\delta \ddot{x}_1, \delta \ddot{x}_2, \dots, \delta \ddot{x}_n)^T$. If the eigenvalues all fall into the left-hand side of the complex plane, and are sufficiently negative, then despite of the bounded disturbance of $b(t)$, Equ.7.15 can be ensured stable and converge to origin sufficiently fast enough [70].

Therefore parameters $k_1 \dots k_{n+1}$ must satisfy,

$$|SI - A| = \prod_{i=1}^{n+1} (S - P_i) \quad (7.17)$$

and P_i are poles to be chosen.

From the above, $g(x)$ must meet the following necessary conditions,

- i) $g(x)$ is continuous and differentiable

ii) $g(0) = 0$

iii) $g'(x) = \frac{dg(x)}{dx} \neq 0$ (7.18)

Different forms of $g(x)$ can be selected such as $g_i(x) = \beta_i \tanh(x)$ or $g_i(x) = \frac{1-e^{-x}}{1+e^{-x}}$.

It is obvious that the system is a classical Luenberger observer when $gx_i = x_i$ ($i = 1 \dots n+1$) and is a variable structure observer when $gx_i = x_i + k_i \text{sign}(x_i)$, ($i = 1 \dots n+1$) [71, 83].

7.3 Construction of the velocity controller

For SR motors, the external disturbances may include the change of load or friction. For parameter uncertainties, there maybe i) change of mechanical parameters such as mass and friction coefficient and ii) variations of electrical characteristics, such as the change of winding resistance or control signal fluctuations.

The force equation of the planar motor for one axis can be represented as,

$$M\dot{V} + BvV + f_l(t) = \sum_{k=a}^c f_k(i_k(t), x(t)) = f_{x(y)} = u_q \quad (7.19)$$

where $f_{x(y)}$ is the totally generated electromechanical force, $f_l(t)$ is load force, and M , Bv , are the mass and the friction constant, respectively. If disturbances and uncertainties are concerned, then the equation becomes,

$$\dot{V} = (\square B + B_m)V + (\square A + A_m)f_l + (\square A + A_m)u_q \quad (7.20)$$

where $B_m = \frac{-B_v}{M}$, $A_m = \frac{-1}{M}$ and $\square B$, $\square A$ are parameter variations. The equation can be further represented as,

$$\dot{V} = F_w + B_m V + A_m u_q$$

$$\begin{aligned}
&= F_w - \frac{B_v}{M} V + \frac{1}{M} u_q \\
&= a(t) + b u_q
\end{aligned} \tag{7.21}$$

where $F_w = \square BV + (\square A + A_m)f_l + \square Au_q$ which includes all external disturbances and system uncertainties; $b = 1/M$ and $a(t) = F_w - \frac{B_v}{M}V$. The above differential equation for velocity only include i) the compositive uncertainties $a(t)$ and ii) the control parameter bu_q .

Therefore, if the compositive item can be observed correctly by ADRC and fed back to the system, the model of this SR motor for one axis becomes a first order system. Also, the other axis can be treated as the same way since two axes of motion are highly decoupled. Thus, the controller for the system can be expressed as,

$$u(t) = (u_0(t) - a(t))/b \tag{7.22}$$

where $a(t)$ is the observation of total uncertainties and disturbances from ESO.

Since each axis of motion is perfectly decoupled, the controllers for X- and Y-axis can be designed individually. The main differences between the two directions are mainly mover mass and friction. Therefore, after a controller of one axis of motion is designed, the one for another motion can be obtained with only slight modifications.

The control object is focused on velocity. Take X-axis of motion for example. The input for TD is speed command and it will arrange a proper transient process which has the output form of,

$$V1(t) = -r_{_Tx} \cdot fal(V1 - V, \delta_{_Tx}, \alpha_{_Tx}) \tag{7.23}$$

where $r_{_Tx}$, $\delta_{_Tx}$ and $\alpha_{_Tx}$ are parameters to be regulated. Then the output $V1$ is compared with the observed state of speed fed back from ESO, and the difference is determined by the NLSEF block to give a proper u_0 ,

$$u_0 = \beta_{_Nx} \cdot fal(\varepsilon, \delta_{_Nx}, \alpha_{_Nx}) \quad (7.24)$$

Three more regulated values $\beta_{_Nx}$, $\delta_{_Nx}$ and $\alpha_{_Nx}$ are included. Then the control force input u_q for the motor becomes,

$$u_q = \frac{1}{b}(u_0 - Z_2) \quad (7.25)$$

b is a constant and $b = 1/M$. The actual measured velocity value from the encoder will be fed back to ESO for state observation, the velocity state Z_1 and the extended state Z_2 are derived from the following,

$$\begin{cases} \dot{Z}_1 = bu_q + Z_2 - \beta_{01_EX} \cdot fal(Z_1 - V_{bak}, \delta_{EX}, \alpha_{EX}) \\ \dot{Z}_2 = -\beta_{02_EX} \cdot fal(Z_1 - V_{bak}, \delta_{EX}, \alpha_{EX}) \end{cases} \quad (7.26)$$

Again, four parameters β_{01_EX} , β_{02_EX} , δ_{EX} and α_{EX} to be regulated are introduced. Then the whole control block can be derived from above and is shown in Fig.7.3. (The footnotes TX, EX and NX stand for parameters for TD, ESO and NLSEF of X-axis.)

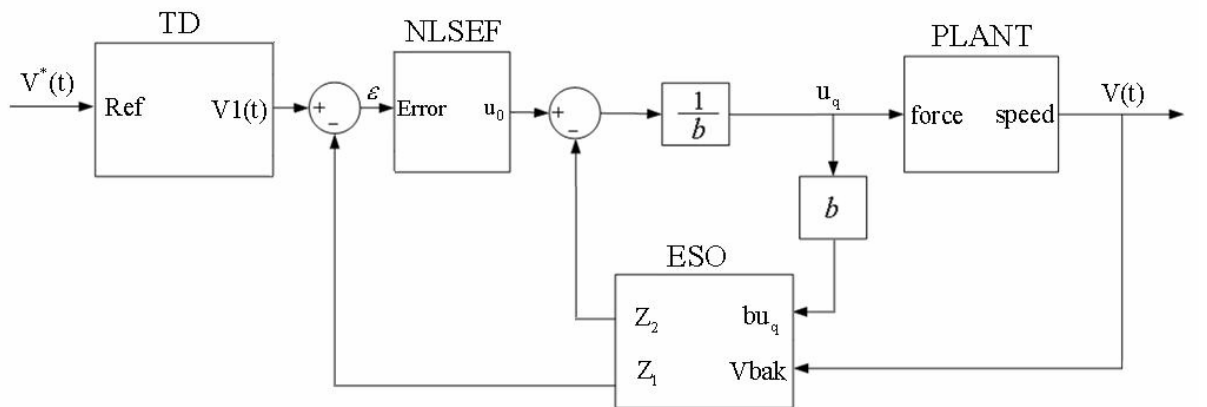


Fig.7.3 ADRC scheme for velocity control

On the motor's side, considering one axis of moving, first a region decision mechanism shall take the combined force command from the ADRC controller, then according the mover's current position, the required force value for each phase is calculated. The amount of force value and the number of phases to be excited depend on both current position and

the moving direction that the mover is required to move. The linearization scheme described in Chapter 6 is implemented.

Concerning the parameter regulations of an ADRC, the whole system is adjusted empirically on simulation and experiment basis. The parameters for TD block are mainly based on the arrangement of a proper transient process and the capability of tracking reference signal successfully within a certain error range. ESO can be configured according to “pole-zero assignment” method to observe every state of each order and estimate the unpredictable (extended state) precisely. NLSEF decides the stable error and it can be designed on such a basis [81].

Up till now, there is no article that has successfully proved the control stability of ADRC system. The parameter regulation depends on the designer’s experience with trial-and-error.

The entire control scheme is a typical two dual-rate cascaded loop control. The control object is velocity, and the control scheme is ADRC to track required speed reference signal satisfactorily. To prevent the motor from shifting and collision from other side, a range limit scheme is included on top of the ADRC. Fig.7.4 shows the entire control diagram.

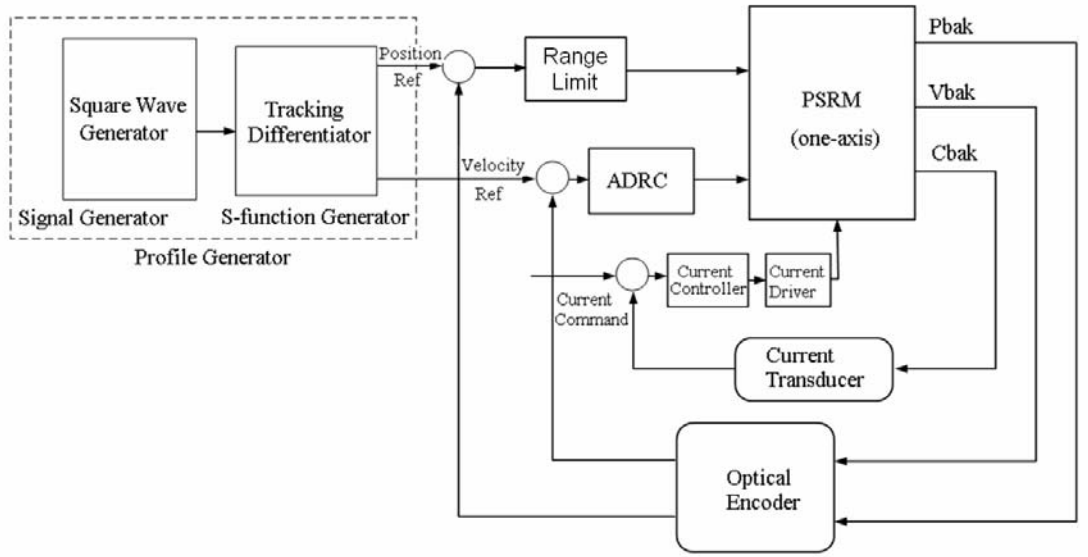


Fig.7.4 The whole control diagram of the controller

7.4 Simulation results

To verify the proposed control scheme, simulation focused on the performance comparisons between an ADRC and a PID controller has been carried out. They are performed under the following conditions,

- i) $M = 3M_0$
- ii) Load increase from 0 to 20 N
- iii) Friction increases 10%

Sudden change of the above parameters occurs at time=0.2 s in all cases. The PID parameters are selected according to a typical dynamic response of the system and further fine-tuned by repeated trial-and-error.

Fig.7.5 (a) shows that the PID controller has reasonable recover time while tracking is just satisfactory if the mass changes. The result becomes deteriorated on load and friction variations as shown in Fig.7.6 (a) and Fig.7.7 (a). For the motion system under ADRC, as

shown in Fig.7.5 (b), Fig.7.6 (b), and Fig.7.7 (b), the response remains the same for all situations. The simulation results prove the ADRC has higher robustness than a PID controller.

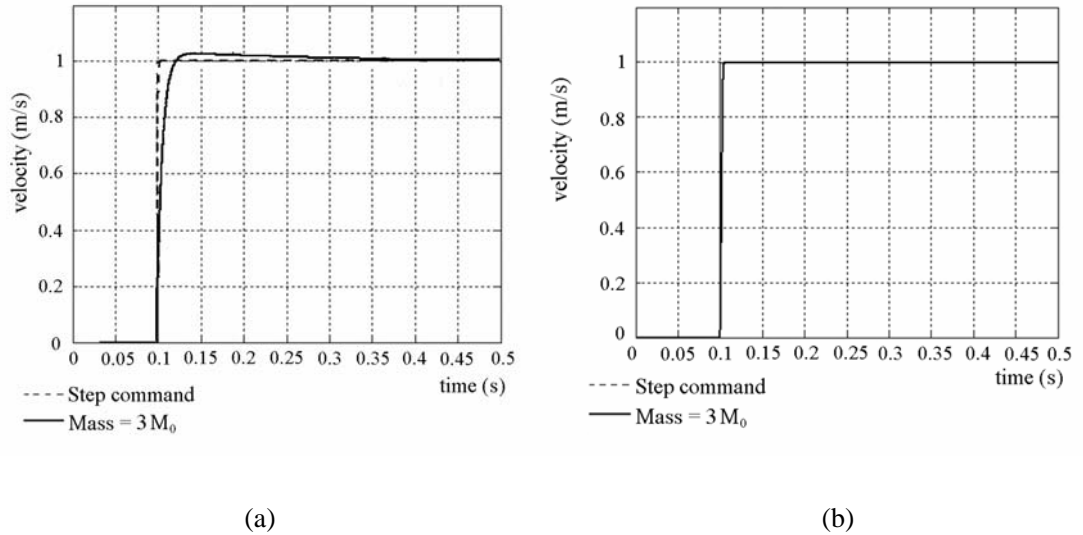


Fig.7.5 Response of mass change from (a) PID (b) ADRC

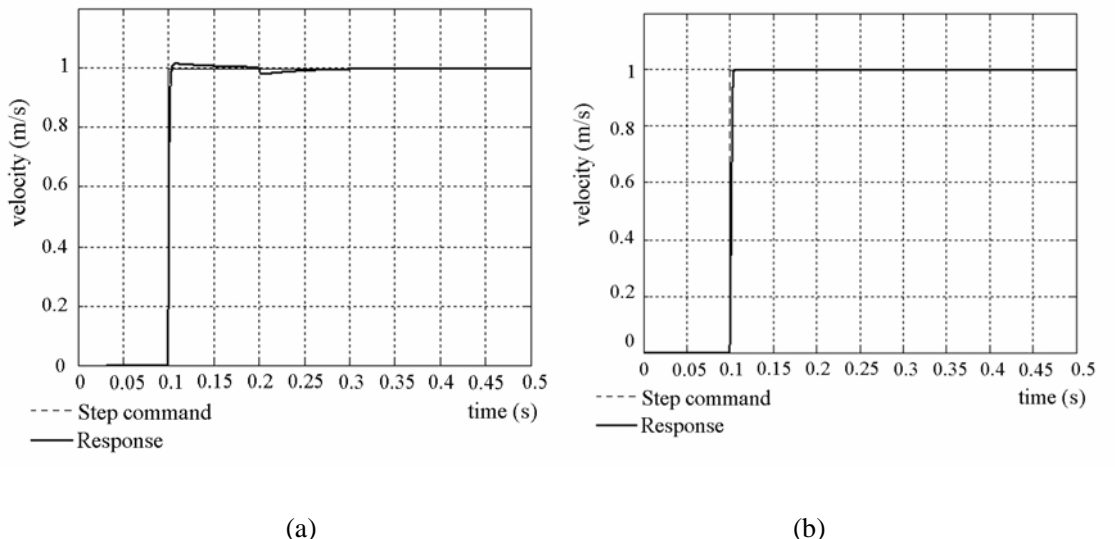


Fig.7.6 Response of PID (a) and (b) ADRC for load change at 0.2 s

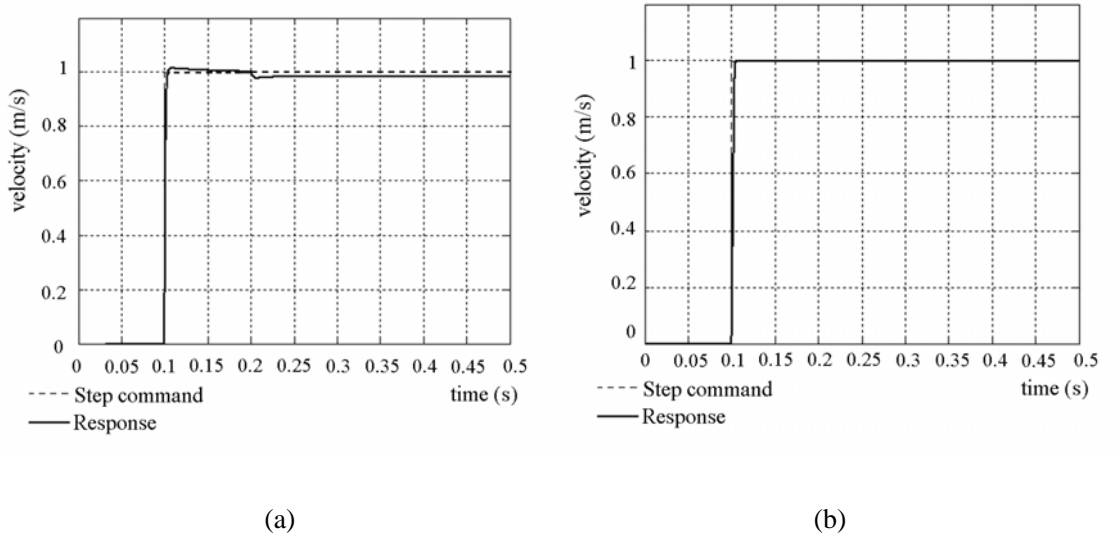


Fig.7.7 Response of PID and ADRC controller at friction variation at 0.2s

7.5 Experiment results

The experiment is mainly focused on the performance comparisons of speed regulation between a PID controller and ADRC. It is composed of two steps. The parameters for both controllers according to frequency 0.5 Hz and amplitude 20 mm are first regulated and in the following experiments, the parameters remain unchanged. Then the frequency is increased to 1 Hz with amplitude unchanged to observe the motor's behaviors from the two controllers. Next, based on the same parameters (0.5 Hz, 20 mm), some kinds of disturbances are added to the motor to study the response from both controllers. Fig.7.8 and Fig.7.9 show the block diagram and experiment setup respectively.

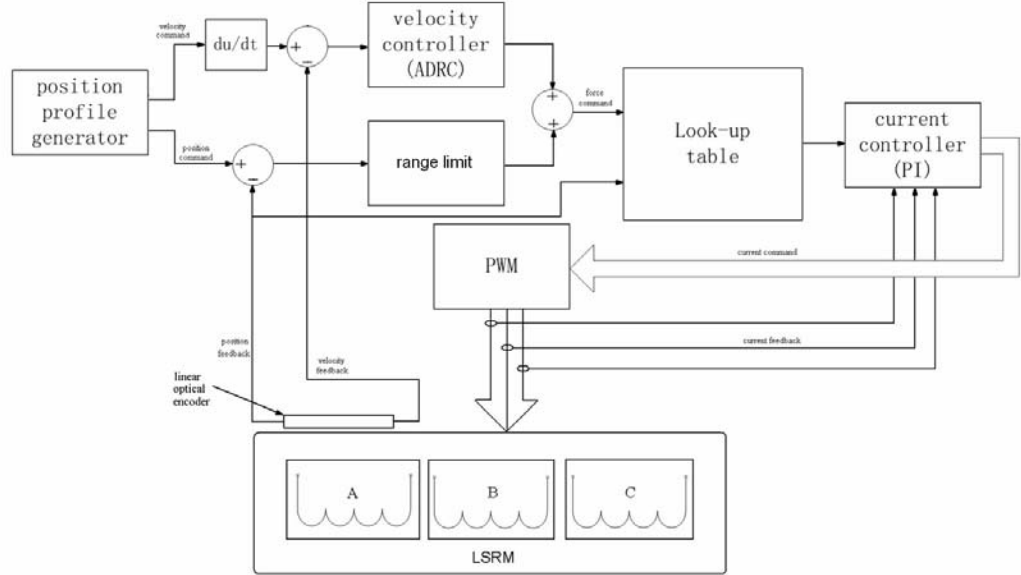


Fig.7.8 Block diagram of the whole control scheme

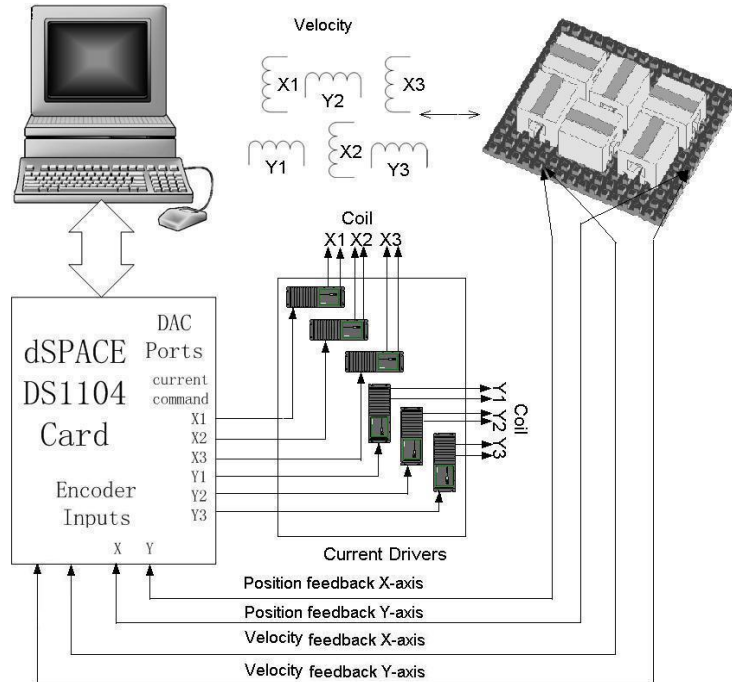


Fig.7.9 Overall experiment setup

The position command is an S-function signal and its profile is generated from a TD with the input signal as a purely square wave. The TD block can arrange a proper transient process and the velocity command is obtained from the other output port of TD.

Response of each axis from PID controller with position command at 0.5 Hz and

amplitude of 20 mm are shown in Fig.7.10 below. Parameters for PID and ADRC regulation are tabulated in Table 7.1.

There is some noise in velocity response under PID control for X-axis. Due to the mechanical asymmetry of the motor structure, there exists little position errors for each direction of movement. Noise also appears in velocity response under ADRC control scheme (Fig.7.11). Compared with the PID controller, the noise is lower and the velocity is a smooth curve during zero-crossing region.

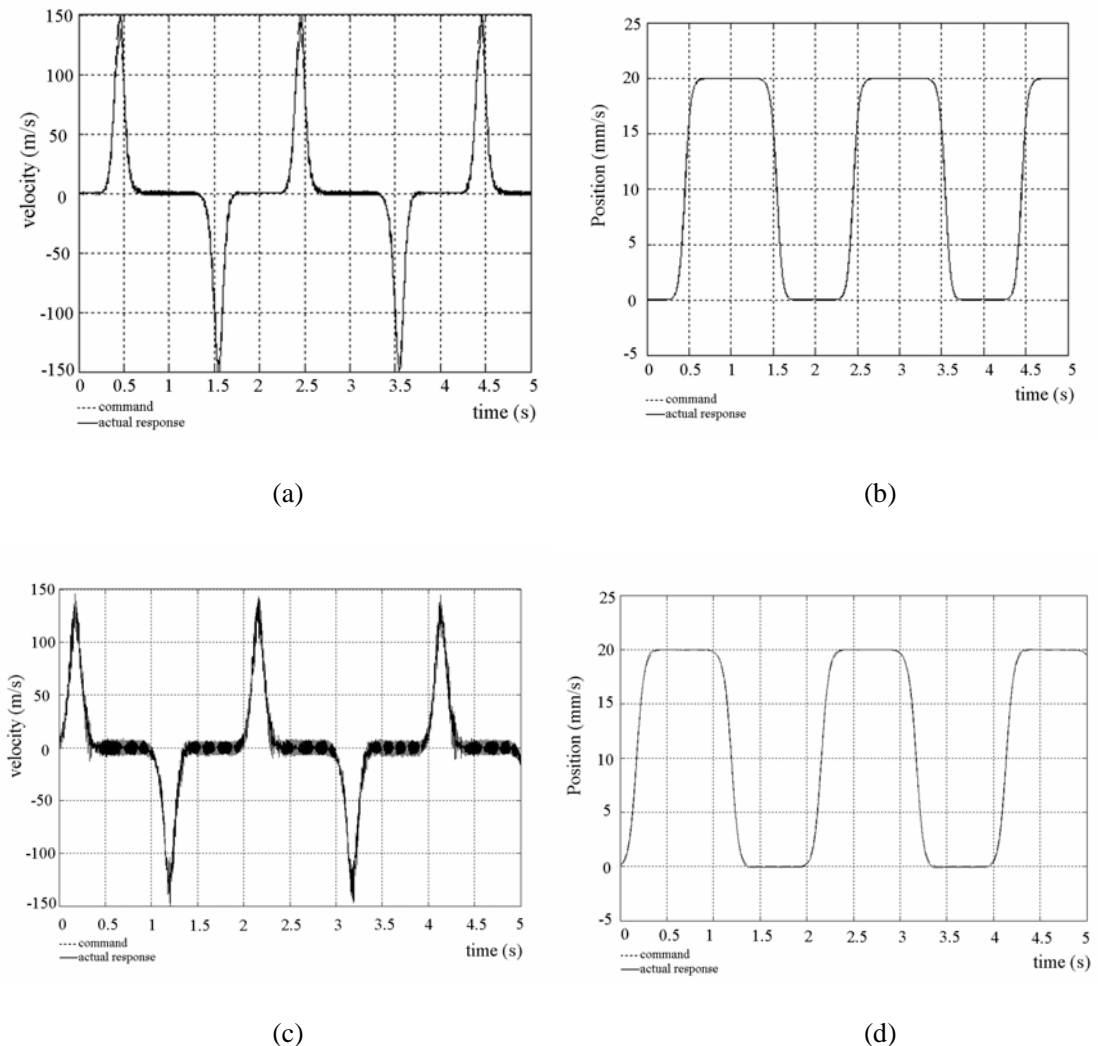
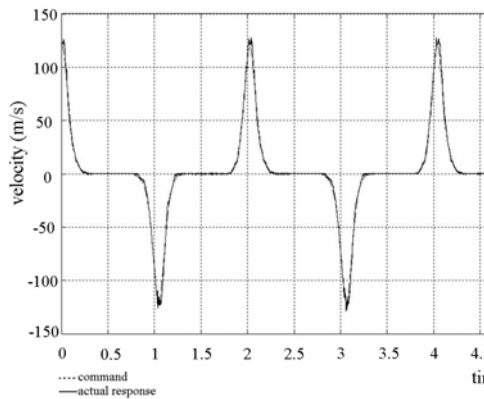


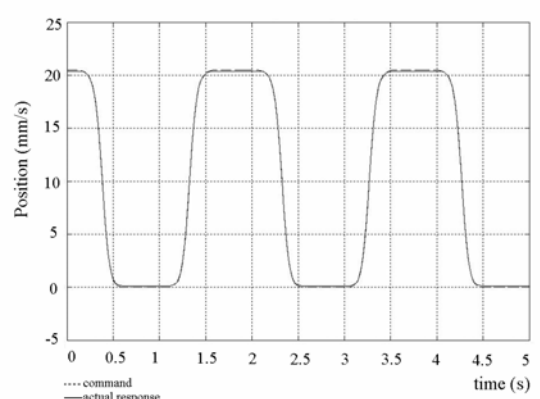
Fig.7.10 Response of PID controller under 0.5 Hz, 20 mm (a) Velocity response of X-Axis (b) Position response of X-Axis (c) Velocity response of Y-Axis (d) Position response of Y-Axis

PID			ADRC										
			TD			ESO				NLSEF			
X	P	D	I	r_T	a_T	δ_T	B01_E	B02_E	a_E	δ_E	B1_N	a_N	δ_N
	42	2.5	0.2	3000	0.9	0.8	800	150	0.2	0.1	150	0.5	0.01
Y	P	D	I	r_T	a_T	δ_T	B01_E	B02_E	a_E	δ_E	B1_N	a_N	δ_N
	60	4	0.1	5000	0.9	0.9	1500	100	0.1	0.1	100	0.9	0.01

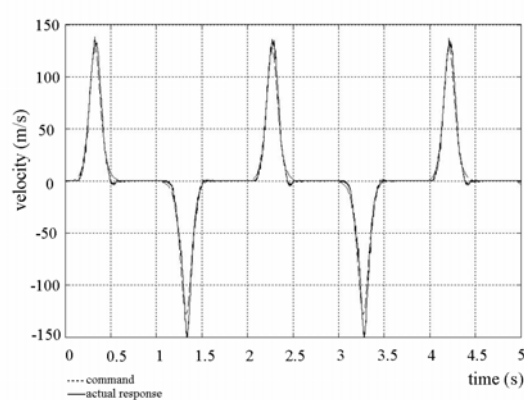
Table 7.1 Parameter regulation



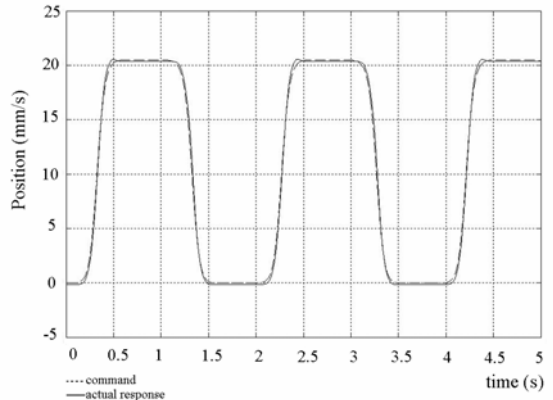
(a)



(b)



(c)



(d)

Fig.7.11 Response of ADRC controller under 0.5 Hz, 20 mm (a) Velocity response of X-Axis (b)

Position response of X-Axis (c) Velocity response of Y-Axis (d) Position response of Y-Axis

Then the frequency is increased to 1 Hz. Since the mass is much lighter for the X-axis mover, the velocity performance is more satisfactory with the same parameters unchanged. Also, the Y-axis moving platform cannot track the velocity reference signal correctly and the dynamic error is quite huge (Fig.7.12). This is because the Y moving platform is heavier and has more inertia. Fig.7.13 illustrates the motor behavior under ADRC control scheme. Both axes have good velocity output performance. It can be concluded that the motor under ADRC is resistant to such model variations.

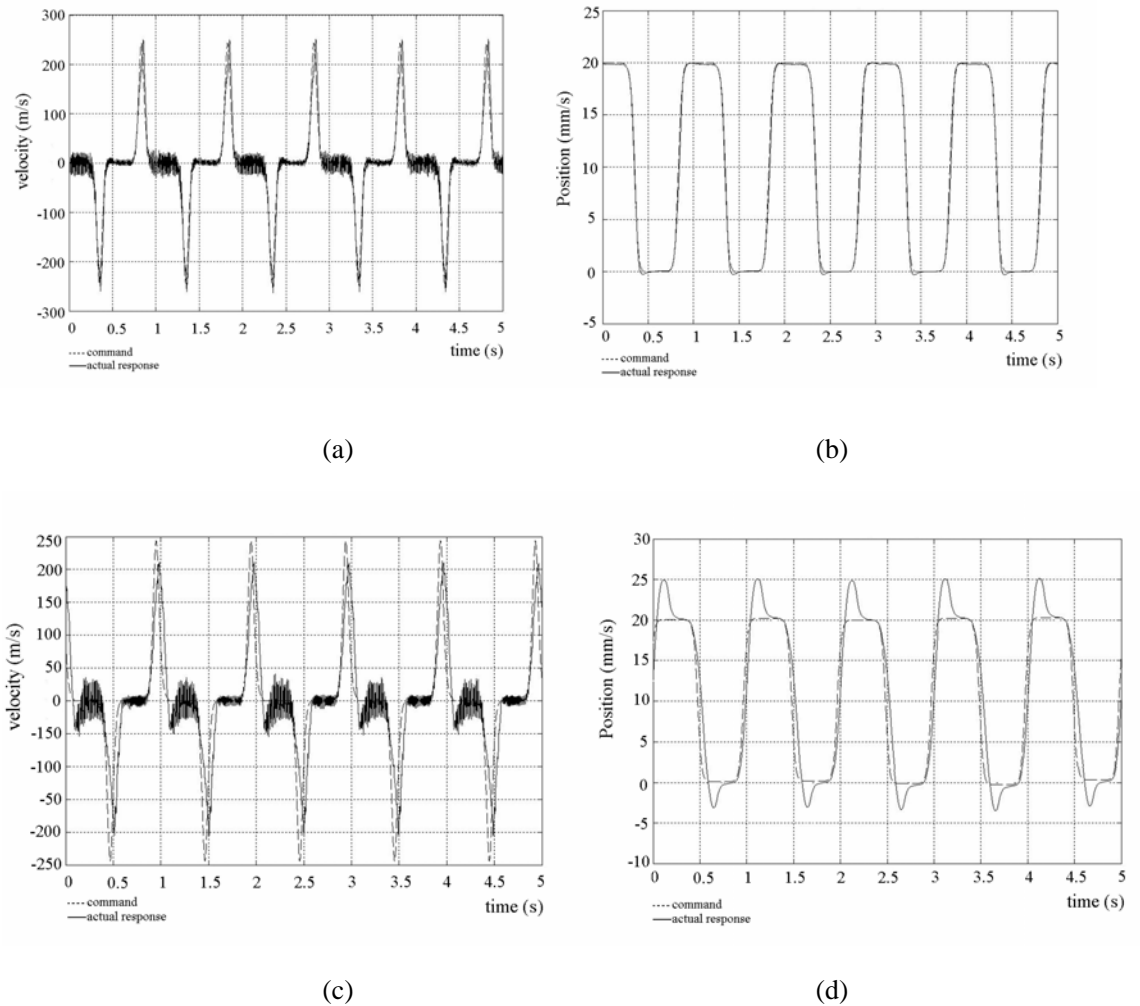


Fig.7.12 Response of PID controller under 1 Hz, 20 mm (a) Velocity response of X-Axis (b) Position response of X-Axis (c) Velocity response of Y-Axis (d) Position response of Y-Axis

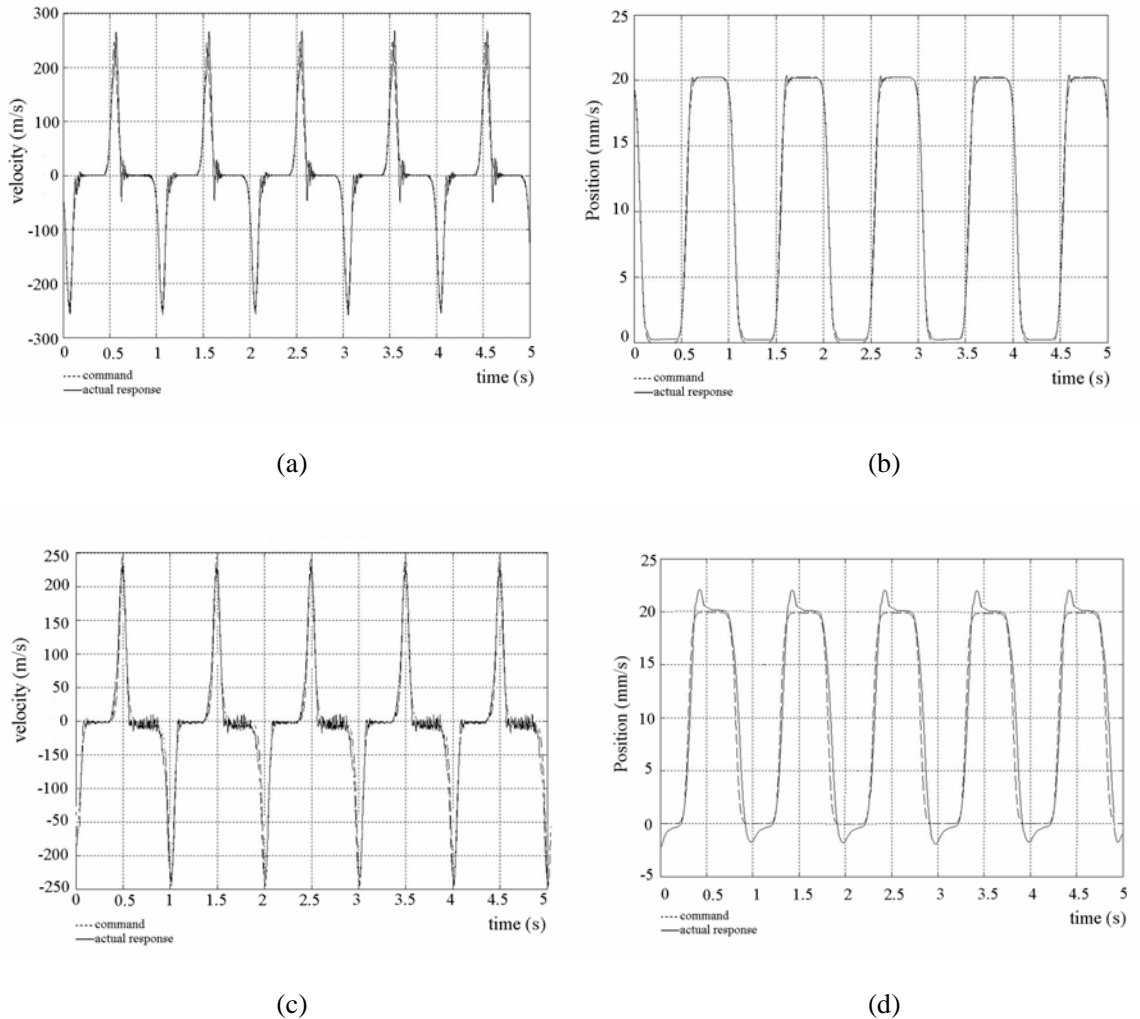


Fig.7.13 Response of ADRC controller under 1 Hz, 20 mm (a) Velocity response of X-Axis (b) Position response of X-Axis (c) Velocity response of Y-Axis (d) Position response of Y-Axis

Next, the following disturbances are added to the motor to simulate some of real working conditions (take X-axis mover for example only). They are,

- i) Mass change—a steel block of 17.5 N is fixed on the X-mover.
- ii) Force disturbances of about 2% is added from the input control command which occurs at time=1.8 s.
- iii) Friction variations with the help of a pull-spring attached (Elasticity coefficient of 57.5 N/m).

The output performance of velocity for the PID controller is unbalanced since the attached object is fixed toward one side of the mover (not centered). The unbalance may be caused by the added mechanical asymmetry. Concerning the response of ADRC, there also exist some unbalances but they are quite small as shown in Fig.7.14.

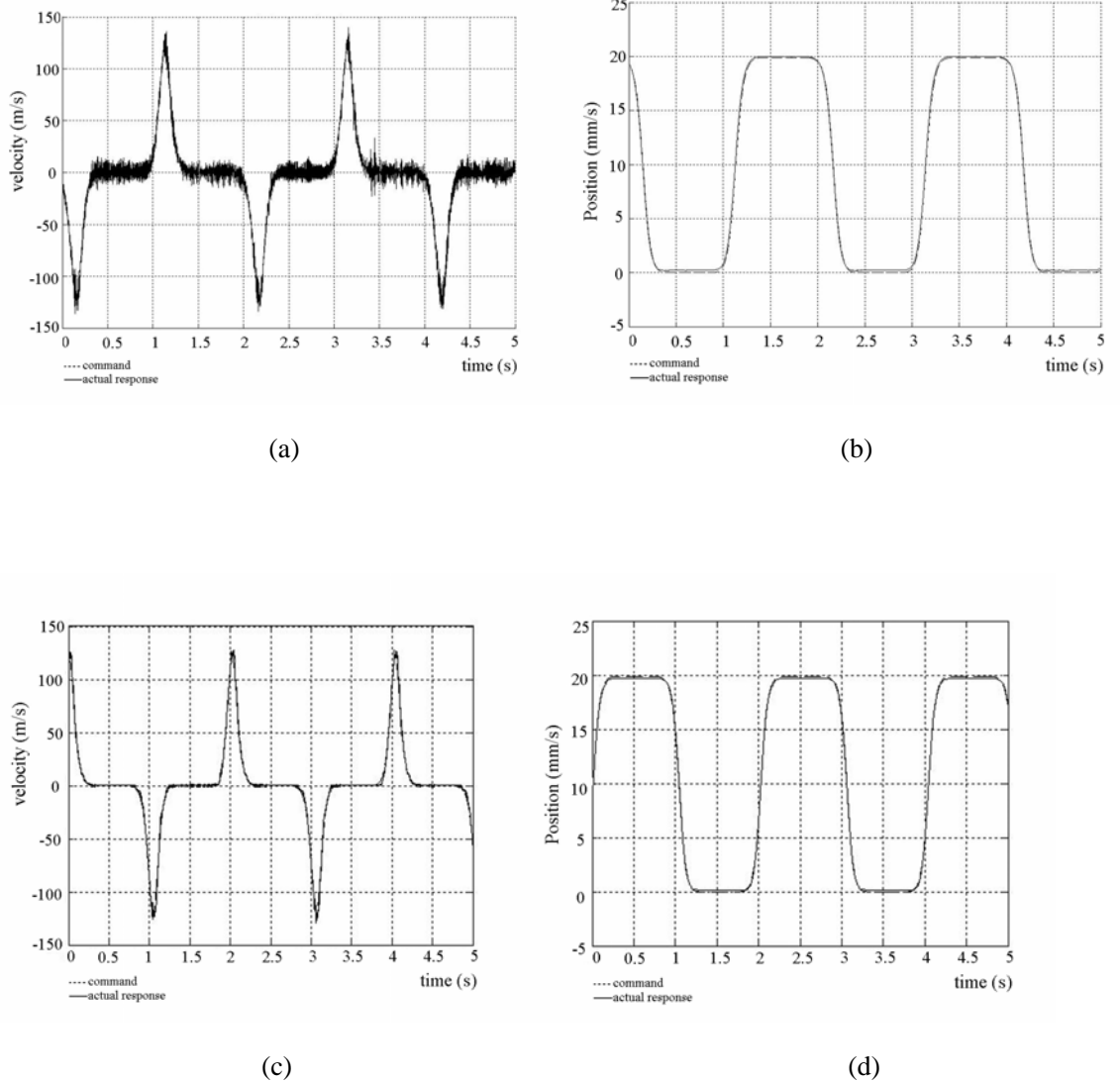


Fig.7.14 Response of PID and ADRC controller under mass change at 0.5Hz, 20 mm (a) Velocity response of PID (b) Position response of PID (c) Velocity response of ADRC (d) Position response of ADRC

It can be seen from Fig.7.15 when force disturbances are introduced, the output

performance of velocity becomes worse and the waveform becomes more and more noisy and it cannot return back to original conditions. Also there occurs a position shift from the actual position tracking profile. While for the ADRC controller, there encounters a velocity dip at time 1.8 s, but the velocity recovers back in a very short time. The motor is only under the pull of the spring in one direction of motion, but the force is varied at each position of the mover according to the stator. The velocity response profile in Fig.7.16 shows that the speed variations are unbalanced for each direction and the tracking error is much bigger for the PID controller. Therefore the ADRC is more robust.

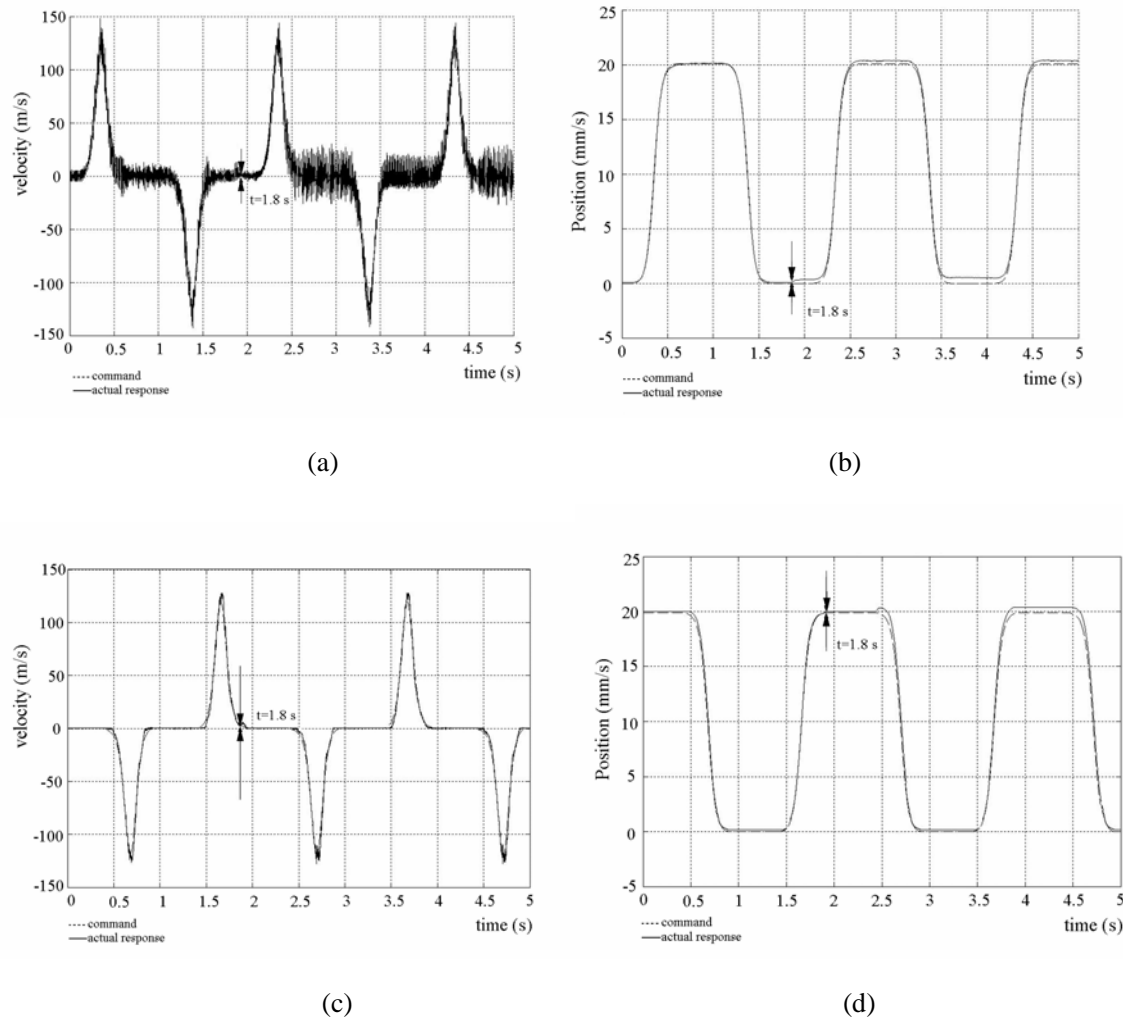


Fig.7.15 Response of PID and ADRC controller under force variation at time=1.8 s at 0.5 Hz 20 mm (a)

Velocity response of PID (b) Position response of PID (c) Velocity response of ADRC (d) Position response of ADRC

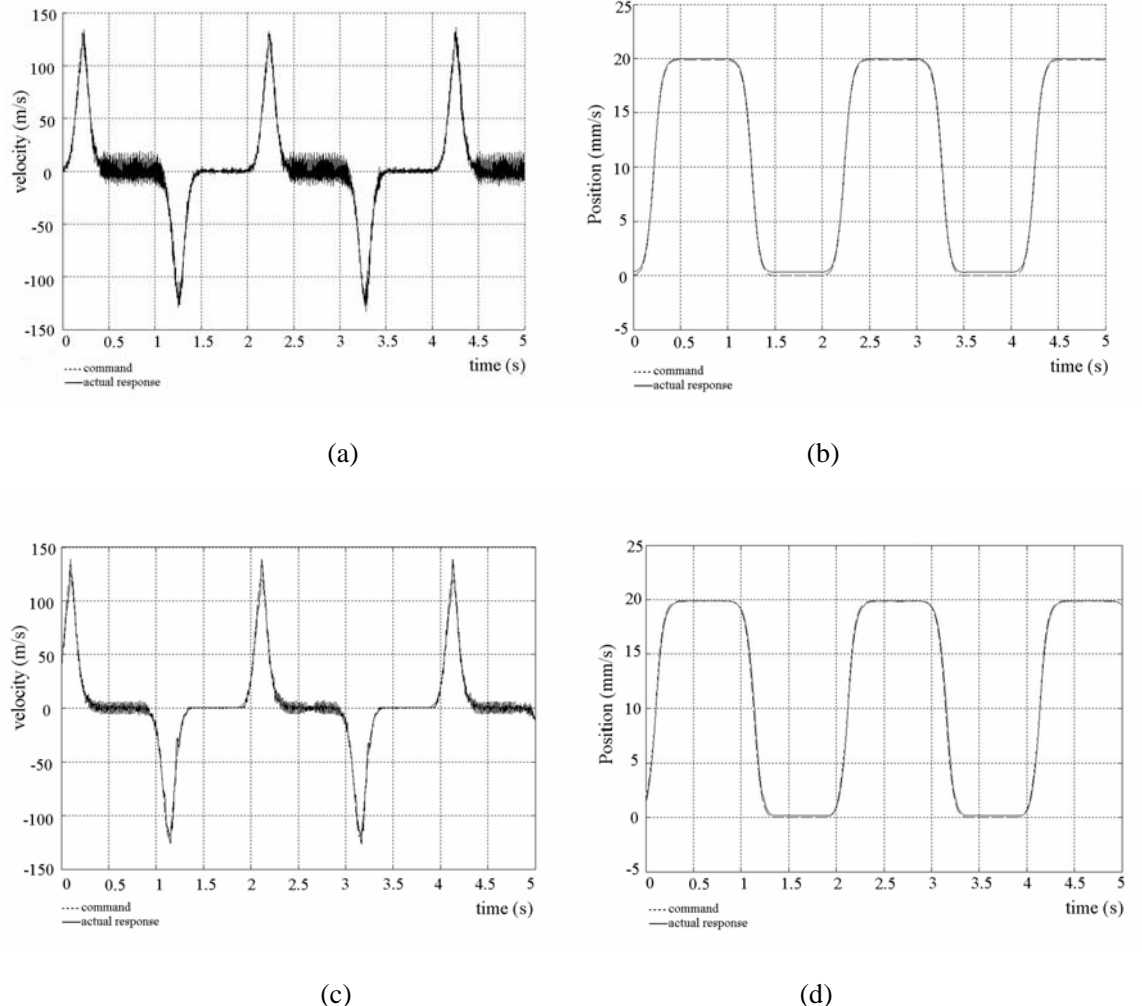


Fig.7.16 Response of PID and ADRC controller under force variation at time=1.8 s at 0.5 Hz 20 mm (a) Velocity response of PID (b) Position response of PID (c) Velocity response of ADRC (d) Position response of ADRC

7.6 The three-loop controller

In servo control applications, the motor is operated under a three-loop manner. Between the inner current loop and outer position loop, an intermediate loop of velocity regulation is

inserted to regulate the speed profile and improve the performance of position response. The control block is shown in Fig.7.17.

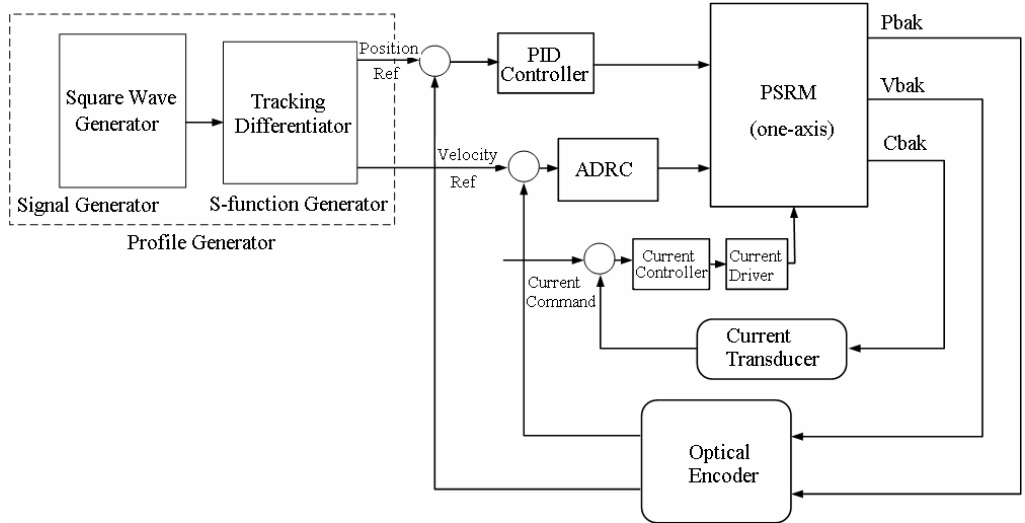


Fig.7.17 The three-loop control scheme

To further testify that the position response can be improved under the three-loop control, a simulation toward the comparisons of two-loop control and three-loop control has been carried out for X-axis of motion. As shown in Fig.7.18 and Fig.7.19, from the dynamic error profile, it can be concluded that position performance can be further improved under speed regulation with ADRC scheme.

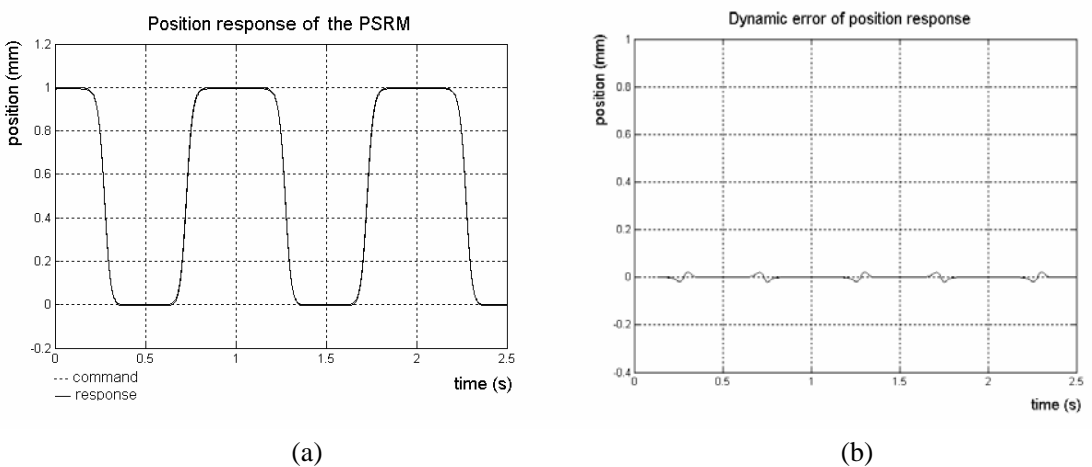


Fig.7.18 Simulation result under two-loop control (a) position response (b) dynamic error

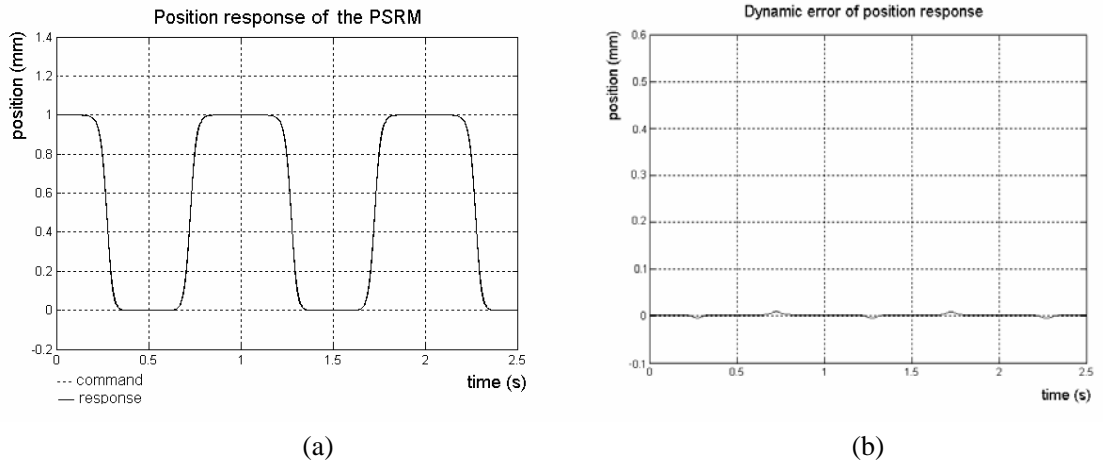


Fig.7.19 Simulation result under three-loop control (a) position response (b) dynamic error

7.7 Summary

This chapter proposes a model-independent control strategy based on ADRC principle and the new control scheme has been implemented on the novel planar switched reluctance motor for speed regulation. Compared with the PID control method of the planar motor, in which parameter variations and external disturbances can affect its speed performance, the ADRC is more resistant to uncertainties or disturbances. Therefore the ADRC is a much better choice in controlling the planar SR motor. It is expected that the same method can be applied to control other SR motors with much better robustness than PID control.

The main work from this chapter is concentrated on speed regulation with ADRC strategy. It can be seen from the above experiment results that trajectory performance is not well regulated. Therefore, the task ahead will be focused on position control using ADRC method. It is worthwhile to mention that in a second order ADRC scheme, parameters to be regulated would be huge. One feasible method under construction is to implement GA (Genetic Algorithm) to calculate them online.

Chapter 8

Conclusions and future work

This thesis describes a novel and unique direct-drive planar motor utilizing SR technology. The design, construction, analysis, characterization, modeling and implementation have also been described. This conclusion chapter summarizes the research work and findings in four different areas.

First, the literature review on other types of planar motors is carried out and the PSRM is proposed. Then the detailed investigation work on the PSRM ranging from its design to its construction is described. Performance analysis, characterization and modeling are conducted. After that, the work regarding to linearization scheme, different control aspects and implementation are summarized. Then achievements from the research work are concluded. Finally, further work for this research project is suggested.

8.1 Conclusions on the planar motor

This project aims at developing a novel 2D direct-drive motor taking the advantages of SR technology of simple construction and robust structure. The needs to develop a new type of planar motor are addressed. After reviewing other types of planar motors available at present, it is found that the PSRM meets most of the requirements for an ideal 2D machine. In addition, the production and cost of the PSRM is extremely low. These features are found to be attractive to a highly demanding market. The PSRM is a direct-drive machine that eliminates mechanical couplings such as lead screws and gears. It is

expected to be an ideal replacement for X-Y tables to achieve 2D motion in industry.

For the performance prediction of this machine, it has shown that the finite element method is most suitable for analyzing the magnetic circuit in the PSRM especially in the presence of magnetic saturation with end and edge effects. From both of FEM and experiment results, it has been concluded that the magnetic circuit of the PSRM is highly decoupled from each axis, therefore the two axis of motion can be simulated and controlled independently without any decoupling mechanism involved. Then the effect of Z disparity which is unique to the PSRM is studied with FEM and measurement. Both results show that the effect of Z-force is negligible and there is no need for the introduction of any decoupling mechanism for Z-axis.

8.2 Conclusions on the characterization and modeling of the PSRM

In order to describe the PSRM accurately, a mathematical model has been built to identify all the parameters within the model. Among all the magnetic parameters, magnetic flux-linkage is most typical and it is able to describe the characterization of the PSRM thoroughly. Flux-linkage measurement with the Step Voltage method has been first conducted. To further explore the motor behaviors during the demagnetization cycle, the AC excitation method has been carried out. In addition to flux-linkage, other magnetic characteristics such as hysteresis and leakage flux-linkage are also observed.

Based on the information from flux-linkage measurement, a dynamic model described with state-space equations is constructed. This model includes the nonlinear magnetic characteristics modeled with an exponential function. For modeling simplicity, some motor

information including friction and core losses are omitted from the dynamic model.

The characterization of this motor is based on an ideal model for this model. If there is some mechanical tolerance during manufacturing, the imperfections could affect the performance of the motor. For example, if the mover teeth and the stator teeth can not overlap fully or have some accumulated errors during traveling, the motor parameters such as leakage or zero mutual inductance may no longer be considered as negligible. Therefore a precise mechanical manufacture of the machine is required at the very first stage.

8.3 Conclusions on the control of the PSRM

This section contains conclusions on the control aspects of the PSRM and they are described in subsection 8.3.1, 8.3.2 and 8.3.3, respectively.

8.3.1 Nonlinear compensation

After selection of an appropriate current regulator based on PID with pulse-width modulation technique, it is important to develop a nonlinear compensator to tackle the nonlinear behavior of the PSRM. The multi-phase excitation scheme combined with the 2D look-up table towards smooth motor operation and easy implementation is proposed. The experiment that verifies the linearization scheme has also been conducted and it shows that the scheme is a good nonlinear compensator for the PSRM.

8.3.2 Position control

Considering the practical implementation of a control method in industrial use, a simple and effective Proportional Derivative (PD) controller is proposed and implemented.

A pair of sinusoidal signals is selected as the tracking command for each axis of motion to reduce the mechanical stress and simulate future working environment practically. The experiment results show that it is capable of achieving high accuracy and it can also be concluded that the motor is magnetically decoupled and each axis of motion can be controlled independently.

An improved dual-loop position controller is proposed which aims at reducing dynamic error at a higher working frequency. The controller is implemented and measurement results verify its effectiveness. Experiment results show that the response of each axis under this controller has less dynamic errors at higher working frequencies.

8.3.3 Speed regulation

For working environment filled with noise and disturbances, a model-independent control strategy based on ADRC principle has been proposed. From simulation and experiment, the PID control method is subjected to parameter variations and external disturbances. The new control scheme has been implemented on the novel planar switched reluctance motor for speed regulation. Compared with the PID control method, from the experiment results, ADRC strategy is more resistant to parameter uncertainties and external disturbances.

8.4 Achievements of this research work

The achievements of this research work can be summarized into four main areas,

- i) Motor design and construction

- ii) Performance analysis of the PSRM
- iii) Characterization and modeling of the PSRM
- iv) Control strategies

8.4.1. Motor design and construction

Design and construction of an innovative magnetically decoupled planar switched reluctance motor have been conducted. By utilizing the SR technology, the motor has a simple structure and robust characteristics. The motor can also benefit from low cost for manufacture.

A unique stator structure is proposed that facilitates magnetic paths in two perpendicular directions. This structure not only reduces eddy current effects, but the size and shape can be modified according to the designers' need without reconstruction of the whole system.

8.4.2. Performance analysis of the PSRM

In view of design and performance prediction, a thorough numerical analysis has been carried out toward performance analysis of the motor. Some features especially to the PSRM have been carefully explored. The negligible mutual effect between any of the six movers ensures an independent operation for each axis of motion. The edge effects that cause Z-force disparities have been observed with both FEM and measurement. A detailed analysis of air gap length on the influence of normal force has been carried out. Propulsion force from one mover has also been observed with both FEM and experiment.

8.4.3. Characterization and modeling of the PSRM

Flux-linkage characteristics of the PSRM with respect to current levels and positions are examined from two different techniques. Amongst all the methods reviewed, exponential description function is found to be the most appropriate and cost-effective for modeling the machine. According to the results from measurement, the model is confirmed to be accurate enough for controller design and simulation purposes.

8.4.4 Control strategies

A linearization scheme has been proposed for the PSRM. The multi-phase excitation strategy ensures a smooth operation of the moving platform. Combined with a compact 2D look-up table as the nonlinear compensator, fast online calculation and easy implementation can be ensured. A simple and practical PD controller is implemented on the whole control system. From experiment results, the control strategy is confirmed to be effective.

An improved dual-loop position controller is proposed which can reduce dynamic error at higher frequency. The effectiveness of the position controller is verified with experiment.

A robust, model-independent speed regulator has been proposed and implemented onto the whole motion system. Compared with a PID speed controller, ADRC is more resistant to parameter uncertainties and external disturbances. This control strategy can be applied to the control of the PSRM for practical use in industry, especially when there are parameter uncertainties and large external disturbances.

8.5 Suggestions for further research

It is expected that for further PSRM design, optimization is performed for the motor geometry variables such as pole-pitch, slot width or stack length, etc. With the help of both analytical and numerical method, a more efficient planar motor can be constructed.

When optimization of the motor is carried out, the work is suggested toward the following aspects,

For the stator,

- i) The mechanical support cover for the stator can be made thick enough to fix the stator.
- ii) Try to make sure that every stator pole is at the same height, which ensures the air gap to be uniform.
- iii) Flat types of linear guides are suggested to replace the linear bars for X moving platform, which are more strong and friction-free. Larger size may be used if they cannot afford large normal force.

For the mover,

- i) The mover fasteners should be strong enough and more screws are suggested to fix them. Due to the large normal force, they may bend downward and finally affect the air gap.
- ii) Try to make the six movers at the same height to ensure a uniform air gap.

For further research investigation of control algorithms, it is suggested that more robust control schemes be carried out both on speed and trajectory regulation. It is applicable to construct a second order ADRC controller for trajectory applications, though

there would involve large parameters to be regulated. An online estimation and correction scheme based on Genetic Algorithm (GA) can be employed to determine and correct the best values online.

Developing a speed or position estimation technique is a good way to lower the cost of the entire motion system and extend its applications. This can be achieved with additional feedback information to the controller such as voltage, instantaneous change of inductance, etc. Then sensorless control can be applied to replace the pair of optical encoders mounted on the moving platform. This not only reduces the cost and the implementation procedure of the encoders, but the motion system can be operated under a wide range of temperature with no sensor hardware involved.

Appendix A

Motor specifications and figures

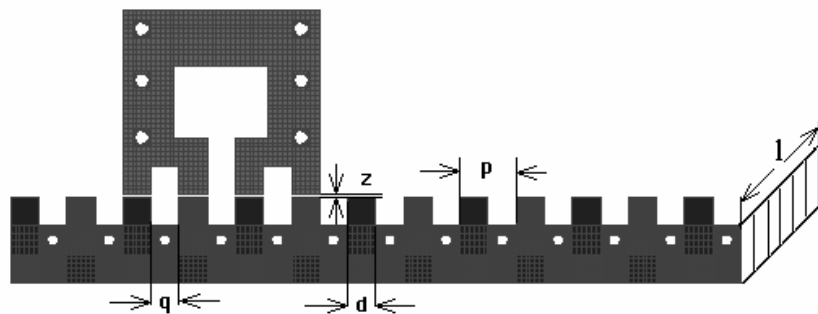


Fig.A.1 Symbols of motor specifications

Mover mass (X)	8.75 Kg (Mx)
Mover mass (Y)	15 Kg (My)
Size of base plate	450×450mm
Travel distance	300×300mm
Air gap	0.55mm (z)
Number of turns per phase	160 (N)
Phase resistance	1.5Ω (R)
Pole pitch	6 mm (p)
Pole width	6mm (d)
Pole slot	6mm (q)
Encoder precision	0.5 μm

Table.A.1 PSRM specifications and symbols

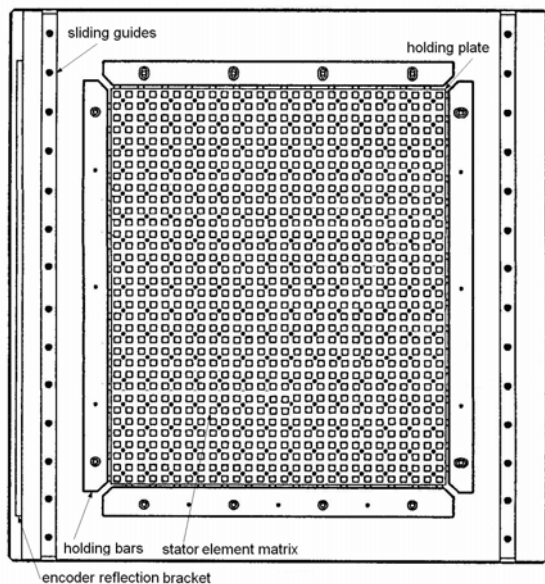
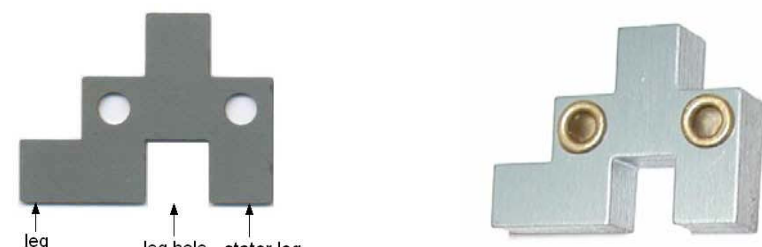


Fig.A.2 Stator top view



(a)

(b)



(c)

(d)

Fig.A.3 Formation of the stator. (a) single stator plate (b) one block (c) building blocks (d) one stator

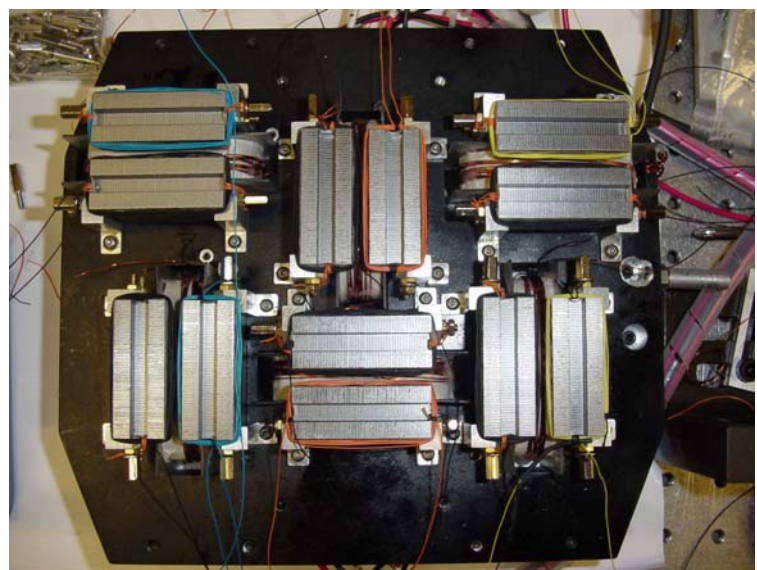


Fig.A.4 Structure of the moving platform

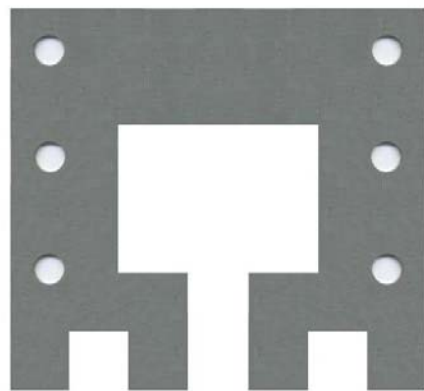


Fig.A.5 single mover plate (one lamination)

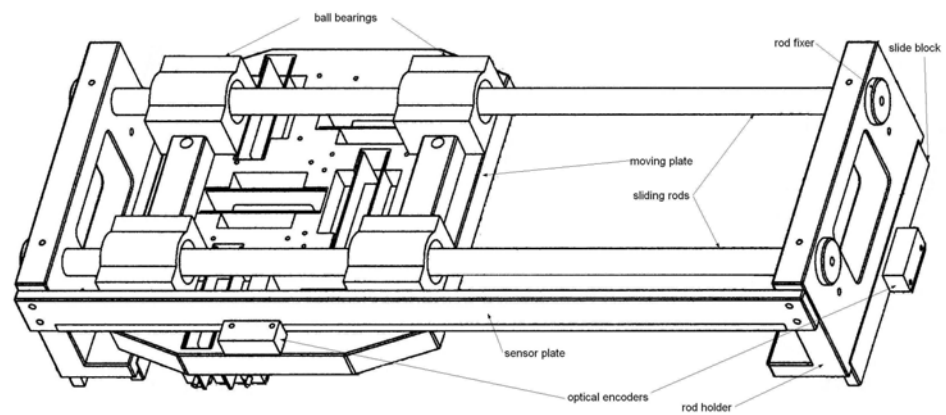


Fig.A.6 The moving platform

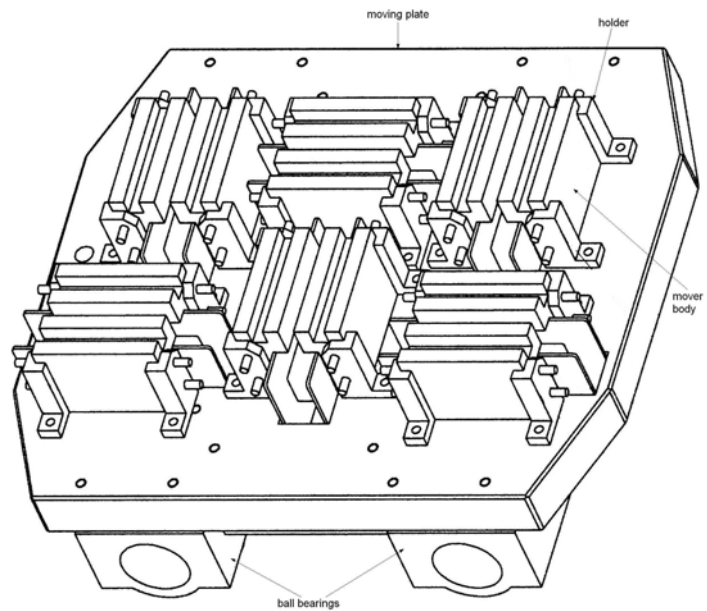


Fig.A.7 The mover structure

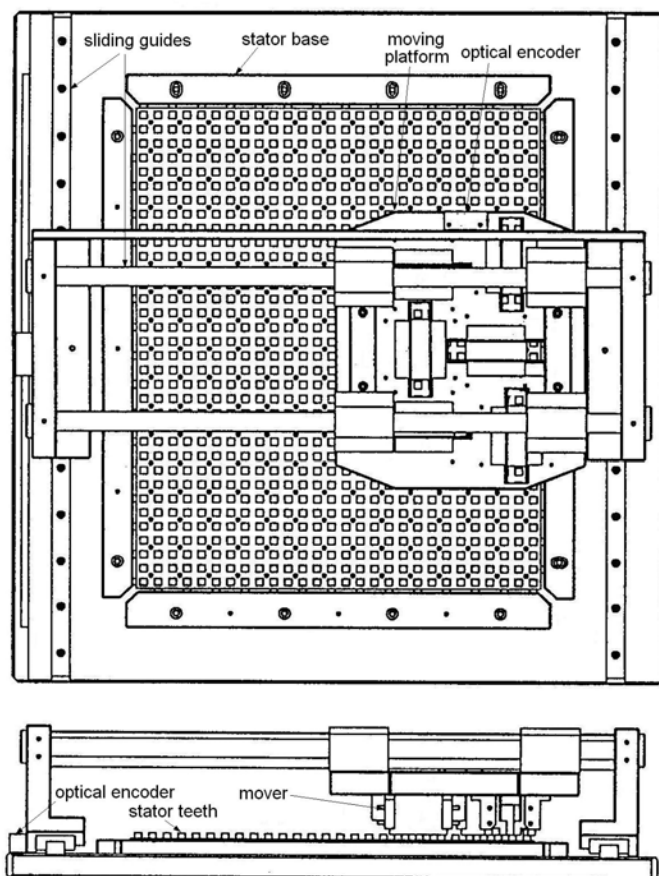


Fig.A.8 Top and side of view of the overall structure

Appendix B

Hardware environment of dSPACE DS1104

The dSPACE DS1104 kit is used as the system controller and data acquisition tool throughout the project as shown in Fig.B.1. The main components include a single-board DSP controller, Real-Time Interface (RTI) to *MATLAB SIMULINK* and experiment software ControlDesk Standard [85].

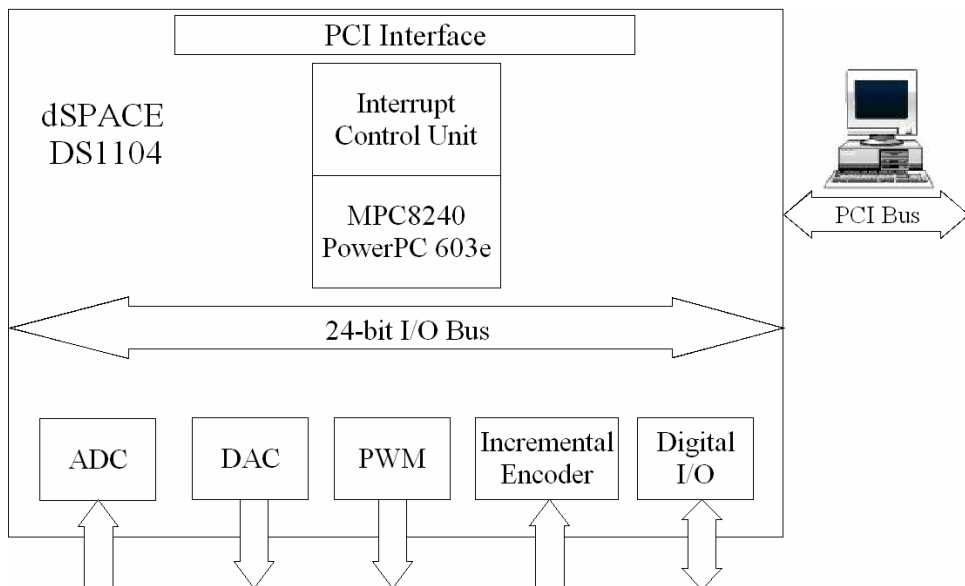


Fig.B.1 The DSP controller setup

The main real-time computing units include an on-board DSP MPC8240 with 250MHz frequency and a PowerPC 603e core floating-point processor. The hardware board interfaces the Personal Computer (PC) through the Peripheral Component Interconnect (PCI) bus. The interface circuit consists of two 24-bit digital incremental encoder channels, four 16-bit and four 12-bit Digital-to-analog Converters (DAC), eight 16-bit Analog-to-digital Converters (ADC) and seven Pulse Width Modulation (PWM) channels.

Graphical programs or control block diagrams from *SIMULINK* blocks can be converted into C-code, then compiled and downloaded to the DSP chip running in real-time. On the other hand, the Real-Time Interface (RTI) from dSPACE provides graphical configuration and the ControlDesk Standard software interfaces with the user, accepting the inputs graphically, modifying the parameters online and displaying the current status of the controll system and logging of necessary data. Fig.B.2 shows the interaction between *MATLAB SIMULINK* and the DSP.

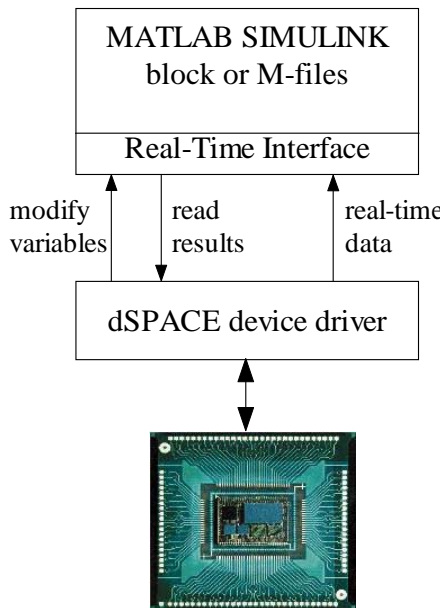


Fig.B.2 Interaction between MATLAB and dSPACE.

The two incremental encoders interface receive the position signals from each direction of axis respectively, while the ADC channels receive and convert current or other measurement into digital signals. For control experiments, the dSPACE controller board calculates the control algorithm on the basis of the measured values and determines the corresponding output values.

References

- [1] B.A. Sawyer, "Magnetic Positioning Device", U.S. Patent 3,457,482, July 1969
- [2] E.R. Pelta, "Two-axis Sawyer Motor for Motion Systems", IEEE Control Systems Mag., Oct 1987. Volume 7, Issue 5, Oct 1987 Page(s):20 - 24
- [3] N. Fujii, T. Kihara. "Surface Induction Motor for Two Dimensional Drive", Trans. of IEE of Japan, Part D, Vol. 118-D, Iss. 2, pp 221-228, Feb 1998
- [4] A. F. Flores Filho, A. A. Susin, and M. A. da Sliveira. "Development of a Novel Planar Actuator", Ninth International Conference on Electrical Machines and Drives, 1999. (Conf. Publ. No. 468) 1-3 Sept. 1999 Page(s):268 - 271
- [5] D. Ebihara and M. Watada. "Study of a Basic Structure of Surface Actuator", IEEE Trans. on Magnetics, Vol.25, No.5, pp.3916-3918, September 1989
- [6] Mak, Sui-tong, "Precision Motion Control of X-Y table with Closed-loop Commuted Stepper Motor", M.Sc. thesis, the Hong Kong Polytechnic University, 1997
- [7] Zatsiorsky, Vladimir M. "Kinetics of Human Motion", Champaign, IL: Human Kinetics, 2002
- [8] T. J. E. Miller, Switched Reluctance Motor and Their Control. London, U.K.: Oxford Univ. Press, 1993
- [9] P. C. Kjaer, J. J. Gribble, and T. J. E. Miller, "High-grade Control of Switched Reluctance Machines," IEEE Trans. Ind. Electron., vol. 33, pp. 1585–1593, Dec. 1997
- [10] D. M. Dawson, J. Hu, and T. C. Burg, Nonlinear Control of Electric Machinery. New York: Marcel Dekker, 1998

- [11] Ren C. Luo and jyh Hwa Tzou. “Investigation of a Linear 2-D Planar Motor Based Rapid Tooling System”, Proc. of the 2002 IEEE International Conf. on Robotics & Automation pp. 1471-1476, Washington, DC, May 2002
- [12] J. Ish-Shalom. “Composite Magnetic Structure for Planar Motors”, IEEE Trans. on Magnetics, Vol.31, No.6, pp.4077-4079, Nov.1995
- [13] A. E. Brennemann and R. L. Hollis. “Magnetic and Optical-fluorescence Position Sensing for Planar Linear Motors”, Proc. Int. conf. on Intelligent Robots and Systems (IROS95), Vol.3, pp.101-107, Pittsburgh 1995
- [14] J. I. Shalom. “Modeling of Sawyer Planar Sensor and Motor Dependence on Planar Yaw Angle Rotation”, Proc. of the IEEE Intel. Conf. on Robotics and Automation Albuquerque, pp.499-3504, New Mexico-April 1997
- [15] J. Ish-Shalom. “Sawyer Sensor for Planar Motion Systems”, IEEE Int. Conf. R&A, San Diego, pp.2652-2658, May 1994
- [16] N. Fujii, T. Kihara. “Surface Induction Motor for Two Dimensional Drive”, Trans. of IEE of Japan, Part D, Vol. 118-D, Iss. 2, pp 221-228, Feb 1998
- [17] N. Fujii and M. Fujitake. “Two-Dimensional Drive Characteristics by Circular Shaped Motor”, IEEE Trans. on Industry Applications, Vol.35, Iss.4, pp. 167-173, July-Aug. 1999.
- [18] N. Fujii, M. Fujitake and K.Hara. “Two-Dimensional Motion with Circular Core and Plural Divided a Windings Supplied Separately”, IEEE Trans. on Magnetics, Vol.35, No.5, pp.4010-4012, Sep.1999
- [19] B. Hoffman and S. Pollack, “Platen Laminated Structure in Mutually Perpendicular Direction for Use with Linear Motors and the Like”. US patent 4,835,424, May 1989

- [20] Chitaya, etc, “Two-axis Motor with High Density Magnetic Platen”, U.S. Patent 5777402, July 1998
- [21] D.L.Trumper, etc, “Magnetic Arrays”, U.S. Patent 5631618, may 1997
- [22] Han-Sam Cho, Chang-Hwan Im. “Magnetic Field Analysis of 2-D Permanent Magnet Array for Planar Motor”, IEEE Trans. on Magnetics, Vol.37, No.5, pp.3762-3766, September 2001
- [23] Junichi Tsuchiya and Gunji Kimura. “Mover Structure and Thrust Characteristic of Moving-magnet-type Surface Motor”, IECON’01: The 27th Annual Conf. of the IEEE Industrial Electronics Society, pp.1469-1474
- [24] Nasar, S.A., D.C., “Switched Reluctance Motor”, Proceedings of the Institution of Electrical Engineers (London), Vol. 116, No. 6, June 1969, pp. 1048
- [25] R. Krishnan, “Switched Reluctance Motor Drives: Modeling, Simulation, Analysis, Design, and Applications”, Boca Raton, FL : CRC Press, 2001
- [26] C. T. Liu, L. F. Chen, J. L. Kuo, Y. N. Chen, Y. J. Lee, and C. T. Leu, “Microcomputer Control Implementation of Transverse Flux Linear Switched Reluctance Machine with Rule-based Compensator,” IEEE Trans. Energy Conversion, vol. 11, pp. 70–75, Mar. 1996
- [27] Wai-Chuen Gan; Cheung, N.C.; Li Qiu; “Position Control of Linear Switched Reluctance Motors for High-precision Applications”, IEEE Transactions on Industry Applications, Volume 39, Issue 5, Sept.-Oct. 2003 Page(s):1350 – 1362
- [28] I. Boldea and S. A. Nasar, “Linear Electric Actuators and Generators”, Cambridge, U.K. Cambridge Univ. Press, 1997
- [29] Cheng-Tsung Liu; Jian-Long Kuo; “Experimental Investigation and 3-D Modelling of

Linear Variable-reluctance Machine with Magnetic-flux Decoupled Windings”, IEEE Transactions on Magnetics, Volume 30, Issue 6, Part 1-2, Nov 1994 Page(s):4737– 4739

[30] Ding, Zhigang, “Linear Stepping Motors—Principle, Control and Applications”, Mechanical Industry publisher, Beijing

[31] J.F. Pan, N.C Cheung and Jinming Yang; “High-precision Position Control of a Novel Planar Switched Reluctance Motor”, IEEE Transactions on Industrial Electronics, Volume 52, Issue 6, Dec., 2005, Page(s):1644 – 1652

[32] N. C. Cheung, J. F. Pan, and J. M. Yang; “Two Dimensional Variable Reluctance Planar Motor”, Ref: IP-135A, file no: I040420E, filed date: July 2004

[33] H. -D. Chai, “Electromechanical Motion Devices”, Prentice Hall PTR, USA, 1998

[34] A. E. Fitzgerald and C. Kingsley, Jr. “Electric Machinery”, McGraw Hill, Tokyo, Japan, 1961

[35] Roters. Herbert C., “Electromagnetic Devices”, New York, J. Wiley & sons, inc.; London: Chapman & Hall, limited, 1941

[36] Reece A. B. J. and T. W. Preston, “Finite Element Methods in Electrical Power Engineering”, Oxford University Press, London, U.K., 2000

[37] “User Manual, *MEGA V6.29*”, Applied Electromagnetic Research Centre University of Bath, Bath, London, U.K., 4th.August 2003

[38] “Tutorial Examples, *MEGA V6.29*”, Applied Electromagnetic Research Centre University of Bath, Bath, London, U.K., 4th.August, 2003

[39] Valery Rudnev, Don Loveless, etc., “Handbook of Induction Heating”, New York : Marcel Dekker, 2003

- [40] Mark J. Debortoli, “Extensions to the Finite Element Method for the Electromechanical Analysis of Electric Machines”, PhD thesis, INPG, Grenoble, France, 1987
- [41] Sheppard J. Salon, “Finite Element Analysis of Electrical Machines”, Kluwer Academic Publishers, Boston, U.S.A. 1995
- [42] Jianfei Pan, N.C. Cheung, and Jinming Yang, “Position Control of a Novel Planar Switched Reluctance Motor”, Industrial Electronics Society, 2004. 30th Annual Conference of IEEE, Volume 3, 2-6 Nov. 2004, Page(s):2400 - 2405 Vol. 3
- [43] “Driver Manual”, Advanced Motion Controls, Camarillo CA, U.S.A
- [44] P. P. Acarnley and R. Aggarwal, “Inductance and Static Torque Measurements in Small Reluctance Type Machines”, Proc. UPEC, vol.10, pp.177-181, 1972/73
- [45] J. C. Prescott and A. K. El-kharashi, “A Method for Measuring Self-inductance Applicable to Large Electrical Machines”, Proc. Inst. Elect. Eng. A Vol.106, pp.169-173, 1959
- [46] A.D. Cheok, and N. Ertugrul, “Computer-based Automated Test Measurement System for Determining Magnetization Characteristics of Switched Reluctance Motors”, IEEE Transactions on Instrumentation and Measurement, Volume 50, Issue 3, June 2001, Page(s):690 – 696
- [47] V. Ramanarayanan, L. Venkatesha, and D. Panda, “Flux-linkage Characteristics of Switched Reluctance Motor”, IEEE International Conference on Power Electronics, Drives and Energy Systems for Industrial Growth, 1996., Proceedings of the 1996, Volume 1, 8-11 Jan. 1996 Page(s):281 - 285 vol.1
- [48] V. K. Sharma, S. S. Murthy, and Singh, B., “An Improved Method for the Determination

- of Saturation Characteristics of Switched Reluctance Motors”, IEEE Transactions on Instrumentation and Measurement, Volume 48, Issue 5, Oct. 1999, Page(s):995 – 1000
- [49] A. Ferrero, A. Raciti, and C. Urzi, “An Indirect Test Method for the Characterization of Variable Reluctance Motors”, IEEE Transactions on Instrumentation and Measurement, Volume 42, Issue 6, Dec. 1993 Page(s):1020 – 1025
- [50] N. C. Cheung, “A Nonlinear, Short Stroke Proportional Solenoid”, PhD thesis, the University of New South Wales, Australia, Sydney, July 1995, 311 pages.
- [51] G. R. Slemmon and A. Straughen, “Electric Machines”, Addison-Wesley Pub. Co., 1980
- [52] A. Ferrero and A. Raciti, “A Digital Method for the Determination of the Magnetic Characteristic of Variable Reluctance Motors”, IEEE Transactions on Instrumentation and Measurement, Volume 39, Issue 4, Aug. 1990 Page(s):604 - 608
- [53] M. Stiebler and K. Liu, “An Analytical Model of Switched Reluctance Machines”, IEEE Transactions on Energy Conversion, 14 (4):1100-1107, December 1999.
- [54] S. A. Hossain and I. Husain, “A Geometry Based Simplified Analytical Model of Switched Reluctance Machines for Real-time Controller Implementation”, IEEE Transactions on Power Electronics, 18 (6):1384-1389, November, 2003
- [55] X.-D. Xue, K. W. E. Cheng, and S. L. Ho, “Simulation of Switched Reluctance Motor Drives Using Two-dimensional Bicubic Spline”, IEEE Transaction on Energy Conversion, 17 (4):471-477, 2002
- [56] F. Soares and P. J. C. Branco, “Simulation of a 6/4 Switched Reluctance Motor”, IEEE Transactions on Aerospace and Electronic Systems, 37(3):989-1009, July, 2001
- [57] C. Roux and M. M. Morcos, “On the Use of a Simplified Model for Switched Reluctance

- Motors”, IEEE Transactions on Energy Conversion, 17(3):400-405, September, 2002
- [58] H.-P. Chi, R.-L Lin and J.-F. Chen, “Simplified Flux-linkage Model for Switched Reluctance Motors”, IEEE Proceedings on Electric Power Applications, Volume 152, Issue 3, 6 May 2005, Page(s):577 - 583
- [59] S. A. Bortoff, R. R. Kohan and R. Milman, “Adaptive Control of Variable Reluctance Motors: A Spline Function Approach”, IEEE Transactions on Industrial Electronics”, 45(3):433-444, June, 1998
- [60] M. Ilic'-Spong, M., R. Marino, S. Peresada and D. Taylor, “Feedback Linearizing Control of Switched Reluctance Motors”, IEEE Transactions on Automatic Control, Volume 32, Issue 5, May 1987 Page(s):371 - 379
- [61] F. Blaabjerg, P.C. Kiaer, P.O. Rasmussen, C. Cossar, “Improved Digital Current Control Methods in Switched Reluctance Motor Drives”, IEEE Transactions on Power Electronics, Volume 14, Issue 3, May 1999 Page(s):563 - 572
- [62] B. S. Lee, H. K. Bae, P. Vijayraghavan and R. Krishnan, “Design of a Linear Switched Reluctance Machine,” IEEE Trans. on Industry Applications, vol. 36, no. 6, pp.1571-1580, Nov., 2000
- [63] D.S. Schramm, B. W. Williams and T. C. Green, “Torque Ripple Reduction of Switched Reluctance Motors by Phase Current Optimal Profiling”, 23rd Annual IEEE on Power Electronics Specialists Conference, 1992. PESC '92, 29 June-3 July, 1992, Page(s):857 - 860 vol.2
- [64] I. Husain and M. Ehsani, “Torque Ripple Minimization in Switched Reluctance Mmotor Drives by PWM Current Control” IEEE Transactions on Power Electronics, Volume

11, Issue 1, Jan. 1996 Page(s):83 – 88

- [65] J.M. Stephenson, J. Corda, “Computation of Torque and Current in Doubly Salient Reluctance Motors from Non-linear Magnetization Data”, IEE Proceedings, Vol. 126, pp 393-396, 1979
- [66] Lu, W., Keyhani, A., Klode, H., Proca, A.B. “Modeling and Parameter Identification of Switched Reluctance Motors From Operating Data Using Neural Networks”, IEEE International Conference on Electric Machines and Drives, IEMDC'03, June, 2003. Pages: 1709 - 1713 vol.3
- [67] Katsuhiko Ogata, “Modern Control Engineering (4th edition)”, Upper Saddle River, N.J. Prentice Hall, 2002
- [68] J. F. Pan, N. C. Cheung, W. C. Gan and S. W. Zhao, “A Novel Planar Switched Reluctance Motor for Industrial Applications”, IEEE Transactions on Magnetics, Vol. 42, No. 10, Oct, 2006
- [69] K. ÅSTRÖM and T. HÄGGLUND, “PID Controllers: Theory, Design and Tuning”. Research Triangle Park, N.C., International Society of America, c1995
- [70] Zhiqiang Gao, Yi Huang, and Jingqing Han, “An Alternative Paradigm for Control System Design”, Decision and Control, 2001. Proceedings of the 40th IEEE Conference, Volume: 5, 4-7 Dec. 2001, Pages: 4578 - 4585 vol.5
- [71] Jianbo Su, Wenbin, etc. “Calibration-free Robotic Eye-hand Coordination Based on an Auto-disturbance Rejection Controller”, IEEE Transactions on Robotics, Volume: 20, Issue: 5, Oct.2004, Pages: 899 – 907
- [72] Y. Huang and J. Han, “Analysis and Design For the Second Order Nonlinear Continuous

Extended States Observer,” Chinese Sci. Bull., vol. 45, no. 21, pp. 1938 – 1944, 2000.

(In Chinese)

[73] Su, Y. X.; Duan, B.Y.; Zhang, Y.F., “Auto-disturbance Rejection Motion Control for Direct-drive Motors”, IECON 02 [Industrial Electronics Society, IEEE 28th Annual Conference, Volume: 3, 5-8 Nov. 2002, Pages:2073 - 2078 vol.3

[74] Sanmin Wei; Bin Wu; Ning Qiu; Congwei Liu, “Auto-disturbance Rejection Controller in Direct Torque Control of Permanent Magnet Synchronous Motor Drives”, The 4th International Conference on Power Electronics and Motion Control, IPEMC, 2004. Volume: 3 , Aug. 14-16, 2004 Pages: 1268 – 1272

[75] Guang Feng; Yan-Fei Liu; Lipei Huang, “A New Robust Control to Improve the Dynamic Performance of Induction Motors”, Power Electronics Specialists Conference, 2001. PESC. 2001 IEEE 32nd Annual, Volume: 2, 17-21 June 2001 Pages: 778 - 783 vol.2

[76] Li Xu and Bin Yao, “Output Feedback Adaptive Robust Control of Uncertain Linear Systems with Large Disturbances”, American Control Conference, Proceedings of the 1999, Volume: 1, 2-4 June 1999, Pages: 556 - 560 vol.1

[77] Su, Y.X., Duan B.Y.; Zhang, Y.F., “Robust Precision Motion Control for AC Servo System”, Proceedings of the 4th World Congress on Intelligent Control and Automation, 2002. Volume:4, 10-14 June 2002, Pages: 3319 - 3323 vol.4

[78] J.-Q. Han and W. Wang, “Nonlinear Tracking Differentiator,” J. Syst. Sci.Math. Sci., vol. 14, no. 2, pp. 177–183, 1994 (In Chinese)

[79] Han Jingqing, “Nonlinear State Error Feedback Control Law—NLSEF,” Control and

Decision, vol. 10, no. 3, pp. 221–225, 1995 (In Chinese)

[80] Han Jingqing, “The Extended State Observer of a Class of Uncertain Systems”, Trans. on Control and Decision, China, Vo1.10, no. 1, pp19-23, Jan, 1995 (In Chinese)

[81] Han Jingqing, “The Extended State Observer of a Class of Uncertain Systems”, Trans. on Control and Decision, China, Vo1.10, no. 1, pp19-23, Jan, 1995 (In Chinese)

[82] Han Jingqing, “Auto-disturbances Rejection Controller and Its Applications”, Trans. Control and Decision, China, Vo1.13, no. 1, pp19-23, 1998 (In Chinese)

[83] Y. Huang and J. Han, “Analysis and Design for the Second Order Nonlinear Continuous Extended States Observer,” Chinese Sci. Bull., vol. 45, no. 21, pp. 1938–1944, 2000 (In Chinese)

[84] Jianfei Pan, N. C. Cheung and J. M. Yang, “High-precision Position Control of a Novel Planar Switched Reluctance Motor”, IEEE Transactions on Industrial Electronics, Volume 52, Issue 6, Dec. 2005 Page(s):1644 – 1652

[85] “Installation and Configuration Guide, ds1104 R&D Controller Board”, Release 3.4, dSPACE Co. Ltd